DISSERTATION

submitted to the
Combined Faculty of Natural Sciences and Mathematics
of the Ruperto-Carola-University of Heidelberg, Germany
for the degree of
Doctor of Natural Sciences

Put forward by
Frans-Felix Schotsch
born in Heidelberg

Oral examination: December 9th , 2020

TrapREMI - Development of a Reaction Microscope inside a Zajfman Trap and First Photodissociation Experiments on Stored Molecular Ions

Referees: Priv.-Doz. Dr. Robert Moshammer
Prof. Dr. Andreas Wolf

Abstract

Within this thesis, a new experimental setup has been developed to investigate the quantum dynamics of molecular ions and charged clusters. An Electrostatic Ion Beam Trap (EIBT) stores a fast target beam at keV energies in oscillatory motion. By crossing it with a projectile beam, e.g. an IR laser, molecular reactions can be induced. We implemented a Reaction Microscope (REMI) in the field-free region of the EIBT to perform coincidence spectroscopy on the resulting reaction products. In contrast to prior experiments, this unique combination of techniques allows to measure the 3D momentum vectors of ions, electrons and neutrals as reaction products in coincidence. At the same time, the EIBT allows for advanced target preparation techniques, e.g. relaxation of hot molecules during storage times up to seconds, autoresonance cooling and recycling of target species which are difficult to prepare. The TrapREMI setup can be connected to a variety of projectile sources, e.g. atomic gas jets, large-scale radiation facilities and ultrashort laser pulses which enable even time-resolved studies. Here, we describe the setup development and first, IR-induced photodissociation experiments on O_2^+ and CH_4^+, providing a proof-of-principle for ion-neutral coincidence detection in the TrapREMI.

Im Rahmen dieser Arbeit wurde ein neuer experimenteller Aufbau entwickelt, um die Quantendynamik von molekularen Ionen und geladenen Clustern zu untersuchen. Eine elektrostatische Ionenfalle (EIBT) speichert einen Ionenstrahl bei keV-Energien in oszillierender Bewegung. Durch Kreuzung mit einem Projektilstrahl, z.B. einem IR-Laser, können molekulare Reaktionen induziert werden. Wir haben ein Reaktionsmikroskop (REMI) in den feldfreien Bereich der EIBT implementiert, um die resultierenden Reaktionsprodukte koinzidenzspektroskopisch zu untersuchen. Im Gegensatz zu früheren Experimenten erlaubt diese einzigartige Kombination experimenteller Techniken die Messung der 3D-Impulsvektoren aller Reaktionsprodukte, also von Ionen, Elektronen und Neutronen, in Koinzidenz. Gleichzeitig bietet die Speicherung in einer EIBT verschiedene Möglichkeiten zur Präparation des Ionenstrahls, z.B. Relaxation heißer Moleküle während Speicherzeiten von bis zu Sekunden, Phasenraumkühlung und Recycling schwer präparierbarer Spezies. An das TrapREMI kann eine Vielzahl von Projektilquellen angeschlossen werden, z.B. atomare Gasstrahlen und ultrakurze Laserpulse, die auch zeitaufgelöste Studien ermöglichen. Hier beschreiben wir die Entwicklung des Aufbaus und erste, IR-induzierte Photodissziationsexperimente an O_2^+ und CH_4^+, die einen proof-of-principle für die Koinzidenzdetektion von ionen und neutralen Produkten im TrapREMI darstellen.

DANKSAGUNG

Danke an alle die mich auf meinem Weg zum Abschluss dieser Arbeit begleitet haben!

Ich danke **Robert Moshammer**, der mich bei meiner Arbeit mit viel Fachwissen, Kompetenz und Geduld betreut hat. Die Möglichkeit solch ein Experiment aufzubauen ist etwas besonderes und eine tolle Erfahrung. Diese hat mir auch unser Direktor **Thomas Pfeifer** ermöglicht, der mich mit unerschütterlichem Optimismus und großer Fachkompetenz immer wieder neu motiviert hat. Einen großen Anteil am Zustandekommen dieses Aufbaus hat auch **Claus Dieter Schröter** ohne dessen Vakuumkompetenz und positiver Einstellung im Labor nicht viel laufen würde. Danke Robert, Thomas und Claus Dieter, ich habe immer sehr gerne mit euch zusammengearbeitet!

Herzlich danke ich auch **Andreas Wolf** und **Holger Kreckel** für das freundliche Bereitstellen der Ionenquelle ohne die viele Messungen nicht möglich gewesen wären und Andreas Wolf außerdem für die Begutachtung meiner Arbeit als Zweitkorrektor.

Extrem wichtig waren natürlich auch die studentischen Kollegen aus der Abteilung. Dank und mit euch hatte ich eine tolle Zeit, war das Institut ein Ort an dem ich immer gerne war. Danke vor allem an **Ilja Zebergs** für eine super Mitarbeit an diesem Projekt. Da ich nicht alle nennen kann, möchte ich noch die hervorheben welche mir beim Korrigieren dieser Arbeit geholfen haben. Dies waren **Severin Meister**, **Hannes Lindenmann**, **Florian Trost**, **Max Hartmann** und **Marc Rebholz**.

Das Labor wäre leer gewesen ohne das **Feinwerkmechachnik-Team** welches die TrapREMI Bauteile hergestellt hat und das **Electronik-Team**, welche diverse Geräte hergestellt und bei vielen kleinen Problemen geholfen hat. Besonders hervorheben möchte ich hier **Oliver Koschorreck**. Danke Oli für die viele Hilfe und die immer gute Stimmung! Besonders wichtig war auch das Team von **Christian Kaiser** das mir teilweise täglich mit viel Tat zur Seite stand, insbesondere **Steffen Vogel** und **Lucas Dengel** und gleiches gilt auch für **Alexander von der Dellen** und **Nikola Mollov**. Vielen Dank auch an **Christian Föhr** für das schöne Fotografieren des Aufbaus.

Abschließend möchte ich meinen lieben Eltern danken, die mich mein Leben lang unterstützt haben und ohne die ich nicht wäre. Ihnen sei diese Arbeit gewidmet.

Declaration:

I hereby certify that the thesis I am submitting is entirely my own original work except where otherwise indicated.

Heidelberg, Septemberg 28th 2020 .....

Table of Contents

CHAPTER 1

INTRODUCTION

Molecular Ions and Charged Clusters

Advancing spectroscopic methods allow to identify a growing number of atomic and molecular species in interstellar gas clouds, i.e. in regions where the formation of stars and planets take place. Despite the low particle density in these clouds, a rich chemical network is present and results in the formation of at least hundreds of molecules. As detected so far, some contain up to 12 atoms, like for example CH_3C_7N, and it is unclear how far the complexity continues. The fact that abundances of biological relevant molecules like for example H_2O and O_2 are not predicted correctly, shows that the routes of chemical reactions are often not well known. One approach towards a better understanding is to investigate the molecules which participate in these reactions. Key roles are often taken by molecular ions, e.g. in radiative and dissociative recombination processes as well as charge transfer reactions. Molecular ions can emerge from ionization by radiation sources. One starting point is the ionization of the most abundant molecule H_2 by stellar UV or cosmic ray impact. The H_2^+ ion rapidly reacts with other H_2 molecules and forms the trihydrogen cation H_3^+. The latter reacts with other species and more complex molecules are formed. Another example is CH_3^+, which is so reactive, and therefore short-lived, that it is difficult to detect. A review on astrochemistry is provided by Fraser et. al. [1]. In planetary environments, processes involving molecular ions are of high importance as well. The ionosphere of the earth for example is dominated by NO^+ and O_2^+ ions over a wide range of latitude [2]. Here, molecules are ionized by solar radiation as well as impact ionization from atmospheric and auroral electrons. Rate coefficients for atmospheric reactions are still under debate [3]. One important reaction is dissociative recombination of O_2^+ which is the present-day major loss mechanism of Mars' atmosphere and probably part of the explanation how this atmosphere was lost in the past [4].

Physics experiments on molecular ions often aim for a better understanding of these reaction pathways by investigating the properties of the ions on an individual level. That means, the ions are prepared in the gas phase or an ion beam and brought to interaction with other particles, e.g. photons. Observing the interaction yields information on the molecule's geometric structure and internal states, e.g. vibrational and rotational states as well as electronic potential surfaces. With the advent of short-pulse laser systems during the last two decades, it even became possible to time-resolve molecular dynamics in so-called pump-probe schemes. The timescale for the formation or breakup of molecular bonds is tens of femtoseconds whereas electronic dynamics can occur within a few attoseconds. However, even more chemical processes occur in the condensed phase where molecules are not rather isolated as in interstellar clouds but bound to and strongly influenced by the surrounding matter. In many cases, the insights gained from gas-phase experiments on isolated molecules are not transferable to the same molecule in the condensed phase. A way to maintain the advantageous of gas-phase experiments, e.g. that the system under investigation is isolated from the environment, and at the same time study molecular dynamics with condensed-phase interactions are gas phase clusters. These are aggregates of a few up to several thousands of molecules and partly fall into the category of nanoparticles. A review on this topic is provided by Jan R.R. Verlet [5]. The TrapREMI setup developed during this thesis allows for the investigation of both, individual molecular ions as well as charged gas-phase clusters.

As described, the molecular oxygen cation O_2^+ is of high relevance for various processes. Chemical properties have been measured in a variety of reactions with other molecules [6] and its potential energy curves have been subject to theoretical [7] as well as experimental [8] investigations. However, although O_2^+ is diatomic and therefore of the simplest molecular structure, there is still uncertainty about many potential energy curves. These are often not accessible in single electronic transitions from the ground state and are of metastable nature which complicates their observance [9]. However, photodissociation channels accessible via infrared photon excitation are known [9, 10]. Therefore, we chose to measure this photodissociation as a commissioning experiment and proof-of-principle. Another molecular ion of major scientific interest is the methane cation CH_4^+. It is the simplest hydrocarbon and therefore the precursor of all other hydrocarbons which are produced in interstellar clouds. It is an important ingredient of atmospheric chemistry, plasma science and chemical manufacturing science [11]. As a prototypical hydrocarbon and polyatomic molecular ion, we additionally performed measurements on the photodissociation of CH_4^+.

The TrapREMI in the Experimental Landscape

The "targets" of investigation, molecular ions or gas-phase clusters, are usually prepared as beam, accelerated from a source into an experimental setup and brought to interaction with "projectile" particles. In most experiments, the projectiles are photons, electrons, neutrals or ions. This interaction induces a reaction which often leads to fragmentation of the molecule. To obtain information on the reaction, the resulting reaction products are collected on detectors of different type. Experiments differ in the way how the targets are prepared, i.e. how their motion and internal states are controlled. They also differ in the capabilities to detect different types of reaction products. In this section, we provide a brief overview on target preparation techniques and product imaging schemes. Thereafter, we compare the TrapREMI setup developed in this thesis to the existing experiments.

Preparation Techniques. Molecular ions are often investigated in fast beam experiments, i.e. the target is accelerated to a few keV of kinetic energy. This offers improved ion and neutral detection capabilities and high mass selectivity [12]. Fast beams are generated by accelerating ions from source to interaction region. The group of Robert Continetti at UCSD for example applies a linear, electrostatic acceleration stage, preparing ions with up to 60 keV [13][14]. A similar approach has been implemented by the group of I. Ben-Itzhak at KSU [15]. Fast ion beams additionally allow to implement merged beam methods to study reactions between ions with vanishing relative velocity, e.g. associative ionization and proton transfer [16][17]. The initial target state can be controlled to an even higher degree when the fast ion beam is trapped in oscillatory motion. Electrostatic storage devices, available for ion energies up to several hundred keV, offer multiple advantages for preparation of molecular ions: The energy spread in the target beam can be reduced by techniques like electron cooling and autoresonance cooling [18]. Long storage times on the order of seconds allow ions to relax internal excitations, e.g. become vibrationally cold [19]. Further, ion trapping allows for recycling of species which are difficult to prepare, enhancing the effective ion current. Electrostatic ion storage has been implemented as large-scale storage rings and linear, table-top devices. The latter are referred to as Electrostatic Ion Beam Traps (EIBTs). First developed by Daniel Zajfman and co-workers in 1997 [20], these traps and similar setups are now employed in various experiments: Continetti and co-workers extended their linear acceleration scheme by a subsequent, cryogenic EIBT, allowing to investigate the dissociative photodetachment of cold anions [21]. The group of Daniel Strasser at HUJI recently developed a Hybrid-EIBT which can store anions and cations simultaneously for multi-pass merged beam experiments [12]. At the MPIK, the Cryogenic Trap for Fast Ions (CTF) [22] and the large-scale Cryogenic Storage Ring (CSR) have been developed to prepare molecular ion targets in conditions resembling the interstellar medium [23].

Product Imaging Schemes. The investigation of molecular ion dynamics usually relies on fragmentation of the molecule. Experiments are set up to detect four types of reaction products: Cationic, anionic and neutral fragments from which in many cases information on the molecule's geometric structure and nuclear motion can be obtained as well as electrons in which the electronic structure can be encoded. Depending on the reaction, a product imaging scheme which measures only some product types can be sufficient. In many single-pass experiments, the fast beams are directed towards time-and-position sensitive detectors. This allows to detect all neutral and ionic products on an event-by-event basis and to apply coincidence imaging techniques [24]. In coincidence imaging, two or more individual products are detected which have originated from the same molecule and therefore are correlated. In multi-pass experiments however, the fast ion beam is stored in an EIBT. Only neutral products can leave this electrostatic trap to be detected. This scheme has been used to study for example SF_6^- photodetachment in the CTF [25]. To extend the imaging scheme in multi-pass experiments, Continetti and co-workers additionally placed an electron detector inside the EIBT, allowing for photoelectron-photofragment coincidence spectroscopy [26].

TrapREMI. We further extend this scheme by implementing a Reaction Microscope (REMI) in the EIBT. REMIs are versatile spectrometers which allow for coincidence spectroscopy on electrons and ions. Since extraction fields inside the REMI complicate the injection of charged targets, these setups have been mostly employed to investigate neutral atoms and molecules. To circumvent this complication, we implemented a longitudinal geometry. This allows to combine advantages in target preparation provided by an EIBT with the sophisticated imaging scheme of a REMI. The TrapREMI is a setup to perform multi-pass, fast beam experiments on molecular ions and detect all four possible reaction products on an event-by-event basis in coincidence. Our flexible EIBT design allows to trap cations as well as anions and even trapping them simultaneously in a merged-beam experiment is possible. This setup allows for a large variety of experiments. Reactions with the stored ions can be induced by various projectile sources, ranging from laser infrastructures which deliver IR-strong-field and XUV radiation over massive particle beams like supersonic gas jets and electron guns to large-scale radiation facilities like synchrotrons and free electron lasers.

Structure of this Thesis

The basic technologies which have been combined in the TrapREMI setup, EIBT and REMI, are reviewed in chapter 2. Chapter 3 is dedicated to the development process of the TrapREMI design. We present ion optics simulations and estimate basic limitations in product acceptance and experimental sensitivities and resolutions. In chapter 4, we present the final TrapREMI setup together with experimental accessories and describe signal processing and data acquisition. The ion production and bunch generation in this setup is described in chapter 5. Thereafter, we present the ion injection scheme for the EIBT and discuss characterization measurements of ion storage. In chapter 6, we present the first photodissociation experiment in the TrapREMI on stored O_2^+, constituting the commissioning of our setup. Finally, the photodissociation of CH_4^+ is presented in chapter 7.

CHAPTER 2

BASIC EXPERIMENTAL TECHNOLOGIES

The TrapREMI setup is a combination of two established technologies: a Reaction Microscope (REMI) inside an Electrostatic Ion Beam Trap (EIBT). This chapter reviews the generic experimental setups and operating principles of these technologies and outlines their performance.

2.1 Electrostatic Ion Beam Trap

Trapping charged particles requires a confining potential. The latter can be implemented in various ways. On one end of the spectrum, there are table-top techniques like Paul or Penning traps [27, 28], which utilize combinations of static and rotating electric as well as magnetic fields to confine ions in a small static region of space. On the other end there are large-scale storage rings like ESR at GSI Darmstadt which store fast ion beams with well defined momentum, using magnetic fields similarly to a synchrotron. The CSR at MPIK Heidelberg even operates with purely electrostatic fields. Besides long storage times, their advantage is that the oscillatory motion leads target ions which have not yet interacted with a projectile particle back to the interaction region after usually a few μs. This increases the effective ion current and efficiency of the experiment for particles which are difficult to produce or only available in small quantities [29]. An EIBT combines advantages from both ends of the spectrum: It is a table-top setup which can store fast ion beams in a linear, oscillatory motion. Purely electrostatic fields allow for storage of ions independent of their charge to mass ratio, enabling studies on heavy molecular ions and charged clusters [30].

2.1.1 Setup and Operating Principle

Using purely electrostatic fields, ions are reflected between two mirrors and confined to a cylindrical region in space, similarly to photons in an optical cavity. Figure 2.1 shows the original realization of this technique by Daniel Zajfman in 1997. It is composed of two stacks of opposing ring electrodes to which electric potential can be applied. As illustrated in figure 2.2, the resulting potential landscape generically consists of two ion optical elements: Reflecting potential barriers which enclose the trap region longitudinally as electrostatic mirrors and traversable potential barriers, below the ion kinetic energy, which focus the stored ion beam onto the trap axis as so called Einzel-lenses. A typical scheme of the latter is shown in figure 2.3: Electric potential is applied to three electrodes. Usually, the center electrode lies at higher potential V_2 than the outer ones at V_1. The resulting potential barrier is illustrated on the bottom. Ions, starting at V_0, traverse the potential barrier from the left and pass regions of different potential curvature. The effect of the latter is indicated by small arrows: Left-handed curvature, i.e. at the foot of the barrier with $\frac{d^2V}{dz^2} > 0$, acts defocusing and right-handed curvature around the top of the barrier with $\frac{d^2V}{dz^2} < 0$ acts focusing. The overall effect is focusing because the ions slow down when traversing the barrier and spend most of the time in the focusing region around the top. This element can also be implemented with reversed potentials $V_2 < V_1$, i.e. with a potential well instead of a barrier. Then, the curvatures are reversed but the net effect is still focusing. Interestingly enough, every traversable ion optics element is focusing. The principles of charged particle optics have been described extensively by Hinterberger [31] and Liebl [32].

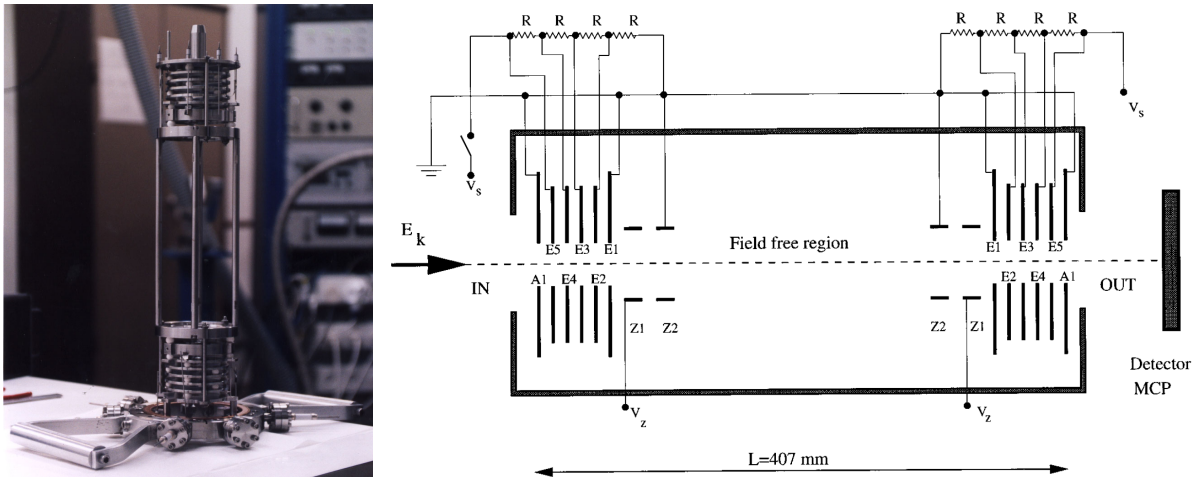

Figure 2.1: (left) Photograph of the original EIBT, set up in the Molecular Physics Group at the Weizman Institute in Rehovot, Israel in 1997 [33]. (right) Schematics of electrode design, electronic circuitry and operational principle. Funcional elements are mirror electrodes (E1-E5), lens electrodes (Z1,Z2) and the MCP detector on the right. The smallest inner electrode diameter is 16 mm and the field-free region has a length of 245 mm [30].

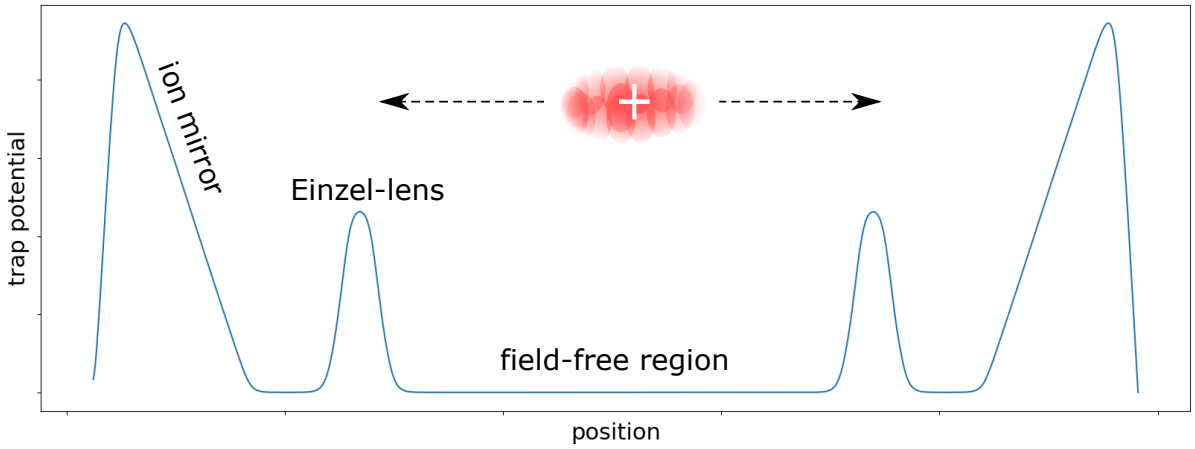

Figure 2.2: Exemplary electrostatic potential along the symmetry axis of an EIBT (indicated by dashed line in figure 2.1). The illustrated ion bunch in red is trapped using two ion optic elements: mirrors, between which the ions are reflected and Einzel-lenses which focus them onto the trap axis. The potential has been extracted from ion optics simulations using SIMION.

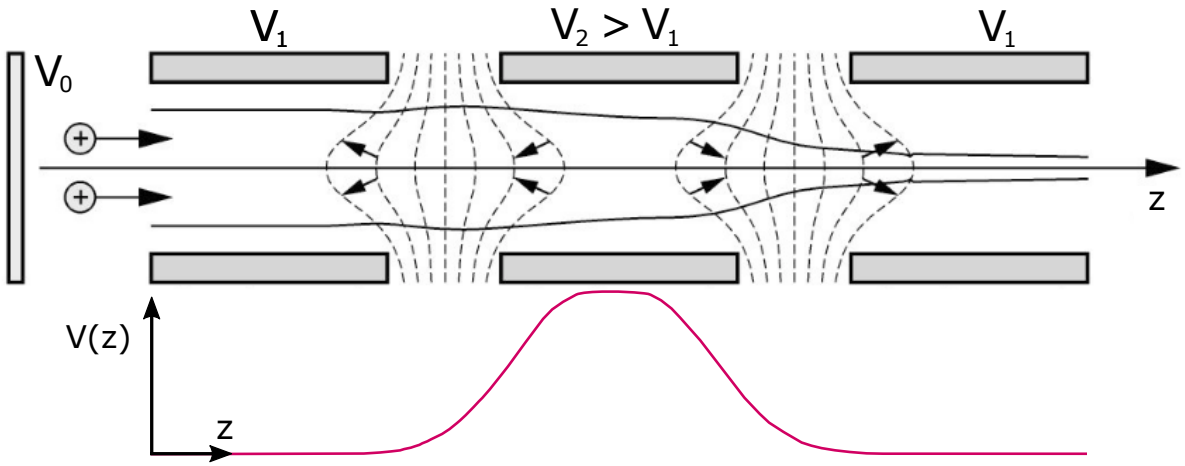

Figure 2.3: Generic Einzel-lens schematics (top): Three electrodes, i.e. cylindrical or rectangular apertures, are aligned along an axis z. At the center electrode, higher electric potential is applied than on the outer ones such that a potential barrier (bottom) is generated. As implied by small arrows, the curvature of this barrier effects the ion trajectories: Left-handed curvature on the foot of the barrier acts defocusing and right-handed curvature on both sides of the top of the barrier acts focusing. The overall effect is focusing since the ions spend more time around the top. Equipotential curves are indicated by dashed lines. Figure adapted from [34].

Stability criteria for these elements to trap ions have been derived by Dahan et.al. [30]: The mirror potential has to exceed the overall ion energy per charge and the focus length f has to exceed a quarter of the trap length L:

$$V_{mirror} > \frac{E_{ion}}{q} \qquad and \qquad \frac{L}{4} \leq f \leq \infty \tag{2.1}$$

Means of measurement are an electrostatic pickup to monitor the stored ion beam in a non-destructive manner and an external micro-channel plate detector. The latter can detect ions which neutralize in the residual gas and leave the trap. Both techniques are discussed in more detail in section 5.2.

2.1.2 Advantages and Performance

The trap design features rotational symmetry which facilitates simulation as well as fabrication. Kinetic ion storage energy is not limited in principle but only by practical difficulties: available power supplies and proper insulation. High storage velocities facilitate the measurement of neutral reaction products which otherwise are too slow to cause events, e.g. on MCP detectors. The number of storable ions has been shown to exceed 10^7 [35] and is only limited by space charge effects and the brilliance of the ion source. Lifetimes of stored beams are limited by the vacuum conditions. Electron capture as well as elastic scattering in the residual gas can be the dominating loss mechanisms for long storage times [30]. For these processes, the ion beam lifetime depends on ion species, ion velocity v and residual gas density. Table 2.1 provides lifetime literature values in EIBTs for the energy range applicable to the TrapREMI. Further, an EIBT is a multi-pass mass spectrometer. The frequency spectrum of ion oscillation allows to identify species of different charge to mass ratio. Kick-out mass selection can be performed by pulsing the potential on a trap electrode. The dynamics of stored ion bunches can be controlled as well by time-varying electrode potentials which is referred to as RF-bunching [22]. Important for this project, an EIBT features a field-free region in the center. This offers the possibility to combine it with a field-sensitive experimental setup like a Reaction Microscope.

Ion Species	E [keV]	P [mbar]	Ion Count	τ [ms]	Reference
CO^+	4.2	1.5×10^{-8}	$10^2 - 10^3$	42	Zajfman1997 [20]
Ar^+	4.2	10^{-9}	10^5	160	Pedersen2001 [36]
N_2^+	7.1	8×10^{-14}	10^5 - 10^6	>300.000	Froese2012 [37]

Table 2.1: Literature examples of ion beam lifetimes in electrostatic ion beam traps.

2.2 Reaction Microscopes

A Reaction Microscope is a versatile experimental setup to investigate atomic and molecular fragmentation reactions. Combining electron and ion momentum spectroscopy, it allows to access the full 3D-momentum distributions of all charged reaction products with full solid angle acceptance. REMIs can detect all products of a single reaction in coincidence and therefore allow to obtain kinematically complete information. Combined with a pump-probe scheme, REMIs allow the time-resolved investigation of various processes like molecular isomerization and dissociation or internal dynamics like wave-packet oscillations. REMI experiments are employed in various research areas, ranging from classic electron-atom collisions [38] over atomic interactions with attosecond XUV pulses [39] to even cluster studies at DESY's free-electron-laser [40]. A review of REMI technology and topical overviews are provided by Moshammer et al. [41, 42], and Ullrich et al. [43].

2.2.1 Setup and Operating Principle

A generic REMI setup is displayed in figure 2.4. The reaction is induced by crossing a target with a projectile beam under ultra high vacuum (UHV) conditions. In this example, atoms from a supersonic gas jet are ionized by two laser pulses in a pump-probe scheme. The emerging charged fragments, ions and electrons, are extracted from the interaction region by an electric field $\vec{E}$. The latter is applied by spectrometer electrodes and accelerates the fragments towards time- and position sensitive detectors. Due to momentum conservation and mass differences, velocity and energy of produced electrons are usually much higher then of produced ions. Thus, to project the electrons efficiently onto the detector and increase their acceptance, they are additionally confined to a spiral trajectory using a magnetic field $\vec{B}$, applied by Helmholtz coils. The extraction fields can be either homogeneous for simple extraction or used as ion optics to optimize the particle projection onto the detectors for a specific purpose.

2.2.2 Time-and-Position Sensitive Particle Detection

REMI Detectors usually consist of two core elements which are illustrated in figure 2.5: **Microchannel Plates (MCPs)** are used to obtain information on the impinging particle timing with a resolution well below 1 ns. An MCP is an array of channels, engineered through an insulating plate of several cm diameter and approx. 2 mm thickness. The channels are typically 10 µm in diameter, regularly distributed in a dense array with 15 µm spacing and coated with a low-work function material like GaP or GaAsP. Each channel acts as signal amplifier via secondary emission of electrons with a gain factor of up to 40 dB. When stacking multiple MCPs, the gain can be increased to 70 dB [44]. MCPs can be used for the detection of all particles which induce secondary electron emission, e.g. electrons, ions, neutrals and photons. The detection efficiency depends on physical properties of the MCP like the coating material and tilt angle of

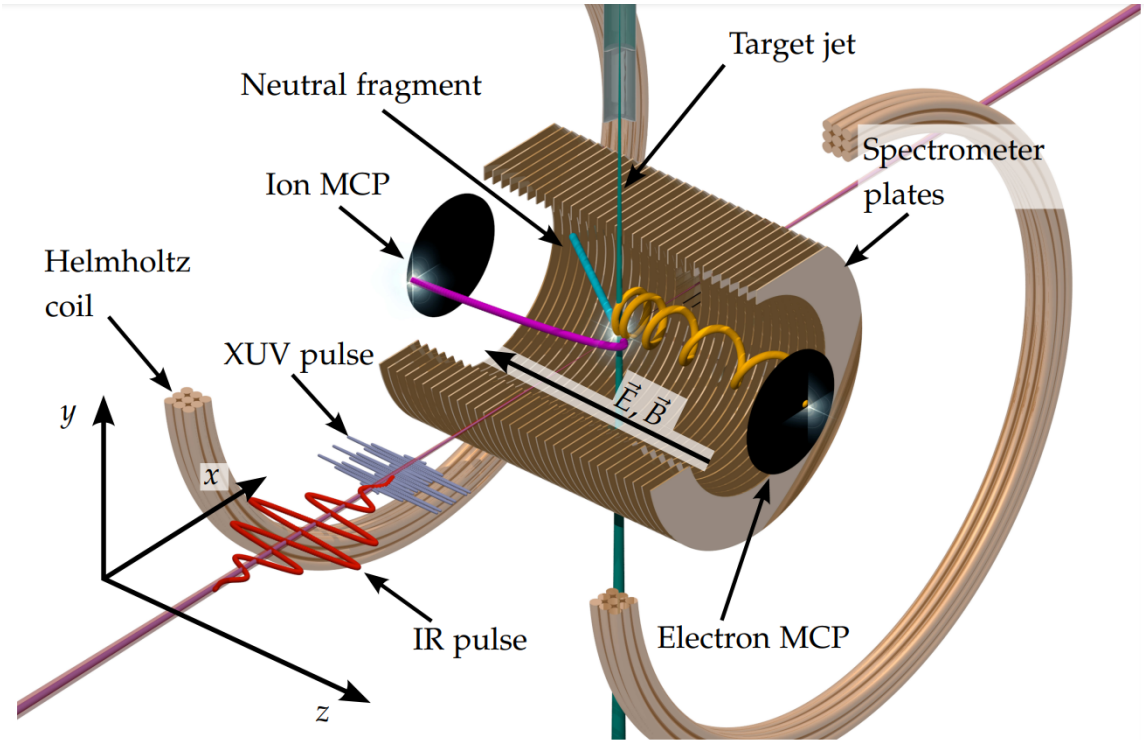

Figure 2.4: Reaction Microscope, exemplary ionization of a neutral target by XUV and IR laser pulses in a pump-probe scheme. The neutral target is injected as a supersonic gas jet. Ring-shaped spectrometer electrodes are used to apply an electric field by which the charged reaction products are extracted towards the detectors. An additional magnetic field, applied by Helmholtz-coils, forces the electrons on a spiral trajectory, thereby increasing their acceptance. The magnetic field effect on the ion trajectory is much smaller. In conventional REMIs, neutral fragments are not detected. Figure adapted from [10].

the channels. A major contribution is the open area ratio, i.e. the ratio between the area covered by channels and the total area, which ranges between 60 % and 80 %. Further, the efficiency increases with the particle's charge and velocity but decreases with it's mass [45]. J.L. Wiza provides an introduction to MCPs [46] and recent developments are described by Cremer et al. [47].

Delayline Anodes (DAs) are established setups for the detection of particle positions [48]. They consist of usually $\varnothing$ 0.2 mm copper(99 %)-zirconium(1 %) wire (the "delayline") wound around a metal body (the "anode") with a pitch distance of 0.8 mm. Usual resolutions are well below 50 µm and thus much superior to pixel-based detectors. Figure 2.5 shows a conventional "quadanode" configuration with two perpendicular delaylines, one for each spatial dimension. Multiparticle hits can be detected if the relative arrival time is longer then the electronic pulse width in the delaylines, resulting in a usual dead time of 10 to 15 ns. The advanced "hexanode" configuration uses three delaylines to further decrease the dead time. This is discussed in more detail in section

3.3. A detailed description of MCP/DA detectors can be found in [49] and the read-out electronics used in this project are discussed in chapter 9.

When a fragment ion or electron impinges a channel of the MCP, it can induce the emission of secondary electrons. As depicted in figure 2.5, a voltage of about 1 kV per MCP accelerates the electrons through the tilted channel, creating an electron avalanche. The corresponding electric signal, capacitively coupled out, provides information on the particle time-of-flight (tof) from the interaction region to the detector. The electron avalanche then leaves the MCP on the back surface and impinges on the DA. As depicted in the bottom of figure 2.5, this cloud covers multiple delayline windings and then spreads in both directions. The timing when the resulting electronic pulses reach the two ends of the respective delayline is denoted T_2 and T_1. The relative timing yields information about the primary particle hit position:

$$\begin{pmatrix} x \\ y \end{pmatrix} \propto \begin{pmatrix} T_2^x - T_1^x \\ T_2^y - T_1^y \end{pmatrix} \tag{2.2}$$

Since the initial cloud covers multiple delayline windings, the measured pulses are superpositions of pulses which started at different delayline position. This constitutes an intrinsic center-of-gravity averaging of the anode and thus a resolution much better then the winding pitch distance. As shown in figure 2.5, usually approx. 2500V are applied between the MCP front and the DA. For ion detection, the MCP front is set to high negative voltage in order to accelerate the positively charged ions on the last millimeters which increases the MCP efficiency. For electron detection, the front is set to a moderate, positive voltage. From the time-of-flight to the detector and the position on the same, the initial momentum vectors can be reconstructed using classical calculations, namely by solving the equation of motion imposed by the general Lorentz-force $m\ddot{\vec{r}} = q(\vec{E} + \dot{\vec{r}} \times \vec{B})$. Uncertainties in the reconstruction are the homogeneity of the extraction fields and the level of accuracy to which they can be controlled, as well as spreads in initial position and momentum of the particles. In section 3.4.2, we describe the momentum reconstruction regarding the TrapREMI. Further discussions of this in other REMI experiments can be found in [10], [50] and [44].

2.2.3 Acceptance and Resolution

The performance of a REMI ultimately depends on the specific design and the actual experiment: on the used target and projectile, spectrometer length and detector size and on the extraction field strengths. Since these parameters can vary strongly, we just want to provide a basic idea of REMI performance by an exemplary experiment in a usual REMI: the ionization of oxygen atoms from a supersonic gas jet by XUV laser pulses [10]. The REMI acceptance for ions and electrons can reach full 4π solid angle if the extraction fields are strong enough to project all reaction fragments onto the detectors, independent of their emission direction. As derived in

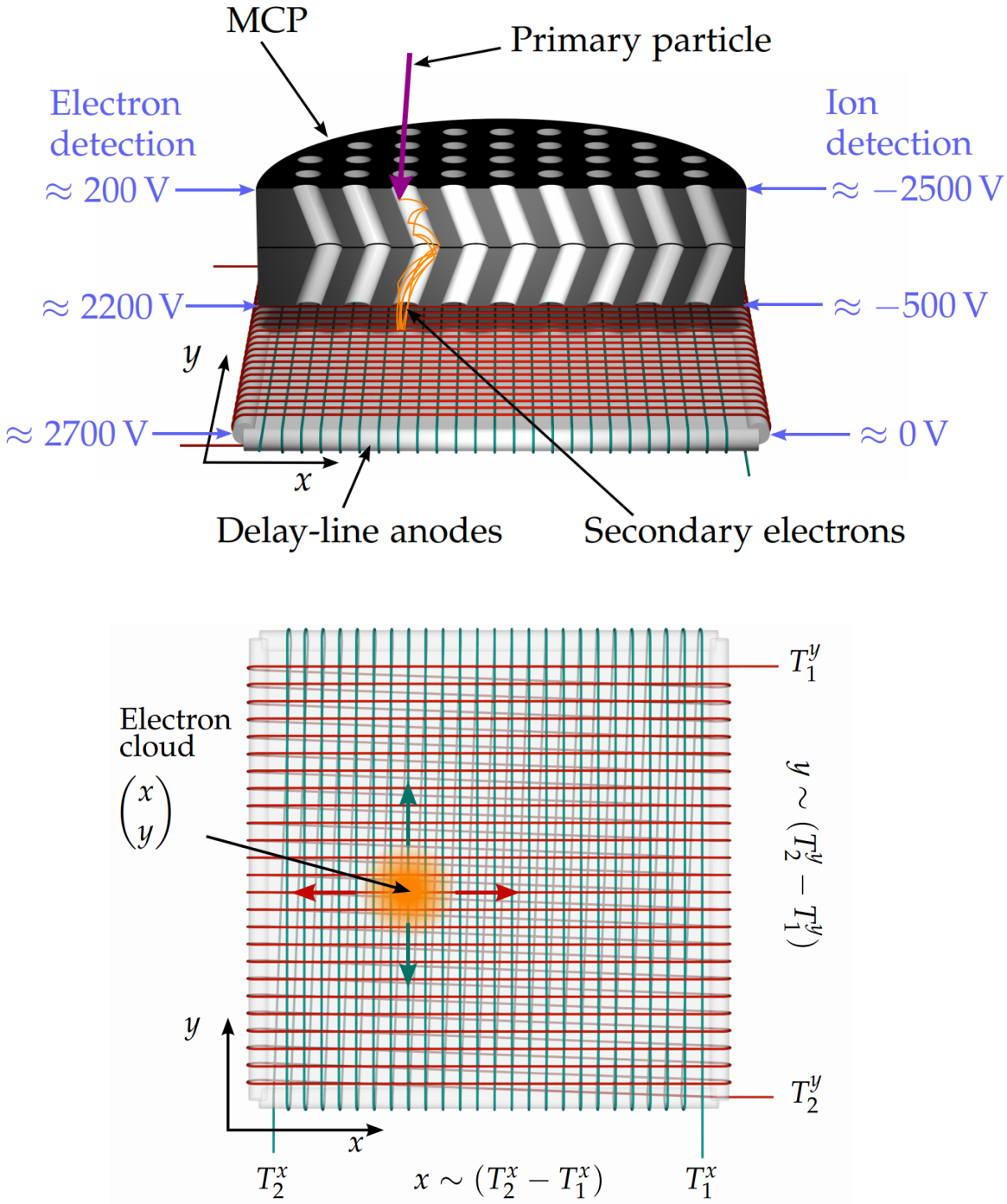

Figure 2.5: (top) Generic REMI detector setup: MCP-pair in cutaway-drawing followed by DA. An impinging primary particle initiates secondary electron emission in a micro channel. The applied voltage accelerates the electrons through the channel, creating an electron avalanche. The latter causes a voltage drop which is coupled out capacitively and used as timing signal of the impinging particle. On the sides, typical voltage configurations for electron and ion detection respectively are shown. (bottom) Position detection scheme: The electron avalanche exits the MCP and hits the delaylines (orange cloud). It spreads in both directions and is detected at the end of the lines. The difference in arrival time yields information on the hit position. Figure adapted from [10].

[10], the kinetic energy which the fragments can maximally have in a direction transverse to the REMI spectrometer axis is given by

$$E_{ion}^{trans} < \left(\frac{R_{MCP}\sqrt{Uq}}{2L} \right)^2 \approx 3eV \tag{2.3}$$

$$E_{ele}^{trans} < R_{MCP}^2 \frac{e^2 B_z^2}{8m_e} \approx 22eV \tag{2.4}$$

The right side indicates exemplary the order of magnitude of fragment energies in usual experiments with an MCP radius of $R_{MCP} = 40\,\text{mm}$, a spectrometer half-length of $L = 135\,\text{mm}$, a spectrometer voltage of $V = 136\,\text{V}$ and a magnetic flux density of $B = 7.9\,\text{G}$ [10]. A trade-off has to be made between acceptance and momentum resolution. While ions with higher energies can be accepted using shorter spectrometers and higher field strengths, the same decreases the resolution. Exemplary momentum resolutions for O^+ ions, which we detect in the photodissociation experiment described in chapter 6 as well, have been measured to be

$$\Delta p_z^{exp} \approx 1.5 a.u. \quad \text{and} \quad \Delta p_{x,y}^{exp} \approx 7 a.u. \tag{2.5}$$

These values have been obtained experimentally and thus include all contributions: spectrometer properties, preparation of target and projectile beam, mass of the measured species, field inhomogeneities and detector misalignments. General discussions of these contributions can be found in [51] (sec. 4.5), [10] (sec. 4.2.3) and [44] (sec. 4.3.2). In section 3.4.3, we discuss the sources of uncertainties in the TrapREMI setup and in section 6.4, we extract momentum resolutions from the photodissociation experiments.

CHAPTER 3

DEVICE COMBINATION: DESIGN AND SIMULATIONS

Starting from scratch, we developed a basic design which was put to test against ion optics simulations and technical feasibility. In parallel, we iteratively developed a 3D construction model together with the MPIK construction department. In this chapter, we outline this process of design development. First, we present the basic idea of a longitudinal configuration in section 3.1. Thereafter, we outline the ion optics simulations which have been performed to define the EIBT design in section 3.2 and present the REMI design in 3.3. In the last section 3.4, we estimate the acceptance and momentum resolution in the TrapREMI.

3.1 Longitudinal Configuration

In a conventional REMI experiment as described in section 2.2, the neutral target is injected perpendicularly to the spectrometer axis. After traversing the REMI, it is collected in a beam dump to maintain UHV conditions. In principle, this is possible with ionic targets as well. However, they are deflected by the REMI extraction fields. This heavily complicates the REMI operation: In contrast to neutral targets, the beam position then depends on ion species, energy and extraction fields. This causes extra work when adjusting the overlap of target and projectile beam, particularly when the target species is changed frequently. Additionally, the extraction fields alter the exit position of the target beam. The requirement of dumping it properly therefore unfavourably constrains the REMI field strengths. Obviously, this is even more complicated when ions should be stored, oscillating through these fields.
To avoid these drawbacks, we chose a longitudinal configuration where REMI and EIBT share the same symmetry axis. In figure 3.1, a 3D model of the REMI is shown. As in the conventional design, a reaction is induced by crossing target and projectile beam under UHV conditions. Electric and magnetic fields are applied by spectrometer electrodes and Helmholtz coils respectively to

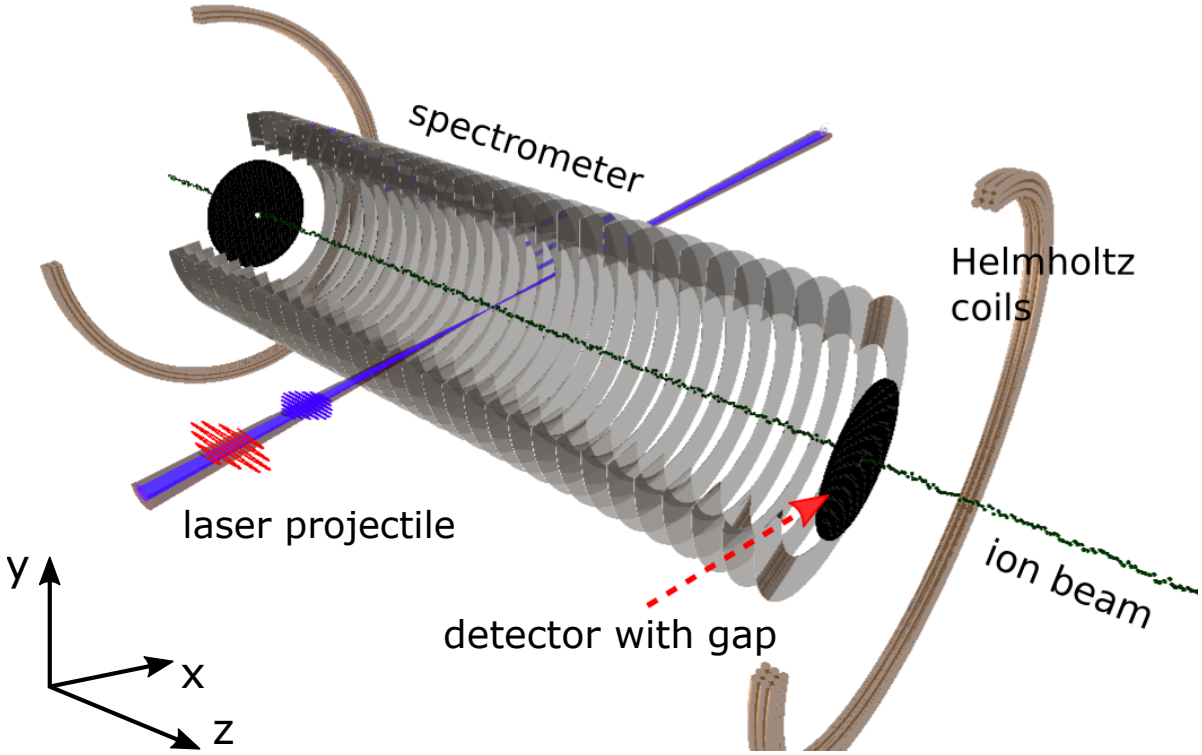

Figure 3.1: Illustration of longitudinal configuration: The REMI consists of the same functional elements as in the usual design described in 2.2. However, the target beam is not injected perpendicular to the spectrometer axis but oscillates parallel to the same, stored in the EIBT. Thus, the ion trajectories are not influenced by the REMI fields. This requires the detectors to exhibit a central gap through which the ions can oscillate. The REMI is embedded in the EIBT which is not displayed here (see figure 3.2). The symmetry axis is defined as z-axis and the detectors are aligned with the x,y-plane.

extract charged products to MCP/DA detectors. The reaction target is an ion beam, stored in the EIBT. The REMI is embedded in the field-free region between the trap electrode stacks which are not depicted here and the stored ions oscillate through the REMI. In contrast to the conventional design, the target beam is not injected perpendicularly but along the REMI symmetry axis. Therefore, the ions oscillate along the REMI extraction fields lines which minimizes the effect on the storage capacity. There are challenges going along with this longitudinal configuration. The stored ion trajectories intersect the REMI detectors which therefore feature a central gap for the ions to pass through. This imposes restrictions on both, REMI and EIBT capabilities: The detection area in the center is lost due to the gap. To maintain sufficient detection area on the rest of the detector, a more complex detector concept is necessary, namely a DA in hexanode configuration (see section 3.3.2). The detector gap also constrains the accessible phase space of the trap, decreasing it's acceptance as simulated in section 3.2.3 and the maximum number of stored ions. The ion beam lifetime is not expected to be altered by the central gap. Figure 3.1,

introduces the coordinate system which is used throughout this thesis. The symmetry axis is defined as z-axis and the detectors are aligned with the x,y-plane.

Electrode Arrangement. Figure 3.2 shows the TrapREMI electrode arrangement. The REMI electrode stack is embedded in the field-free region of the EIBT. All electrodes share a mutual symmetry axis. In this way, the reaction products are not influenced by the trapping fields. The EIBT electrode design is discussed together with the underlying simulations in more detail in section 3.2.

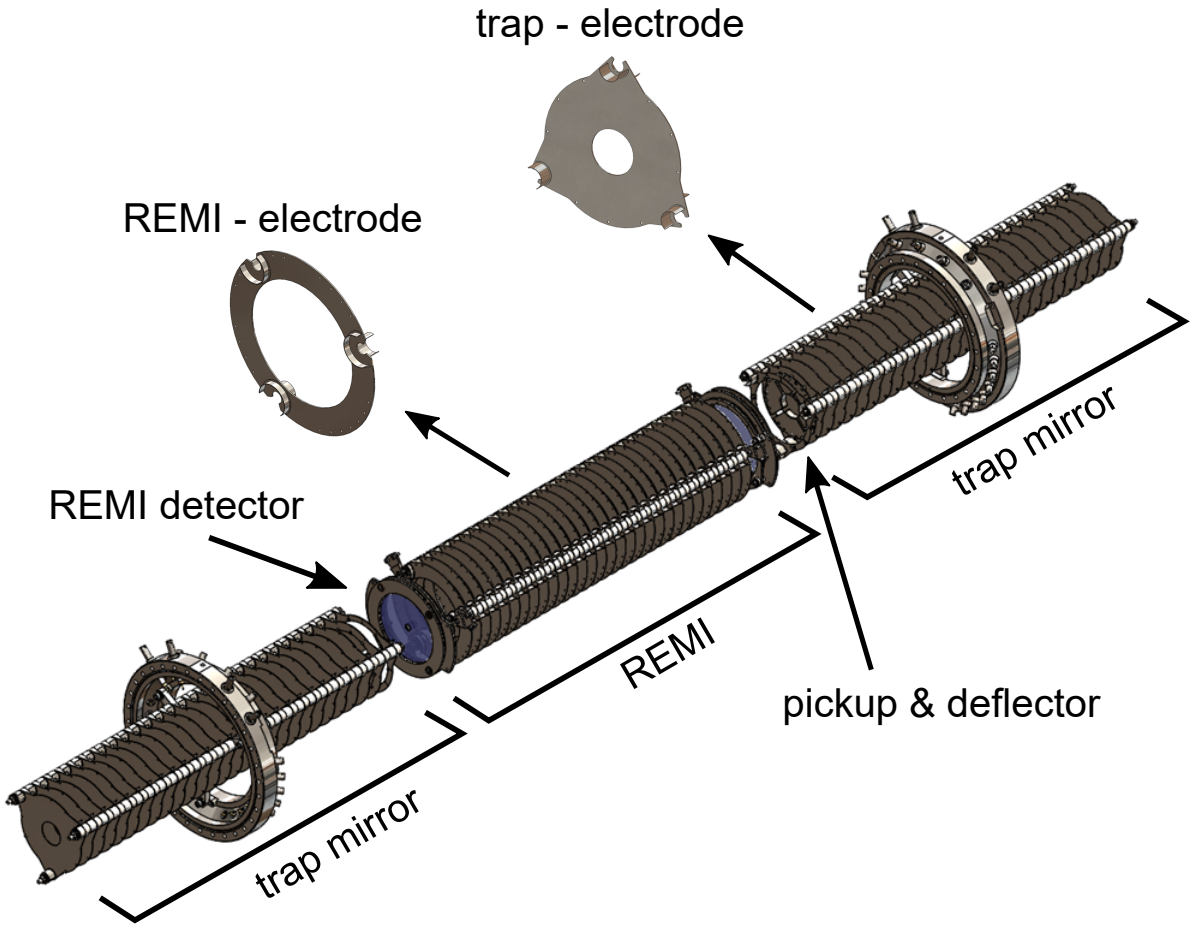

Figure 3.2: Arrangement of REMI electrodes, embedded in the field-free region between the EIBT electrode stacks. The stacks are mounted on flanges with HV-feed-throughs. Different electrode designs have been chosen: In the EIBT, a small inner diameter hinders potential reach-through from the vacuum chambers. In the REMI, reaction products can approach the detector on trajectories far away from the trap axis and thus a larger inner diameter is required. For illustrative purposes, the Helmholtz coils are not displayed.

Modular Design. The 3D model in figure 3.3 depicts the mechanical structure around the electrode stacks. The electrodes of EIBT and REMI are housed in DN200 vacuum chambers which are mounted on three alignment tables. Since the chambers are mechanically decoupled by stainless steel bellows, these tables can be used to individually align each electrode stack. The alignment on a mutual axis is crucial to efficiently trap ions and can be performed optically with a precision of 100 µm. All three tables can be translated on rails. Therefore, this modular design enables to open the setup at the EIBT/REMI junctions and access electrodes or detectors. The latter can be implemented as individual modules as well and are further discussed in section 3.3.2. The TrapREMI vacuum chambers exhibit an overall length of about 2.26 m and are mounted on an aluminum ITEM frame (blue). This setup is less compact than the original EIBT but still can be transported to perform experiments at large-scale radiation facilities.

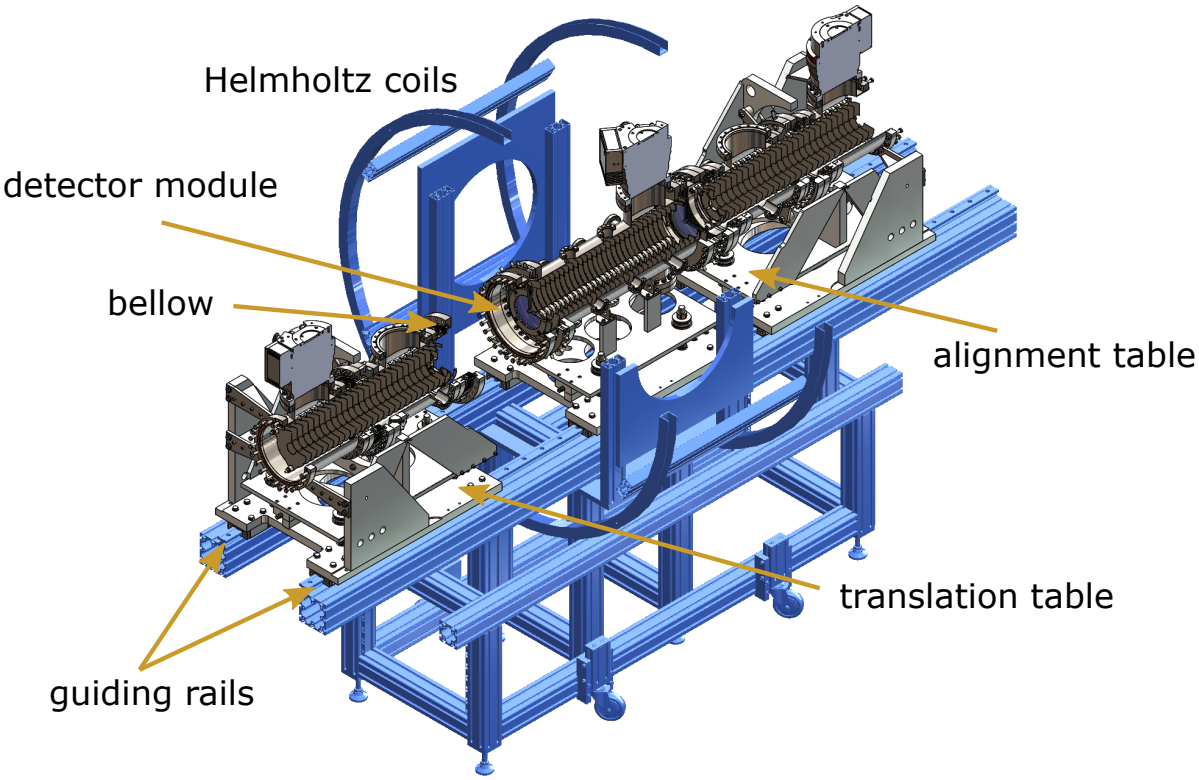

Figure 3.3: Vacuum chambers which house the EIBT and REMI electrodes, mounted on three individual alignment and translation tables. The chambers are separated by four stainless steal bellows and can thus be aligned individually. Translation tables allow to move apart EIBT and REMI sections on guiding rails. This modular design facilitates the access to inner parts like electrodes and detectors. In blue, we show the ITEM frame and Helmholtz coils.

3.2 Ion Optics Simulations of the EIBT

The trap design has been tested and refined for its capabilities using ion optics simulations in SIMION. This software allows to simulate particle trajectories in electric potentials for a given 3D electrode geometry. The potentials are calculated by solving Laplace's equation with Dirichlet-type boundary conditions. A detailed documentation can be found in [52]. The physics of ion optics is described in the book "Ion Optics with Electrostatic Lenses" by Frank Hinterberger [53].

3.2.1 Potential Simulations and Electrode Design

The EIBT electrodes are supposed to generate a well controlled potential landscape. Any potential curvature which is not intentionally applied should be avoided since it alters the ion trajectories. Therefore, the electrodes have to effectively shield the trap axis from the surrounding vacuum chambers to avoid potential reach-through. Additionally, minimum curvature should be introduced by the geometric electrode design. Given the rotational symmetry of EIBT and REMI, an obvious geometric choice is a ring electrode. The optimal geometric parameters have been determined by simulating the generated potential. An example is shown in figure 3.4. On the left, we show the potential in one half of the EIBT, i.e. ion mirror and Einzel-lens. It is plotted against the position along the trap axis (z) and the position transversal to it (y). The trap axis is indicated by a red line. The mirror potential, which is applied to be a linear ramp, is altered periodically. The amplitude of this modulation increases for larger distances to the trap axis, i.e. towards the electrodes. This is clarified on the right, where we plot the electric field strength, i.e. the gradient $\frac{dV}{dz}$ along the trap axis. In the mirror region, the simulated field strength shows clear oscillations.

For a given distance between the electrodes, the amplitude of these oscillations decreases with increasing inner electrode diameter (ID). However, since the potential drops from the ring electrode towards the trap axis, an increasing ID leads effectively to a smaller applied potential. An ID of 40 mm is a good trade-off, resulting in small relative field strength oscillation amplitude on axis (2.4%) while still maintaining a large fraction (89%) of the applied voltage at the trap axis. Other parameters are the electrode thickness and the distance between neighbouring electrodes. For smaller distances, a better shielding of the trap axis is achieved. However, this requires a higher number of electrodes. As trade-off between shielding and practicability, we chose 26 disc-like electrodes as depicted in figure 3.2 with a thickness of 1 mm and a distance of 25 mm. The outer diameter was chosen to be 154 mm which is a trade-off between shielding and the necessary space for electric wiring.

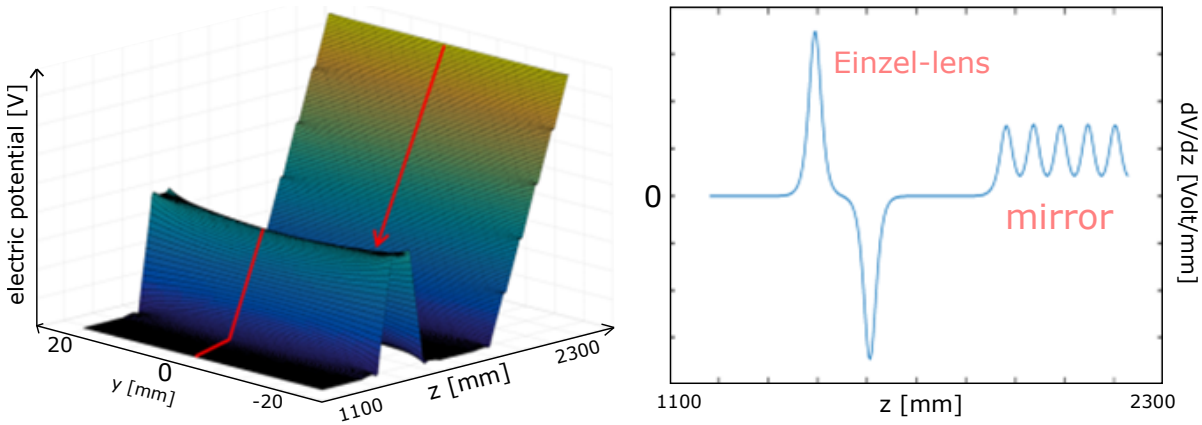

Figure 3.4: (left) SIMION simulation of EIBT potential. The red line indicates the trap axis. The generated potential is periodically modulated. (right) Electric field strength along trap axis. The oscillations in the mirror region are due to a combination of electric shielding and electrode geometry.

3.2.2 Electrode Stack Design

As shown in figure 3.2, we organize the trap electrodes in two opposing stacks with the REMI in between. In contrast to the original EIBT, the electrode stacks are formed by identical electrodes. That offers a high flexibility in forming ion optical elements: The positions, shapes and lengths of mirrors and lenses, i.e. the trap length and focusing properties, can be varied from the outside without opening the vacuum chambers. The electrodes are mounted on three ceramic rods and separated by ceramic insulators. The latter are shielded by stainless steel tube segments, also visible on the single electrode in figure 3.2, to prevent them from charging up. The distances and insulation between trap elements have been designed to store ions with a maximum kinetic energy of 10 keV. For maximum trap acceptance, the electrodes have to be aligned as good as possible: The electrodes in one stack should be parallel to each other and both stacks have to be aligned on the same axis. In simulations we determined a maximum tolerable tilt of individual electrodes of 0.05°. With a fabrication tolerance of 20 µm for individual dimensions, this is feasible to achieve. However, when mounting the electrodes and insulators, they have to be sorted by actual length and thickness so that fabrication deviations do not add up. Additionally, each EIBT stack is equipped with a 4-quadrant electrode. It can be used to steer the stored ion beam and compensate alignment imperfections. Further, we implemented a charge pickup electrode to monitor the stored beam as described in section 5.2.1 and a 4-quadrant deflector in each electrode stack.

3.2.3 Transversal Phase Space and Trap Acceptance

A charged particle beam which is stored by ion optic elements is described by the particle positions and momenta in a six-dimensional phase space. In ion optics, the coordinates are usually chosen relative to a reference particle. This so called synchronous particle moves along the ideal trajectory, i.e. the trajectory which the setup has been designed for. In the TrapREMI, the synchronous particle moves on the trap axis. As introduced in figure 3.1, x,y denote the dimensions transversal to the trap axis and z denotes the longitudinal direction. Since the TrapREMI is rotational symmetric, we can limit the description to one transversal dimension. For a certain position z on the trap axis, the transverse ion beam phase space is spanned by the ion's

$$\begin{aligned} &\text{distance to the trap axis} \quad x \\ &\text{and directional deviation} \quad x' = \frac{dx}{dz} = \frac{dx/dt}{dz/dt} = \frac{p_x}{p_z} \approx \frac{p_x}{p}, \end{aligned} \tag{3.1}$$

usually expressed in units of mm and mrad respectively. Here, p is the total ion momentum and x' is in good approximation the angle between the ion's propagation direction and the trap axis. The area which the ion beam occupies in phase space is the beam emittance

$$\epsilon^{1\sigma} = \sigma_x \sigma_{x'} \tag{3.2}$$

which describes the beam expansion and characterizes together with the beam brilliance the quality of an ion beam [53]. Here, the emittance has been defined on the basis of one standard deviation σ of the x and x' distributions for the case of a gaussian beam profile. The trap acceptance A on the other hand, is an important figure of merit for storage devices. It is the maximum emittance an ion beam can have in order to still be stored. If $A < \epsilon$, only the part of the ion beam which overlaps with the trap phase space can be stored. Ion optic elements can alter the form of the phase space area occupied by a beam but the emittance is conserved (Liouville's theorem).

Figure 3.5 exemplarily shows a phase space simulation in the TrapREMI. Using SIMION, we started argon ions with 2000 eV parallel to the axis, i.e. with $x' = 0$, and recorded their phase space coordinates each time they passed the trap center for approx. 1000 revolutions. This was repeated for varying distances x to the axis. In transversal phase space, the ions generically propagate on ellipses. However, other dynamics can be observed as well. As can be seen in this simulation (plotted in blue), we observed an ion which occupied only three small regions in phase space. That means, it returned every three revolutions to approx. the same coordinates. In an actual experiment, this can lead to the accumulation of perturbations and thus be an unstable trajectory. Apart from this example, the presented trajectories are stable. The corresponding area, indicated by the dashed, grey ellipse, is the trap acceptance A. Outside of this area, there are no stable trajectories. It was of interest how A would be influenced by the central gap in the REMI detectors. Table 3.1 displays the simulated values for different gap diameters. Without

detectors, i.e. with only the trap electrodes with an inner diameter of 40 mm as limiting element, we obtained 52 mm mrad. This is an acceptance comparable to other EIBTs [54]. Down to 14 mm, A is not influenced and then decreases rapidly. We used commercially available MCP/DA detectors as guideline which have for example gap diameters of 4.5 mm [55]. At this value, A is reduced by an order of magnitude. Ion storage is still possible, but only a fraction of the injected ions will be stored. This is not necessarily disadvantageous since only the total number of stored ions but not their density is decreased.

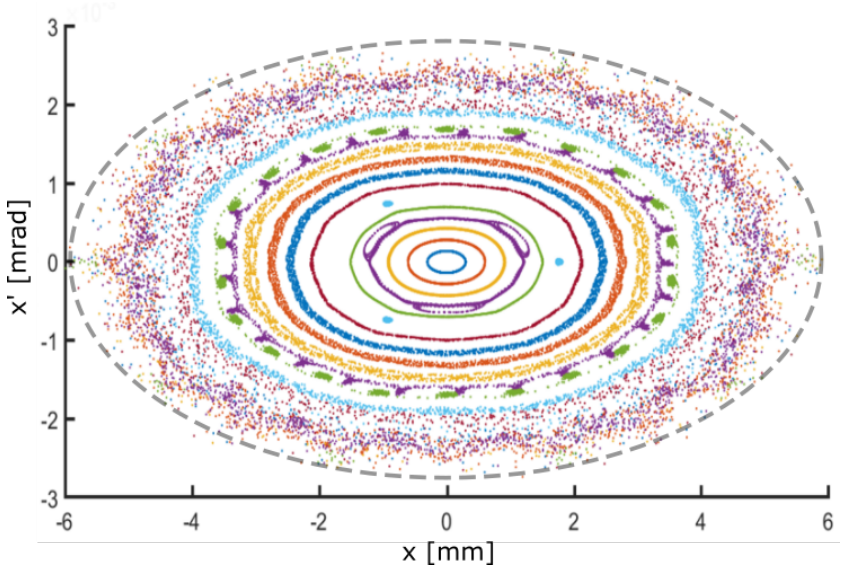

Figure 3.5: Exemplary simulation of trajectories in phase space. The area of the enveloping ellipse is the trap acceptance A.

⌀[mm]	40	14	12	10	8	4
A [mm mrad]	52	52	45	31.5	17.5	5

Table 3.1: Simulation results for trap acceptance A depending on the diameter of the detector gap. For the relevant diameter of 4 mm, A has decreased by an order of magnitude.

3.2.4 Magnetic Field Influence

Since the trap in this project is much longer than previous EIBTs, ions are further deflected by the earth magnetic field when propagating between two ion optics elements. We simulated the effects on ion storage by including a magnetic flux density component of $B_\perp = 0.5\,\mathrm{G}$ perpendicular to the trap axis. The results for Ar^+ and Cs^+ at 2500 eV kinetic storage energy are presented in figure 3.6. We plot the acceptance regions for $B_\perp = 0$ in black. For $B_\perp = 0.5\,\mathrm{G}$, the acceptance of Ar^+, has decreased to 65% (red) and the acceptance of Cs^+ has decreased to 70% (blue). The

magnetic field effect depends on the ion mass. From this simulation, it is expected that the majority of molecular ions can be stored in sufficient amounts. Only for very light ions like H_2^+, the acceptance is simulated to be close to zero. To store very light ions, the earth magnetic field has to be compensated by additional coils.

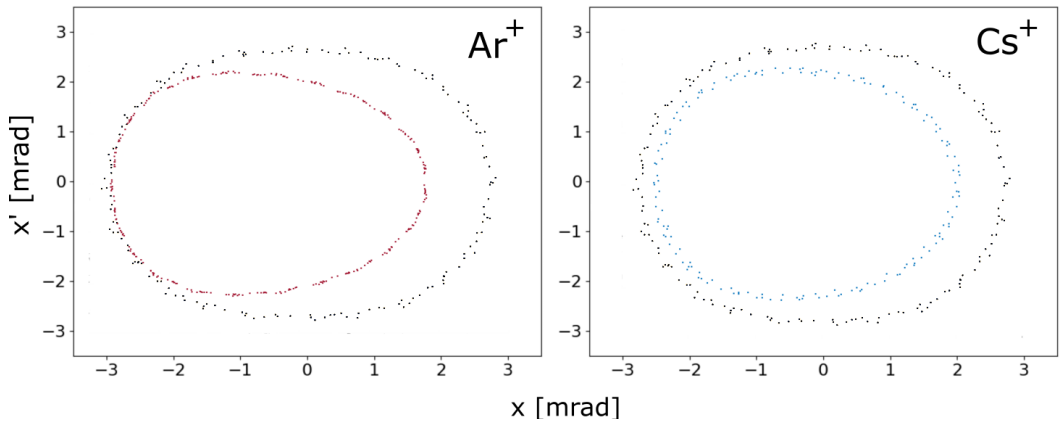

Figure 3.6: Earth magnetic field influence on trap acceptance, simulated by a 0.5 G magnetic flux density perpendicular to the trap axis in SIMION. (left) Ar^+ acceptance decreases to 65%. (right) Cs^+ acceptance decreases to 75%.

The ions revolve with a finite angle to the axis and are therefore also slightly influenced by the REMI magnetic field. Further, the Helmholtz coils do not generate a homogeneous magnetic field along all the trap axis but only in the REMI region. To take these effects into account, we implemented a pair of Helmholtz coils in the simulation which produced a magnetic flux density of $B_\parallel = 20\,\mathrm{G}$ in the REMI center. This is the maximum value which the Helmholtz coils are designed to produce in this setup. Again, we simulated Ar^+ ions with 2500 eV kinetic energy. The results are shown in figure 3.7: The ion trajectories are altered by the magnetic fields, but in both cases the acceptance remains the same.

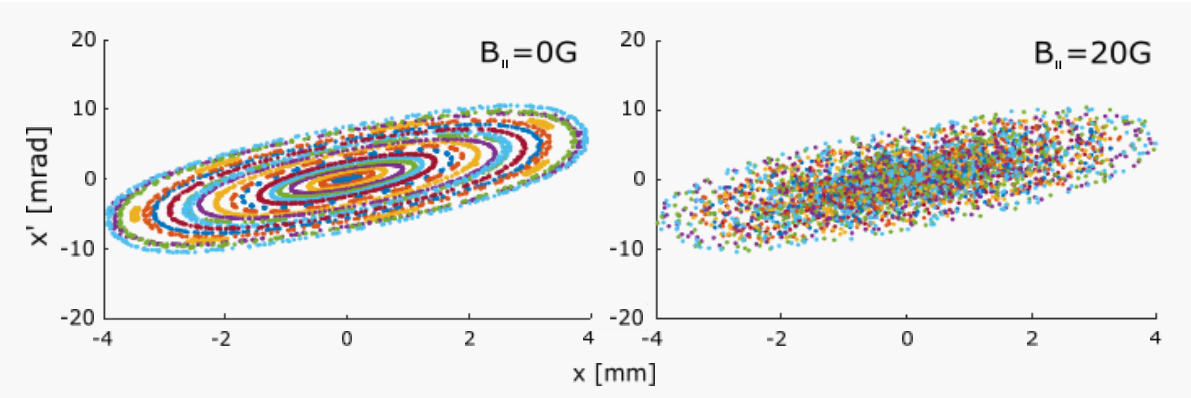

Figure 3.7: Simulated influence of magnetic field parallel to trap axis, applied by Helmholtz coils.

3.3 Reaction Microscope Design

This section describes how we modified the usual REMI design to optimize product acceptance and momentum resolution and at the same time meet the requirements imposed by the longitudinal configuration, in particular on the REMI detectors.

3.3.1 Spectrometer

An interesting feature of the longitudinal TrapREMI design is that, contrary to a usual REMI described in 2.2, momentum resolution and acceptance can both increase with spectrometer length since the ions are stored with high momentum towards the detector. In many experiments the challenge will be to ensure that the fragments have sufficient time to travel far enough outwards from the trap axis in order to hit the detector rather than passing the central hole. This is certainly only true for small reaction energies. In other cases, e.g. in coulomb explosion experiments where the products can gain several eV [56], the spectrometer voltage as well as the storage energy can be varied to maximize the acceptance. Thus, with 700 mm, we roughly tripled the usual spectrometer length. Figure 3.2 presents the spectrometer, placed in the field-free region between the trap electrode stacks. It is an array of 30 ring electrodes with a spacing of 20 mm. The electric extraction field generated by the spectrometer should be as homogeneous as possible in order to allow for accurate reconstruction of the product momenta as described in section 3.4.2. Field inhomogeneities increase close to the electrodes as well as due to potential reach-through from the grounded chamber walls. Since the maximum radial distance of a product is defined by the MCP radius of 40 mm, we set an inner diameter of 120 mm. An outer diameter of 172 mm was a good trade-off between manual accessibility and shielding of the chamber walls.

3.3.2 Hexanode Detector

In order to minimize the loss of detection area due to the central gap, we implemented MCP/DA detectors (see section 2.2.2 ff.) in hexanode configuration. Figure 3.8 displays a 3D model which has been developed based on a version implemented by the group of Alexander Dorn at MPIK. The central gap imposes a missing stripe in each delayline layer. In a usual quadanode configuration, this stripe would constitute a loss in detection area. A hexanode configuration can compensate this loss by using three layers, arranged with 120° relative angle. The red circle indicates the detection area, defined by the MCP radius. The whole detection area, except of the central gap, is covered by at least two delayline layers. Each layer consists of two copper(99%)-zirconium(1%) wires, constituting signal and reference line respectively. As described in section 4.3, the difference signal between these two lines is generated to filter out electronic noise (common-mode rejection).

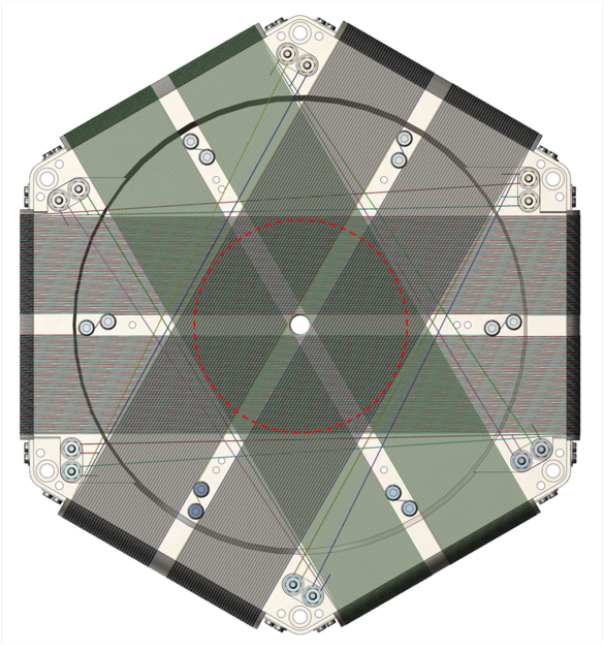

Figure 3.8: 3D model of stainless steel anode body, wrapped by 3 layers of delaylines. The red circle denotes the area covered by the MCP. Each delayline layer features signal and reference line with a thickness of 0.2 mm, spaced by 0.3 mm. The pitch distance for each winding is 1 mm.

Figure 3.9 displays a cut through the inner elements of the detector [1]. The 8 cm long detector tube consists of an inner stainless steel tube, electrically insulated by a ceramic tube. The tube potential can be controlled in order to ensure optimal ion storage. To provide a homogeneous termination of the REMI extraction field, the tube and grid potential are usually set to equal values. The grid can also be used to repel products with a certain charge or energy. The first delayline winding starts at 9 mm diameter and the position detection on the next 2 mm is expected to suffer from nonlinear distortions [55]. A detection gap of 11 mm diameter can be expected. The whole detector is shielded with stainless steel front and back plates to prevent the trap potential from being influenced by the detector potentials and to shield the detector from airborne electromagnetic noise.

In the phase space simulations presented in section 3.2.3, the REMI detectors where simulated perfectly aligned with the trap axis. Alignment deviations from the trap axis would further restrict the trap phase space and reduce the acceptance. In order to optimize this alignment, the hexanode detector has been designed with a 2D-translation mount. As shown in figure 3.10, the whole hexanode and MCP assembly which has been presented in figure 3.9, is mounted on a back plate, highlighted in blue. This assembly can be translated relative to the plate in the

[1] In the actual assembly, the distance between MCP and delaylines has been increase from 2.4 mm to 5 mm.

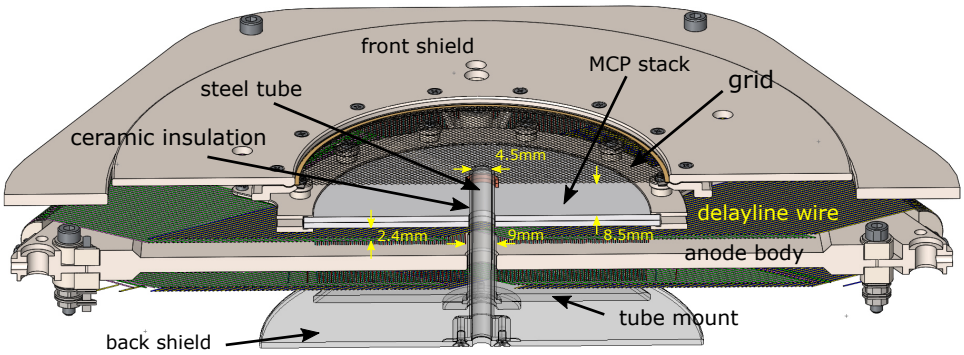

Figure 3.9: Cut through inner elements of hexanode detector. The ion storage path is shielded electrostatically by the detector tube. The whole assembly is shielded by front and back stainless steel plates. Electric potentials can be applied individually to the inner tube, grid, MCP, delaylines and the anode body.

y-direction. The back plate itself is mounted in a DN200 CF flange in which it can be translated in the x-direction. The translation range is ±5 mm. Furthermore, the mounts allow for a rotation about the horizontal and vertical axis by ±1 mm.

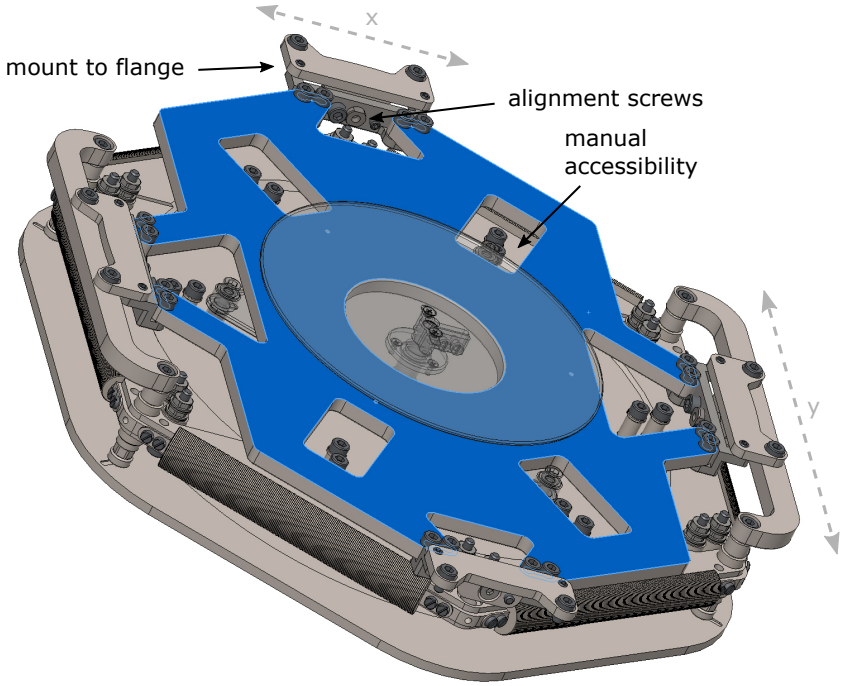

Figure 3.10: Inner detector elements mounted on back plate (blue). The back plate is itself mounted in a CF flange and allows for x,y-translation in the detector plane by ±5 mm as well as for rotation about the horizontal and vertical axis by ±1 mm.

The final design of the complete detector module is presented in figure 3.11. The detector is mounted in a flange with 17 SHV feed-throughs to individually connect the 12 delayline wire ends, the back and front of the MCP, grid, tube and anode body. As shown on the right side, the module is shielded on the back with an additional cover.

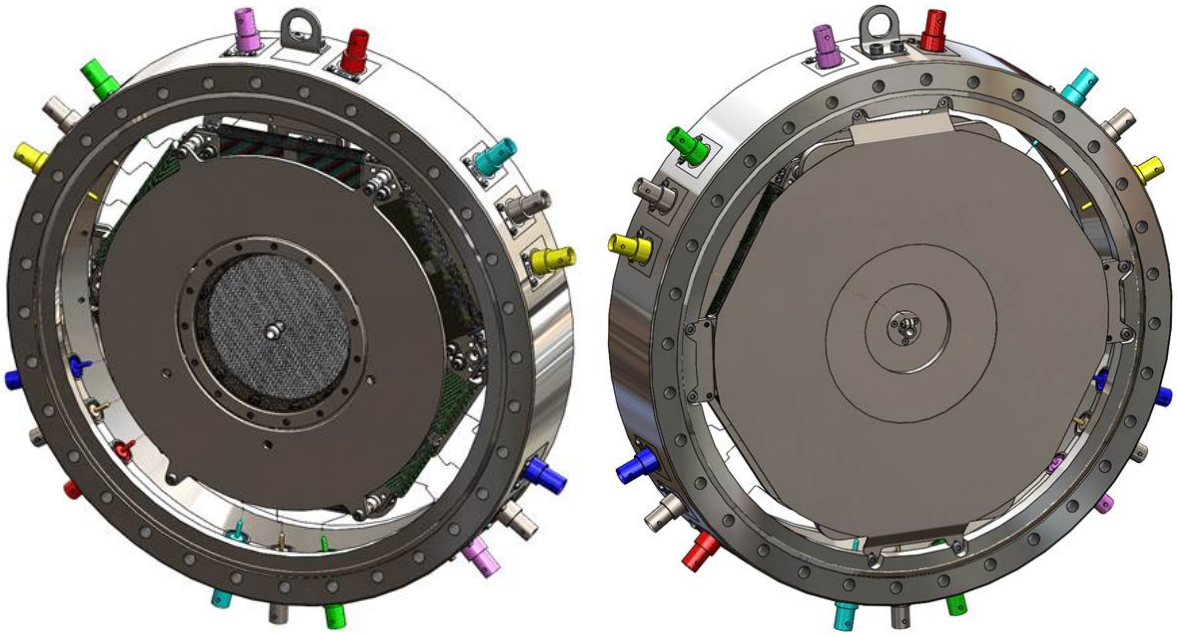

Figure 3.11: Overall view on hexanode REMI detector. (left) front side with grid and MCP. (right) rear side with shielding and electric connection for detector tube.

3.4 Reaction Kinematics and Product Momenta

The TrapREMI setup is equipped with two REMI detectors named ion and electron detector as well as a detector behind the EIBT, named neutral detector. Considering the reaction kinematics of products from a fast ion beam, we estimate the acceptance limits for particle detection on these detectors in section 3.4.1. Thereafter, we describe how reaction momenta can be reconstructed from the particle time-of-flight (tof) and position in section 3.4.2 and estimate how the momentum resolution depends on experimental parameters in section 3.4.3.

3.4.1 TrapREMI Acceptance

Figure 3.12 shows a geometric scheme of particle detection in the TrapREMI. For illustrative purposes, the distances are not to scale. Since the molecules are stored with high initial velocity $\mathbf{v}_0$, ionic products can be detected without applying an extraction field. When a reaction takes place, the products can repel each other and gain reaction velocity $\mathbf{v}_R$. In the laboratory frame, they propagate towards the detector with

$$\mathbf{v} = \mathbf{v}_0 + \mathbf{v}_R. \tag{3.3}$$

The resulting emission angle with respect to the trap axis is $\Theta = \arctan\left(\frac{v_t}{v_z}\right)$ with transversal and longitudinal velocity v_t, v_z. In green, we illustrate the range of emission angles in which ions and neutrals can hit the ion detector. Neutral products can additionally leave the trap through the detector tube and hit the neutral detector. The respective angular range is illustrated in yellow. The acceptance can be characterized by the limit values of these angular ranges. With the geometrical parameters listed in the caption of figure 3.12, we find

- ion detector min. angle: $\Theta^{ion}_{min} = \arctan\left(\frac{R_{dead}}{d_{ion}}\right) \approx 16\,\mathrm{mrad}$
- ion detector max. angle: $\Theta^{ion}_{max} = \arctan\left(\frac{R_{MCP}}{d_{ion}}\right) \approx 117\,\mathrm{mrad}$
- neutral detector max. angle: $\Theta^{neutr}_{max} = \arctan\left(\frac{R_{tube}}{40\,\mathrm{cm}}\right) \approx 5.6\,\mathrm{mrad}$

To illustrate the limits imposed by this geometry on detectable reaction momenta and energies, we employ the case of O_2^+ photodissociation which is presented in chapter 6. An O_2^+ ion with $E_{kin} = 2500\,\mathrm{eV}$ enters the interaction region with $v_0 \approx 1.23 \times 10^5\,\mathrm{m\,s^{-1}}$. We assume for simplicity that the molecules are stored parallel to the trap axis, i.e. that $v_z = v_0$. For the limits of transverse reaction momentum and energy, we find

- min. momentum/energy for ion detector: $p_{R,min} \approx 25\,\mathrm{a.u.}$ / $E_{R,min} \approx 0.290\,\mathrm{eV}$
- max. momentum/energy for ion detector: $p_{R,max} \approx 192\,\mathrm{a.u.}$ / $E_{R,max} \approx 17\,\mathrm{eV}$

- max. momentum/energy for neutral detector: $p_{R,max} \approx 9\,\text{a.u.}$ / $E_{R,max} \approx 0.040\,\text{eV}$

This example shows, that due to the ion storage at keV energies, the ion detector is best suited to detect products which gain high reaction momentum. These limits can be shifted by changing the storage energy or employing the REMI electric field as described section 6.3.1 and figure 6.10. The minimal required reaction momentum is proportional to the square root of the storage energy $p_{R,min} \propto \sqrt{E_{kin}}$.

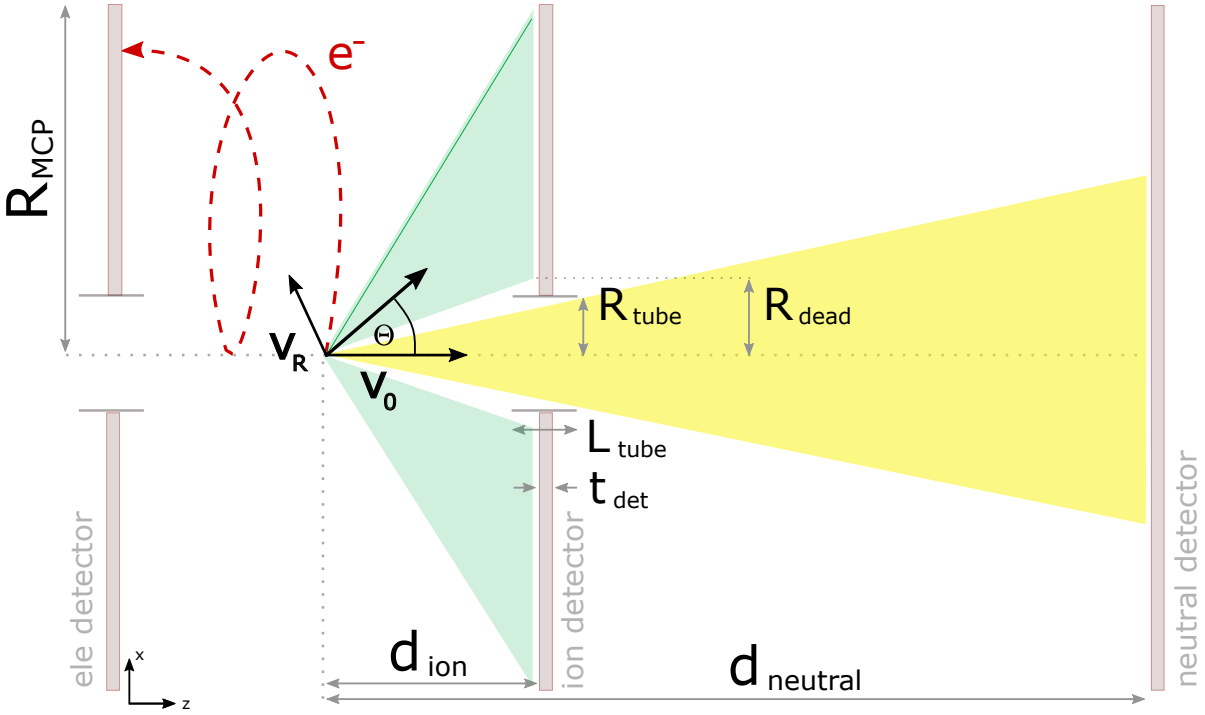

Figure 3.12: Kinematical scheme of detector acceptance: The product is emitted from the reaction with $v_0 + v_R$ under an angle Θ to the REMI axis. (green) angular range for which an ion or a neutral is detected on the ion detector. (yellow) angular range for which a neutral is detected on the neutral detector. (red dashed line) cyclotron trajectory of an emitted electron. (geometrical parameters) detector distances $d_{ion} = 34\,\text{cm}$, $d_{neutral} = 151\,\text{cm}$, tube length $L_{tube} = 8\,\text{cm}$, tube radius $R_{tube} = 0.225\,\text{cm}$, detector thickness $t_{det} = 4\,\text{cm}$, MCP radius $R_{MCP} = 4\,\text{cm}$, MCP dead radius $R_{dead} = 0.55\,\text{cm}$.

Electrons on the other hand, retain only a small fraction of the initial target momentum due to their small mass. This contribution is neglected in the following. As indicated by the red dashed line in figure 3.12, electrons are extracted from the interaction region by the REMI electric and magnetic field on a spiral trajectory. The cyclotron radius can be derived from centrifugal and Lorentz-force to $R_c = \frac{p_t}{eB_z}$, with the electron's transverse momentum p_t and the magnetic flux density along the spectrometer axis B_z. During the cyclotron oscillation, the largest distance of the electron to the spectrometer axis is $2R_c$. For the electron to be detected, this distance has to be

larger than the detector dead radius and smaller than the total MCP radius $R_{dead} < 2R_c < R_{MCP}$. The limits of transverse reaction momentum and energy can be expressed as

$$\begin{aligned} eB_z\frac{R_{dead}}{2} < p_t^{ele} < eB_z\frac{R_{MCP}}{2} \\ e^2B_z^2\frac{R_{dead}^2}{8m_e} < E_t^{ele} < e^2B_z^2\frac{R_{MCP}^2}{8m_e}. \end{aligned} \tag{3.4}$$

By varying the magnetic field, these limits can be shifted according to the actual experiment. For example with $B_z = 1\,\mathrm{G}$, electrons with transverse energy between 3.5 meV and 350 meV can be detected. For $B_z = 10\,\mathrm{G}$, this window is shifted to 350 meV and 35 eV.

3.4.2 Momentum Reconstruction and Sensitivity

A major feature of REMI experiments is to perform kinematically complete experiments. That is, to determine the full 3D - momentum vectors of all reaction products. For n products, there are 3n momentum components which are coupled by 4 equations: momentum conservation in each dimension as well as energy conservation. If the initial target state is known, measuring 3n-4 momentum components is sufficient to obtain kinematically complete information. O_2^+ for example, can dissociate in only two reaction products (if not further ionized). Detecting one of them yields kinematically complete information. However, there are uncertainties in the target preparation: Molecules are stored with a certain momentum distribution and the interaction region is of finite size. Detecting both products yields information on these initial uncertainties. For this, coincidence detection is necessary. That is, detecting multiple reaction products which originate from the same molecule and reaction in a single shot. In this section, we first discuss how particle momenta can be reconstructed from the measurement. Since within this thesis no experiment with electrons as reaction product has been performed, we skip the description of electron momentum reconstruction. A detailed discussion is provided in [10]. We outline basic differences to conventional REMI experiments and estimate the influence of experimental parameters on the measurement sensitivity. Finally, we estimate upper limits for the measurement uncertainties in the case of the O_2^+ photodissociation experiment presented in chapter 6.

In the REMI spectrometer, the Lorentz-force acts on the ionic products. The magnetic field effect can be neglected because of the high product mass and the low magnetic REMI field [57] (p. 57-59). The electric force acts only along the trap axis z and so the equation of motion reduces to

$$\begin{bmatrix} F_x \\ F_y \\ F_z \end{bmatrix} = m \begin{bmatrix} \ddot{x} \\ \ddot{y} \\ \ddot{z} \end{bmatrix} = q \begin{bmatrix} 0 \\ 0 \\ E_z \end{bmatrix} \tag{3.5}$$

Longitudinal momentum. To determine an equation for the longitudinal momentum, we integrate the component along the trap axis with respect to time. Assuming that the reaction takes place at $t = 0$ in the origin $(x_0, y_0, z_0) = 0$, we can write

$$d = \frac{1}{2}\frac{q}{m}\frac{V}{d}t^2 + \dot{z}_0 t. \tag{3.6}$$

Where we used that the products are accelerated by an electric voltage V over a distance d to the detector and are measured after a time of flight t. Thus, the product's total, longitudinal momentum after the reaction can be expressed as

$$p_z = \dot{z}m = \frac{md}{t} - \frac{1}{2}q\frac{V}{d}t \tag{3.7}$$

The first term is the "measured momentum", determined by distance and time-of-flight to the detector. The second corrects for the momentum change induced by the REMI electric field. In the case of an accelerating/decelerating field, V hast to be chosen positively/negatively. In the case of no electric field or neutral particles, the second term vanishes. The quantity of interest is not the total momentum but the momentum gained from the reaction. According to equation (3.3), we can write $\mathbf{p}_R = \mathbf{p} - \mathbf{p}_0$ and

$$p_{R,z} = \frac{md}{t} - \frac{1}{2}q\frac{V}{d}t - p_{0,z} \tag{3.8}$$

Thus, the longitudinal reaction momentum for a certain ion species and fixed REMI fields depends only on the measured time-of-flight. The initial momentum along the trap axis $p_{0,z}$ can be either estimated by the electrostatic potential at which the ions are produced in the source or determined from the center-of-mass of the measured time-of-flight distribution.

Transversal Momentum. For the reconstruction of the transversal momentum components, the time-of-flight as well as the hit positions on the detector are necessary. By integrating the x and y component of equation 3.5, we obtain

$$\begin{bmatrix} p_{R,x} \\ p_{R,y} \end{bmatrix} = \frac{m}{t}\begin{bmatrix} x \\ y \end{bmatrix} - \begin{bmatrix} p_{0,x} \\ p_{0,y} \end{bmatrix} \tag{3.9}$$

Sensitivity of Tof-measurements. It is of interest, how sensitive our measurement is on the different momentum and energy contributions: $\mathbf{p}_0$, E_0 from the stored target and $\mathbf{p}_R$, E_R from the reaction. Further we want to clarify the influence of experimental parameters like time-of-flight distance d, product mass m and target mass M on the resolution. We consider the simple case of longitudinal momentum for a neutral product. Then, from the first-order Taylor expansion of $t = d/v$, we find

$$\begin{aligned}\Delta t(\Delta \mathbf{p}_{R,z}) &= -\frac{m \cdot d}{|\,\mathbf{p}_{R,z} + \frac{m}{M}\mathbf{p}_{0,z}\,|^2}\dot{\Delta}\mathbf{p}_{R,z} \\ \Delta t(\Delta \mathbf{p}_{0,z}) &= -\frac{m}{M}\frac{m \cdot d}{|\,\mathbf{p}_{R,z} + \frac{m}{M}\mathbf{p}_{0,z}\,|^2}\dot{\Delta}\mathbf{p}_{0,z}.\end{aligned} \tag{3.10}$$

This equations show how the momenta are mapped onto a time-of-flight measurement and which parameters influence the mapping. Due to the storage, the target ions enter the reaction with high initial momentum $\mathbf{p}_{0,z}$ compared to targets in conventional REMIs. As result, the momentum distributions are mapped to smaller tof regions which decreases the resolution. The influence of the distribution of initial target momentum depends on the mass ratio of product and parent ion $\frac{m}{M}$. Beneficial for the resolution is the detection of small fragments from heavy parent molecules. Large distances d between interaction region and detector increase the resolution as well. This effect is exploited by the additional neutral detector behind the EIBT which is ≈ 4.5 times as distant as the REMI detectors. Both momentum contributions are mapped differently to the time-of-flight measurement. The uncertainty in initial target momentum gets suppressed by the mass ratio $\frac{m}{M}$. Thus, this setup is best suited for the detection of small fragments from heavy molecules. The total product energy in the laboratory system is

$$E_{kin} = \frac{1}{2}m(\mathbf{v}_0 + \mathbf{v}_R)^2 = E_0 + E_R + 2\sqrt{E_0 E_R} \tag{3.11}$$

with the energy contributions E_0 from the stored target and E_R from the reaction. In the simple case of a neutral product and by approximating $E_{kin} \approx E_{kin,z}$, the time-of-flight can be expressed in terms of this energy as $t = f\frac{\sqrt{m}d}{\sqrt{E_{kin}}}$ in units of eV, u, and cm and with $f = 719.7$ [43] (p. 35). The sensitivity of our time-of-flight measurement on these energy contributions can be expressed as

$$\begin{aligned}\Delta t(\Delta E_0) &\overset{E_0 \gg E_R}{\approx} -\frac{f\sqrt{m}\cdot d}{2\left(E_0 + 2\sqrt{E_0 E_R}\right)^{3/2}}\Delta E_0 \\ \Delta t(\Delta E_R) &\overset{E_0 \gg E_R}{\approx} -\frac{f\sqrt{m}\cdot d\cdot\sqrt{\frac{E_0}{E_R}}}{2\left(E_0 + 2\sqrt{E_0 E_R}\right)^{3/2}}\Delta E_R\end{aligned} \tag{3.12}$$

In good approximation, the relative factor between these contributions is $\sqrt{\frac{E_0}{E_R}}$. Thus, due to the high initial target velocity, the reaction energy is mapped onto a much broader range of flight times. then the initial target energy. In the case of the O_2^+ photodissociation experiment in section 6, this factor is on the order of 10^2.

Obviously, a large time-of-flight distance d is as beneficial for energy as for momentum resolution. The momentum and energy resolutions increase with m and $\sqrt{m}$ respectively. The fact that the

target is stored with high kinetic energy prior to the reaction amplifies the reaction energy. Thus, the time-of-flight measurement is more sensitive to reaction energy compared to the initial target energy by a factor of $\sqrt{\frac{E_0}{E_R}}$.

3.4.3 Momentum Resolution

There are several influences of uncertainty which contribute to the momentum resolution. Given the different REMI geometry and target preparation, these influences differ from conventional REMI experiments. Here we provide basic considerations followed by a specific estimation for the O_2^+ - experiment which is presented in section 6.

Momentum Uncertainties of Target Beam. The target ions are produced at different positions and extraction potentials in the source. This introduces an uncertainty in the initial kinetic energy ΔE_0 and longitudinal momentum $\Delta p_{0,z}$ of the target. The value can be accessed through the Fourier-spectrum of the oscillating target ions. It contains the mean ion revolution frequency $f_{rev} = 29.72\,\text{kHz}$ and the FWHM $\Delta f_{rev} = 0.07\,\text{kHz}$ of the corresponding distribution. From this, we can estimate $\Delta p_{0,z} = p_{0,z}\frac{\Delta f_{rev}}{f_{rev}} \approx 3.9\,\text{a.u.}$ During storage, the target ions can cross the reaction region with different angles to the trap axis. From the REMI geometry, we estimate an upper limit for this angle distribution to be $\pm 6\,\text{mrad}$. We can extract information on the stored ion beam from the phase space projection on the neutral detector as described in section 5.3.3. In the case of O_2^+, the uncertainty in transversal target momentum is estimated to $\Delta p_{0,x}, \Delta p_{0,y} \approx 3.9\,\text{a.u.}$ (see figure 6.7).

Position Uncertainties of Reaction. The reaction takes place in the overlap between target and projectile beam. This introduces a reaction position uncertainty $\Delta x_0, \Delta y_0, \Delta z_0$. When the longitudinal reaction position z_0 varies, the reaction also does not take place at REMI potential $V(0) = 0$ but at

$$V(z_0) = V_0 \frac{d - z_0}{d} \tag{3.13}$$

Where V_0 is the applied potential, d is the distance from REMI center to detector and $d - z_0$ the distance from reaction point to detector. The actual values of these position uncertainties depend strongly on projectile beam and reaction process. In the photodissociation of O_2^+, the reaction position uncertainties $\Delta y_0, \Delta z_0 = 66\mu m$ are defined by the LASER focal width as estimated in section 6.2.3. We also estimate the laser focus to be rather extended. Therefore, the x-direction uncertainty is limited by the ion beam width. An upper limit of $\Delta x_0, \Delta y_0 < 3.6\,\text{mm}$ can be deduduced from the phase space projection on the neutral detector (see figure 6.7).

Uncertainties of Particle Detection. The FlashCam DAQ system enables to perform time-of-flight measurements with an uncertainty of $\Delta t < 0.5ns$. As described in section 2.2.2, an upper limit of $\Delta x, \Delta y < 50\mu m$ can be assumed for the spatial detector resolution.

Overall Uncertainty of Momenta. The overall uncertainty of reaction momenta can be derived from equations 3.8 and 3.9 to

$$\begin{aligned}
\Delta p_{R,x} &= \sqrt{\frac{m^2}{t^2}\Delta x_0^2 + \frac{m^2 x^2}{t^4}\Delta t^2 + \Delta p_{0,x}^2} \\
\Delta p_{R,y} &= \sqrt{\frac{m^2}{t^2}\Delta y_0^2 + \frac{m^2 y^2}{t^4}\Delta t^2 + \Delta p_{0,y}^2} \\
\Delta p_{R,z} &= \sqrt{\left(\frac{m}{t} + \frac{mqV_0}{dp_0}\right)^2 \Delta z_0^2 + \left(\frac{md}{t^2} + \frac{1}{2}q\frac{V_0}{d}\right)^2 \Delta t^2 + \Delta p_{0,z}^2}
\end{aligned} \tag{3.14}$$

With the parameters $m = 16\,\mathrm{u}$, $V_0 = 200\,\mathrm{V}$, $d = 34\,\mathrm{cm}$, $t = 2750\,\mathrm{ns}$, $q = 1$ and $p_0 \approx 1637\,\mathrm{a.u.}$ and the uncertainties estimated above we find for the ion detector

$$\begin{aligned}
\Delta p_{R,x} &< \sqrt{17.5^2 + 0.035^2 + 3.9^2}\,\mathrm{a.u.} \approx 17.9\,\mathrm{a.u.} \\
\Delta p_{R,y} &< \sqrt{0.32^2 + 0.035^2 + 3.9^2}\,\mathrm{a.u.} \approx 3.9\,\mathrm{a.u.} \qquad \text{on ion detector} \\
\Delta p_{R,z} &< \sqrt{0.34^2 + 0.31^2 + 3.9^2}\,\mathrm{a.u.} \approx 4\,\mathrm{a.u.}
\end{aligned} \tag{3.15}$$

These upper limits are governed by the initial momentum spreads $\Delta p_{x,y,z}$ and the position uncertainty along the laser path Δx_0. On the neutral detector, these uncertainties decrease due to a longer distance $d' = 151\,\mathrm{cm}$ and time-of-flight $t' = 12\,300\,\mathrm{ns}$:

$$\begin{aligned}
\Delta p_{R,x} &< \sqrt{3.9^2 + 0.0018^2 + 3.9^2}\,\mathrm{a.u.} \approx 5.5\,\mathrm{a.u.} \\
\Delta p_{R,y} &< \sqrt{0.07^2 + 0.0018^2 + 3.9^2}\,\mathrm{a.u.} \approx 3.9\,\mathrm{a.u.} \qquad \text{on neutral detector} \\
\Delta p_{R,z} &< \sqrt{0.08^2 + 0.07^2 + 3.9^2}\,\mathrm{a.u.} \approx 3.9\,\mathrm{a.u.}
\end{aligned} \tag{3.16}$$

CHAPTER 4

EXPERIMENTAL SETUP

This chapter provides an overview on the experimental setup developed during this thesis and used for the presented experiments. Figure 4.1 presents the final overall TrapREMI setup in the Quantum Dynamics Laboratory at MPIK.

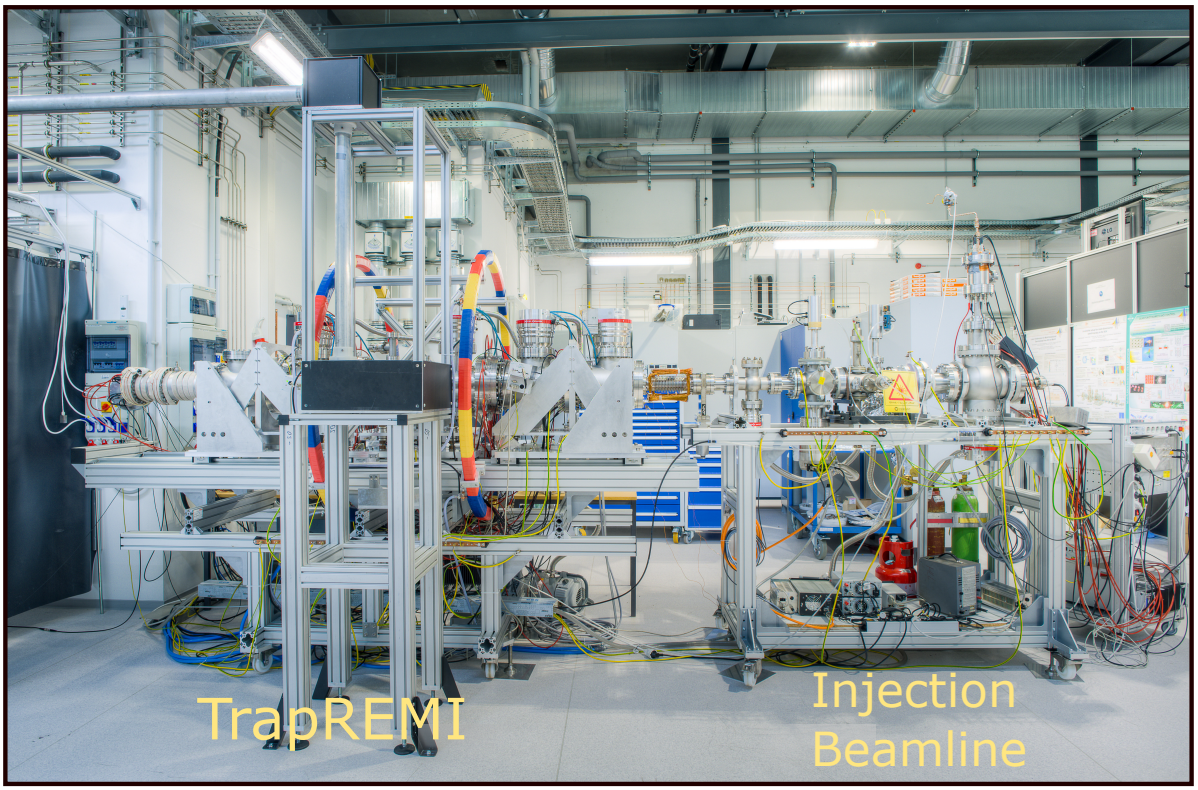

Figure 4.1: Full setup as developed in this PhD thesis.

4.1 Injection Beamline

The injection beamline is presented in figure 4.2. Ions are guided from the source to the TrapREMI on a path indicated by the green, dashed line. The ion source is mounted in a DN100 CF chamber. Both sources used in this setup, electron impact ion source and $^{133}Cs^{+}$-aluminosilicate ion source (see section 5.1), are compatible with this chamber and can be conveniently interchanged. The ion source optics, an electrode assembly described in section 5.1.3, is used to extract the ions from the source and focus and steer them into the 90°-deflector. A Behlke HTS 121 HV-switch is used to pulse the electric potential on one ion source optics electrode to generate bunches instead of a continuous beam. The bunch generation procedure is described in section 5.1.4. The 90°-deflector is a concentric assembly of two ring segment electrodes which we implemented to clean the beam from a continuous neutral background emitted by the source. Thereafter, an Einzel-lens has been implemented as additional focusing element, followed by an aperture consisting of four independently movable slits for beam control and analysis. The aperture is followed by a Faraday-cup to measure the ion current. The ion source is operated in the 10^{-5} mbar regime. To maintain the large pressure difference between the source region and the TrapREMI, the beamline is equipped with three turbomolecular pumps and divided in two differential pump stages by vacuum apertures. The source stage, i.e. from ion source to the first vacuum aperture, is pumped by a Pfeiffer HighPace 300 and a Leybold TURBOVAC 300i. The second stage, between the two vacuum apertures, is pumped by a Peiffer HighPace 80. A mechanical UHV valve can be used to separate the beamline volume from the TrapREMI volume.

4.2 Electrostatic Ion Beam Trap and Reaction Microscope

Setup Overview. Figure 4.3 presents the TrapREMI setup. When the ions are injected from the beamline on the right, they oscillate in the region illustrated by the green, dashed arrow. The REMI is housed in the central part with ion and electron detector. On the left and the right of these detectors, the trap electrode stacks are located. Each stack is equipped with a pickup electrode. The one which is presented in section 5.2.1 is located on the left of the REMI (figure 4.4, left). The EIBT electrode wiring used in the presented experiments is documented in section 9.4. When ions neutralize in the residual gas, they can leave the trap towards the neutral detector as indicated by the orange, dashed arrow. In front of the neutral detector, we implemented a Faraday-plate to measure the ion current order of magnitude behind the trap (figure 4.4, right). To obtain UHV conditions, we pump the TrapREMI volume with three Pfeiffer HighPace 700 turbomolecular pumps.

Helmholtz Coils. Figure 4.5 shows the full setup from the other side. The magnetic coils are arranged in Helmholtz configuration, i.e. their distance equals the coil radius. They have been constructed by coiling over 100 m of copper tube on a ring of $R = 0.7$ m radius, resulting in $N = 24$ windings. The copper tube has an outer diameter of 8 mm and an inner diameter of 6 mm. The

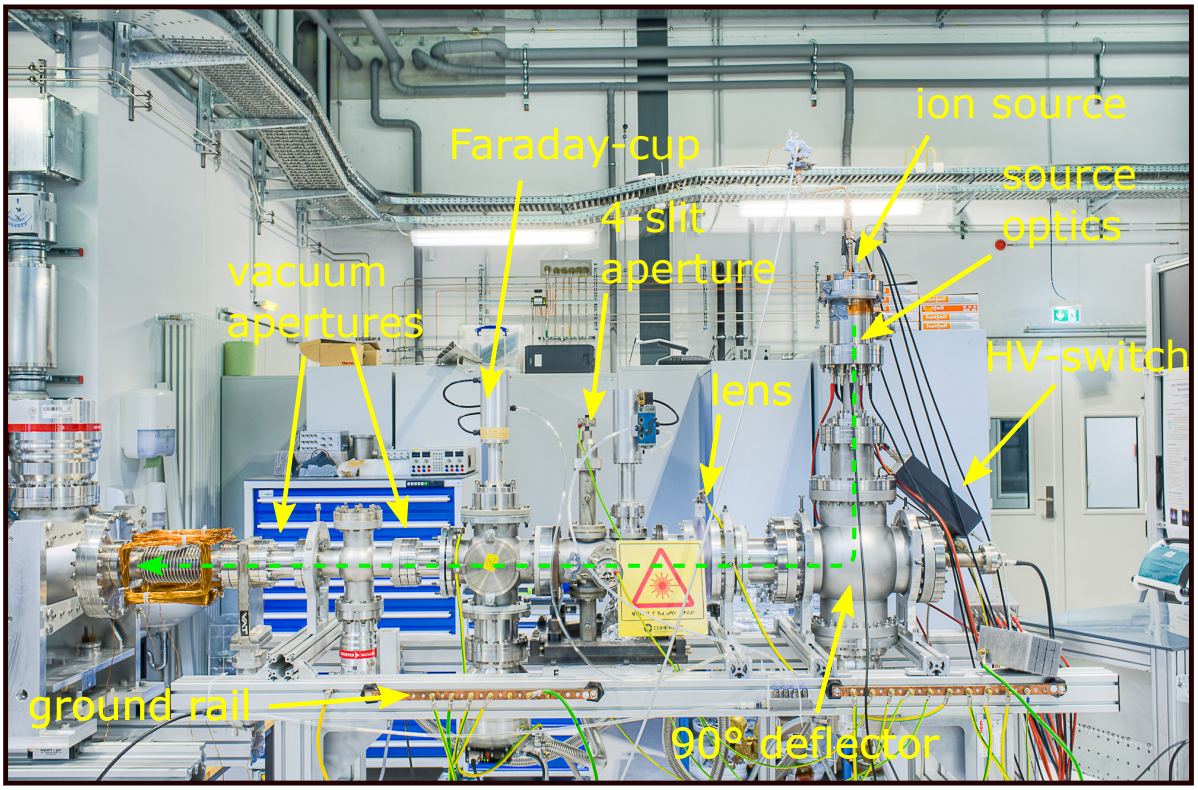

Figure 4.2: Ion injection beamline of the TrapREMI setup

coils have been designed to produce a magnetic flux density up to 20 G in the REMI center. The relation between the applied current and the flux density is $B = \frac{8}{5\sqrt{5}} \frac{\mu_0 N I}{R}$. For 20 G, approx. 65 A have to be applied which heats the copper significantly. Thus, the copper tubes are water-cooled from the inside.

Power supplies are important elements of the setup. For lower voltages, we use ISEG NHS 6205 with V_{max}/I_{max} = 500 V/15 mA. Most electrodes and the REMI detectors have to be supplied with high voltages. Here we apply ISEG NHQ 204M and 208M with 4 kV/1 mA and 8 kV/1 mA respectively. The voltage residual ripple is specified to be below 50 mV peak-to-peak. The power supplies employed at TrapREMI are shown in figure 4.6 (left). The trap mirror electrodes are supplied with high-precision power supplies PNChp10000 by Heinzinger. Since the ions spend most of the time in the mirror regions, particularly close to the turning points, the mirror voltage stability is crucial. The specified residual ripple for this model is 0.001% of the applied voltage.

A **voltage divider** has been developed to distribute the potentials to the mirror electrodes (see figure 4.6, right). The number of electrodes which generate one ion mirror has been between 6 and 10 in our experiments. Supplying each electrode with an individual power supply is not practicable. The voltage divider allows to apply the mirror voltages by means of only a single power supply. It is a chain of twelve 10 kΩ resistors between which the voltage can be picked of, additionally stabilised by capacitors.

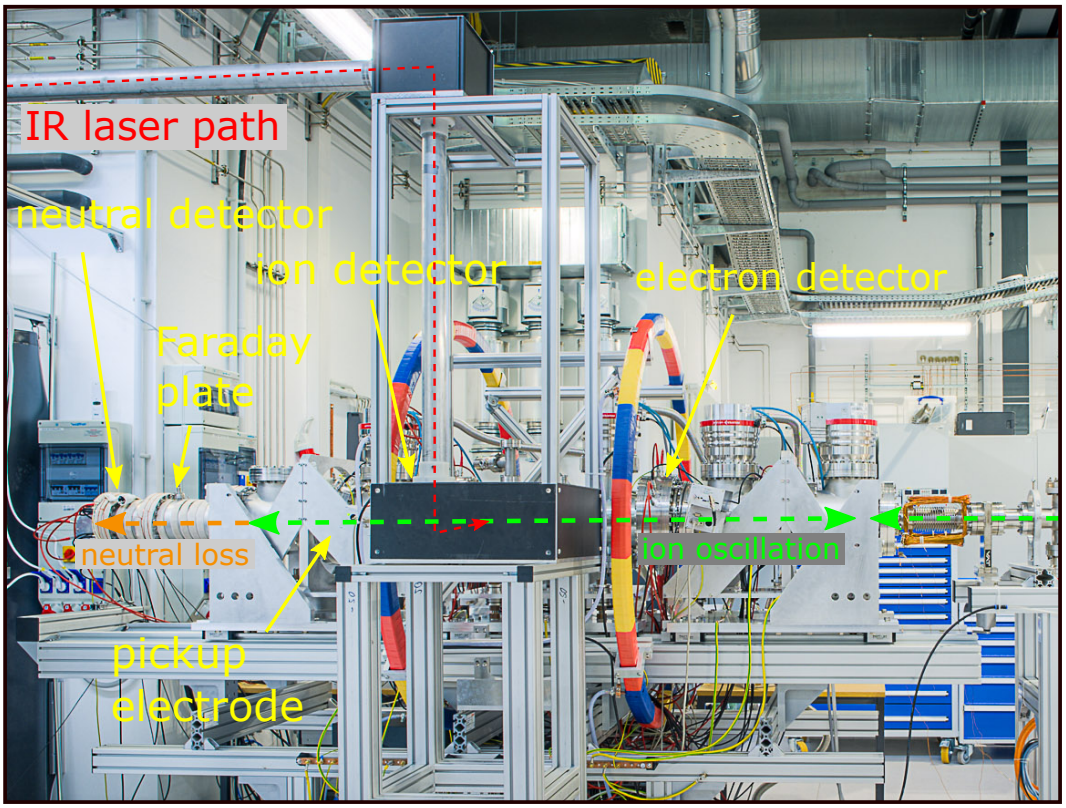

Figure 4.3: TrapREMI setup connected to ion beamline and IR laser

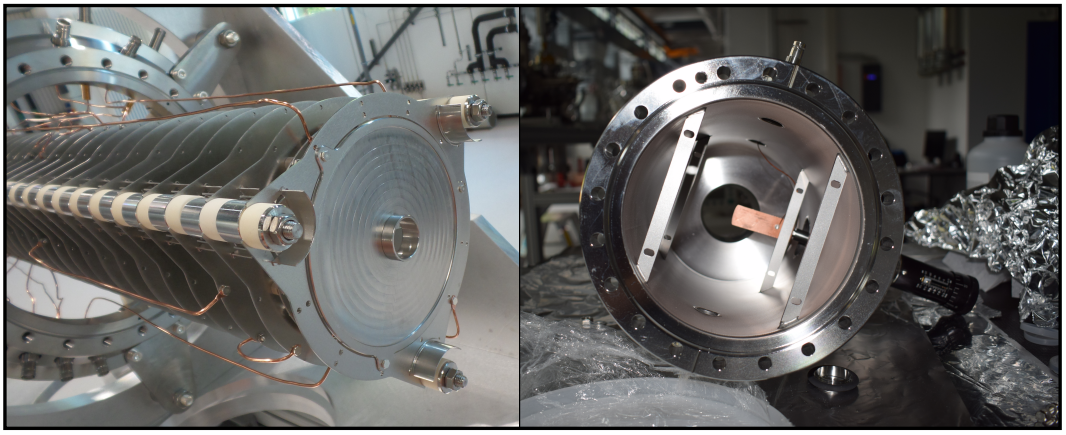

Figure 4.4: (left) pickup electrode on the EIBT electrode stack. (right) Faraday-plate behind trap. A copper plate, mounted on a manipulator.

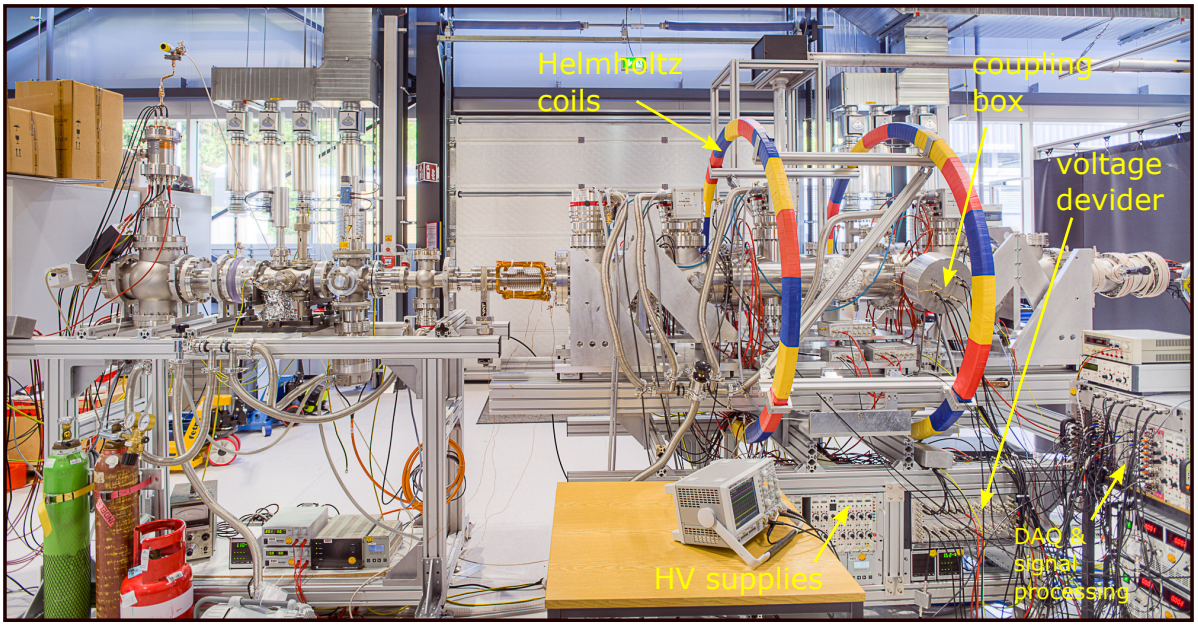

Figure 4.5: TrapREMI setup from the operator's side with experimental accessories and data processing electronics.

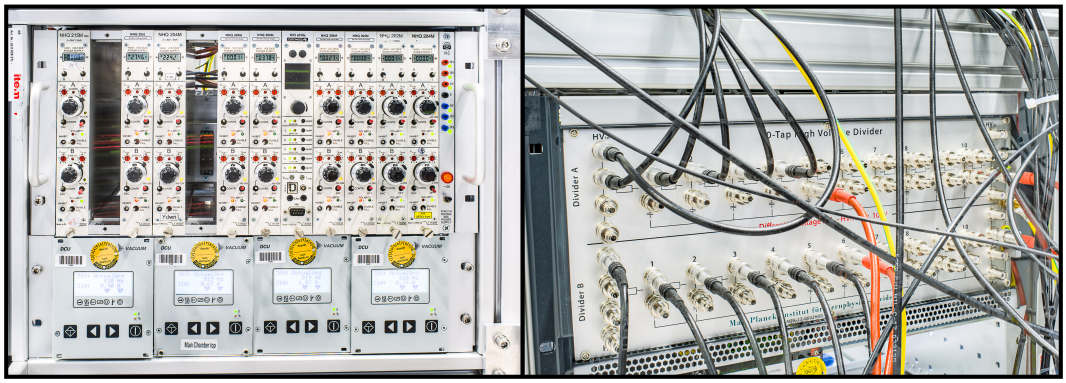

Figure 4.6: (left) Power supplies for trap and REMI voltages. (right) Voltage divider developed to distribute a linear voltage ramp to up to twelve electrodes in each ion mirror.

4.3 Electronics and Data Acquisition

Electronic Data Processing. As described in section 2.2.2, the detectors have to be supplied with high voltages. To distribute these voltages to individual elements of the detector, so-called coupling boxes are employed as shown in figure 4.5. These boxes also couple out the detector signals capacitively. In the case of delayline signals, common-noise rejection is performed, i.e. signals from signal and reference delayline are subtracted from each other via a transformer. Noise contributions which appear on both lines are filtered out. Figure 4.7 illustrates the data processing after the coupling box. The MCP and delayline signals are amplified by an Ortec FTA820A, a fast amplifier with 350 MHz bandwidth, and sent into the FlashCam data acquisition system (DAQ). The MCP signal however is additionally processed by an Ortec 935 constant fraction discriminator (CFD) which outputs a NIM signal. CFDs are usually used to measure the timing of pulses with varying pulse amplitude. Here, we employ only accessory features. The "veto" input of the CFD enables to suppress MCP signals. This is often necessary in the first 200 µs after injection since many ions are lost in the first few turns, hit the detectors and fill the ADC (analogue-to-digital converter) buffers of the DAQ. This leads to an ADC dead time on all channels. Figure 4.8 shows an example of this dead time. For illustration, we additionally plot the ADC acceptance as provided by the DAQ.

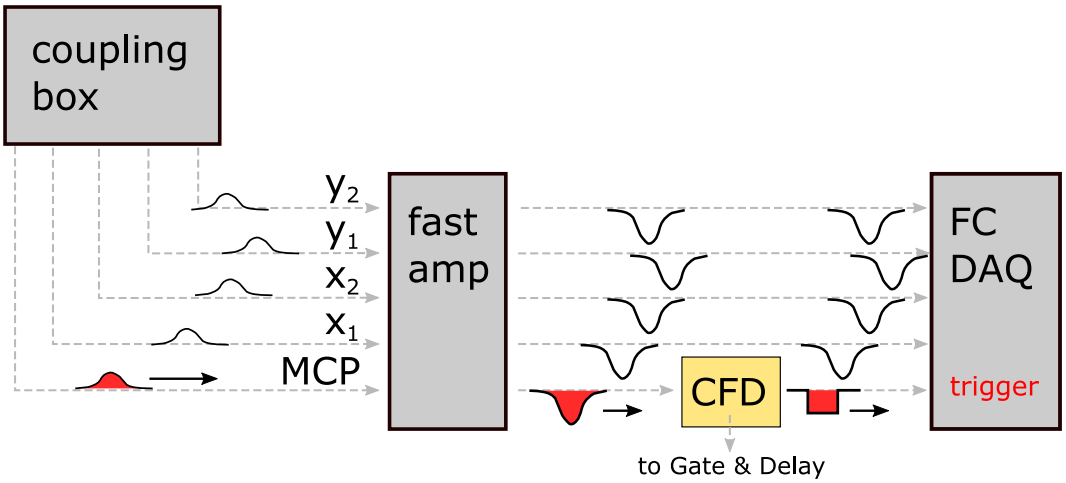

Figure 4.7: Data processing scheme for TrapREMI experiments. For simplicity, we show only one detector. The signal path for the others is analogous. At the CFD, the MCP signal is split and sent to the DAQ as well as to the Gate & Delay unit. The latter path is described in 9.2.

FlashCam Data Aquisition & Go4 The FlashCam data acquisition system has been developed at MPIK for Cherenkov telescope arrays. It features 24 ADC channels which digitize the analogue detector signals with 250 MHz sample rate, i.e. 4 ns sample size, and 12 bit resolution. When the DAQ is triggered by an input signal, it records an event window of adjustable sample length. In this window, the input signals on all 24 channels are recorded. The MCP signal in figure 4.7 is

highlighted in red since we use the MCP signals of the three detectors as trigger signals. Which ADC channel is a trigger channel can be defined by an ADC mask as described in the appendix 9.1. Figure 4.9 exemplarily shows two recorded event windows. On the left, the five digitized neutral detector (quadanode) signals are shown. An event window of 64 samples, i.e. 256 ns has been chosen to ensure that all delayline signals are recorded. Since the samples are stored in the ADC buffers, the event window does not start at the time of the MCP trigger but an adjustable number of samples earlier. The DAQ additionally features various means of data processing like low- and high-pass filters as well as upsampling routines. On the right, we exemplarily show the ion detector signals (hexanode), upsampled by a factor of 4 using multiple moving average routines. A conversion code developed in our group stores this data in ".lma" file format which is compatible with the Go4 framework which we use for online and offline data analysis. The timing of the detector signals is determined in Go4 by CFD or center-of-mass software routines. Reference information and manuals on Go4 are provided on the GSI webpage [58].

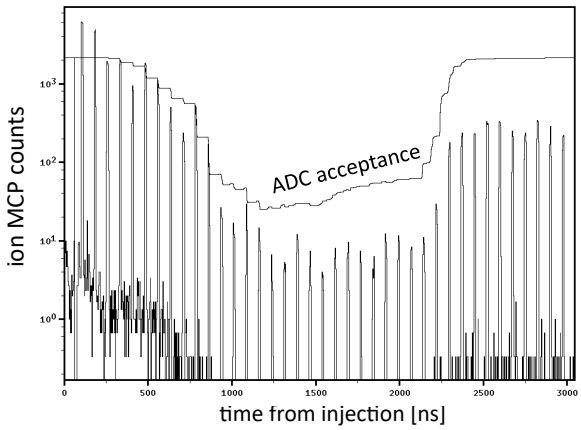

Figure 4.8: MCP counts after injection. The high count rate leads to ADC dead time in the FlashCam DAQ.

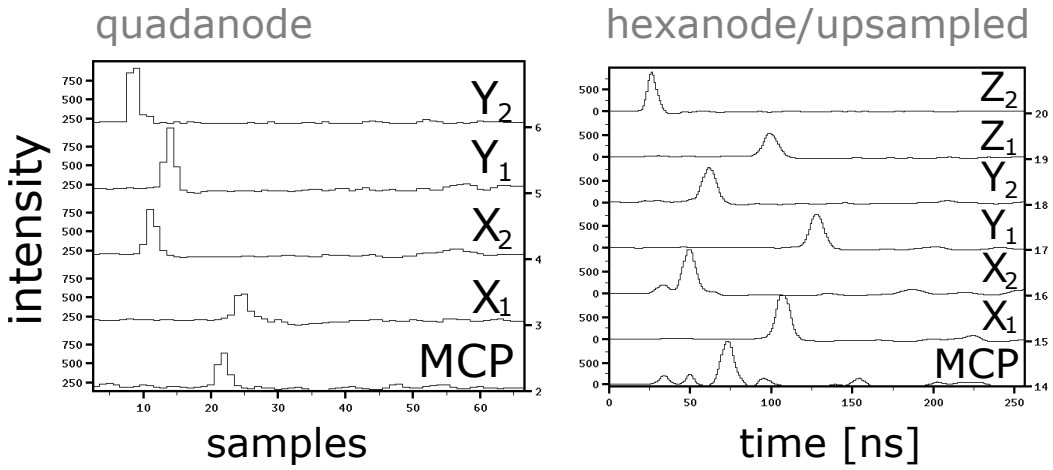

Figure 4.9: (left) Event window with digitized quadanode signals of 64 samples length. (right) Event window with digitized hexanode signals of same length, upsampled by factor 4. The sample axis is replaced by the corresponding time axis.

4.4 Assembly in the Quantum Dynamics Laboratory

In this section, we present impressions of the setup assembly and provide a closer look on some TrapREMI elements. Figure 4.10 shows the new experimental hall at MPIK, shortly after the inauguration in May 2017. We located the TrapREMI outside the new femtosecond-laser laboratory. After constructing the base framework from ITEM components, we implemented the translation and alignment tables on the guiding rails. Thereafter, the EIBT electrode stacks where installed and connected electrically (figure 4.11). Mounted on the alignment tables, these stacks can be aligned relative to each other. When pumped to vacuum, the room atmosphere acts with the corresponding force of approx. 700 kg on the end flanges on both sides of the setup. To ensure a stable alignment, the electrode stacks are mechanically decoupled from this force by stainless steel bellows. As shown in figure 4.12 (left), the electrode's flange is mounted on the alignment table but the outer chamber is mounted on a fixed mount to the translation table and thus the force acts on the guiding rails and item frame. On the right, the decoupling bellow is shown.

Figure 4.13 shows a view into the REMI vacuum chamber. The IR laser path and polarization is indicated by the red, dashed arrow as applied in the experiments presented in chapter 6 and 7. We designed the REMI chamber with multiple flanges to allow flexible access for particle injection or diagnosis devices like mass spectrometer and pressure gauges. In figure 4.14, the ion detector is mounted at the junction between REMI and EIBT. A closer view on the delayline anode is shown in figure 4.15. The delaylines have been coiled on ceramics of different size to place each layer at a different height. Grooves in the ceramics define the distance between signal and reference line to be 0.3 mm and the pitch distance to be 1 mm.

Figure 4.10: Begin of our mechanical assembly in the new Quantum Dynamics Laboratory

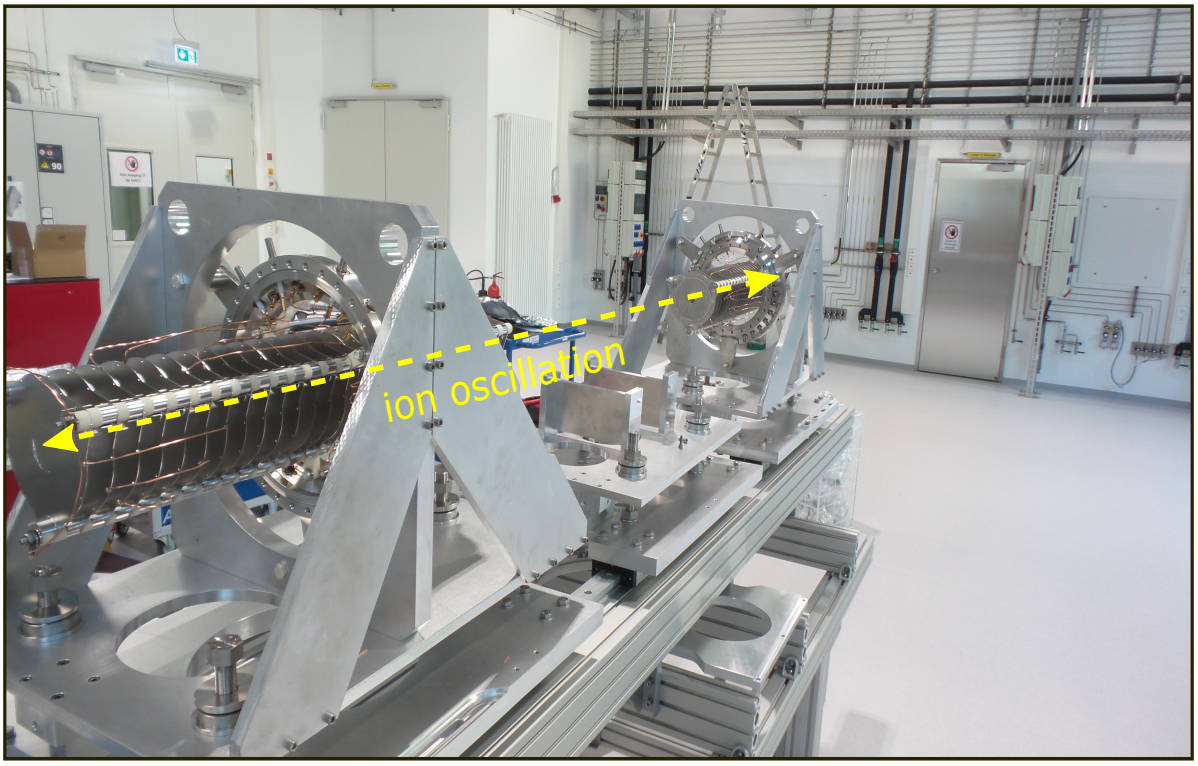

Figure 4.11: EIBT electrode stacks mounted on alignment tables. In yellow, we indicate the trap axis along which the ions will oscillate.

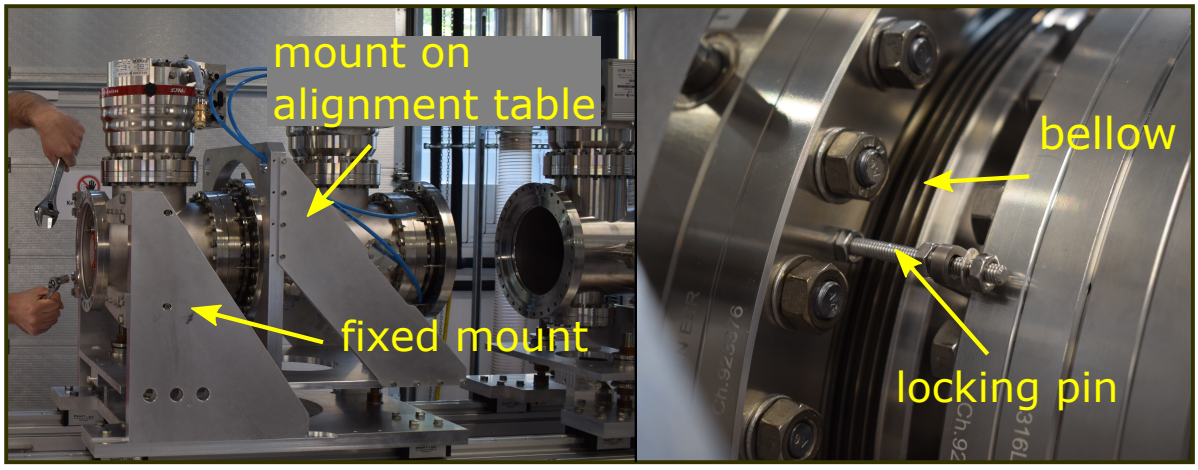

Figure 4.12: (left) The chamber with the trap electrode stack is mounted on an alignment table. The outer chamber is mounted on the translation table. (right) Bellows mechanically decouple the chambers from each other and alignment of the trap electrodes is possible even during operation.

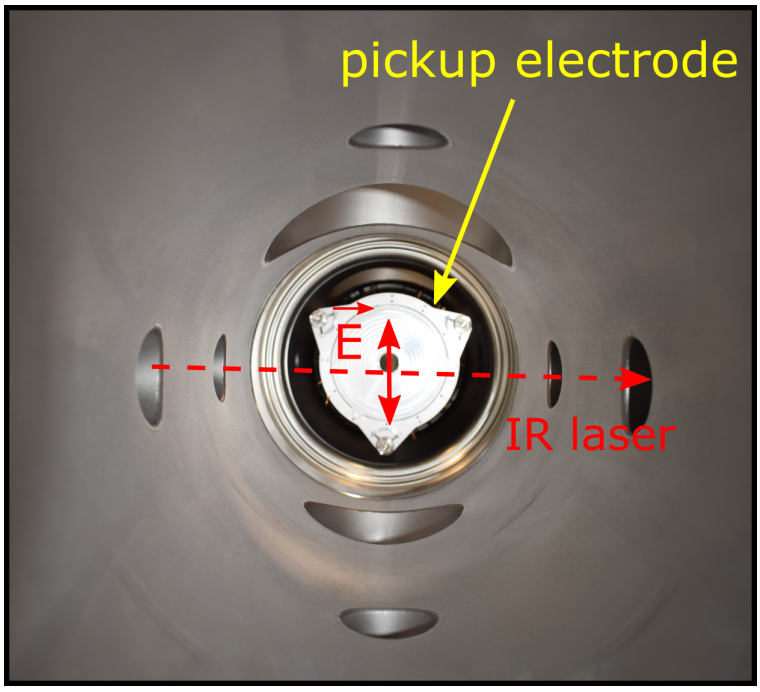

Figure 4.13: Inside view of REMI chamber without REMI spectrometer and detectors installed. The IR laser path and polarization, as used in the experiments presented in this thesis, is indicated in red.

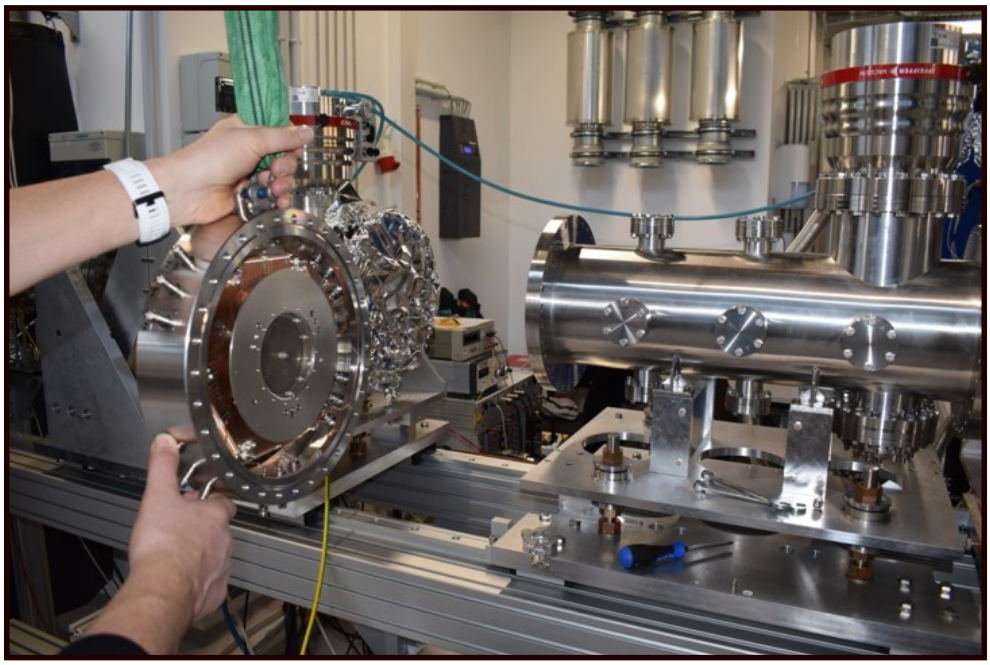

Figure 4.14: Installation of ion detector at the junction between REMI and EIBT.

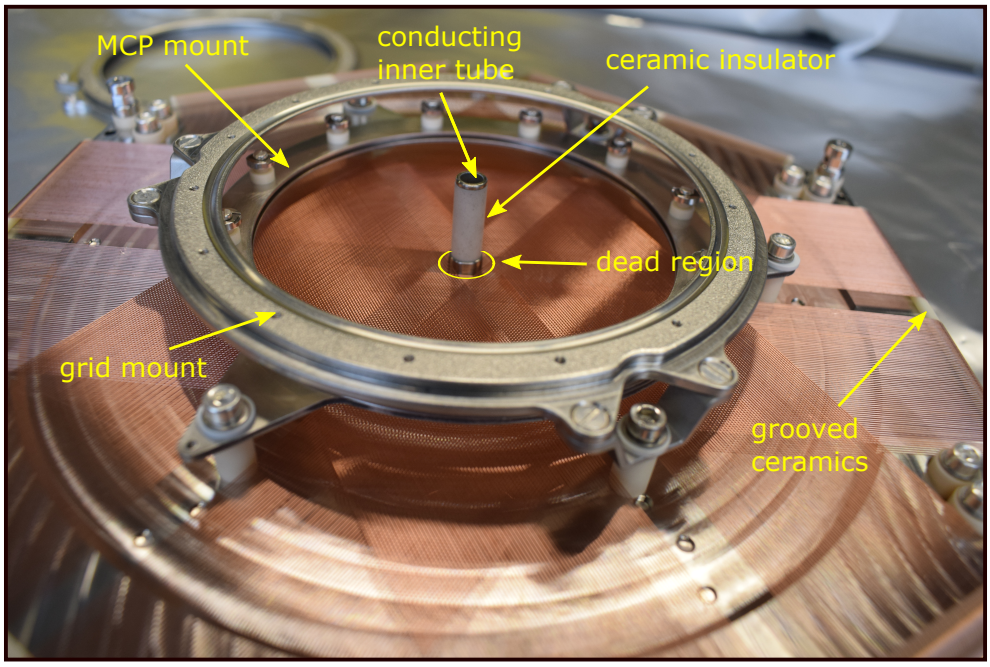

Figure 4.15: Hexanode of ion detector before installing MCP and grid. The delaylines have been coiled on ceramics. Grooves in the ceramics maintain the wire positions. The detector tube shields the ion path way from the high detector potentials. The inner tube potential can be controlled individually.

CHAPTER 5

EIBT CHARACTERIZATION

In this chapter, we outline the ion storage capabilities of the EIBT. First, we introduce the two ion sources employed during this thesis as well as the ion optic means to manipulate and clean the ion beam in section 5.1. Then, in section 5.2, we present how the stored can be monitored by the pickup electrode, the neutral detector as well as by both REMI detectors. In section 5.3, we present the developed scheme of ion injection followed by measurements on ion beam lifetime and phase space projection. Finally, the observed bunch dynamics in dispersive and self-synchronizing mode are discussed.

5.1 Ion Production

In this section, we present the aluminosilicate and electron impact ion source which have been employed for the EIBT characterization in section 5.3 and the photodissociation experiments in chapter 6 respectively. The ion bunch generation scheme presented in section 5.1.4 has been applied throughout this thesis.

5.1.1 $^{133}Cs^+$ - Aluminosilicate Ion Source

To store ions for a first time and characterize the new setup, we favored an ion source which emits high currents, is simple to implement and straightforward to operate. A source which offers these qualities is a solid-state aluminosilicate or "pellet" source. Aluminosilicates are known to be excellent thermionic emitters of alkali metal ions since roughly hundred years [59]. Figure 5.1 (top) shows a cross-sectional scheme together with a photograph of the utilized source model by HeatWave Labs. The source consists of a molybdenum body onto which an extremely porous tungsten disc is welded, serving as emitter matrix. The emitter material, usually an alkali-

aluminomsilicate compound, is fused into the emitter matrix and forms the emission surface at the top. When the source is heated by applying up to 1.8 A to the heater wire, alkali metals in the compound are thermionically emitted to a great extent since they exhibit a relatively low work function. For temperatures between 950 °C and 1100 °C, current densities up to 10 $\mathrm{mA\,cm^{-1}}$ can be reached according to HeatWave Labs [60]. Since the electric potential is the same across the emission surface, a further advantage is the resulting small energy spread among the emitted ions. We chose a $^{133}Cs^{+}$ emitting material since heavy ions are less influenced by the earth magnetic field and thus facilitate a first ion storage. The source mount on a DN40-CF flange has kindly been provided by the group of Sergey Eliseev at MPIK.

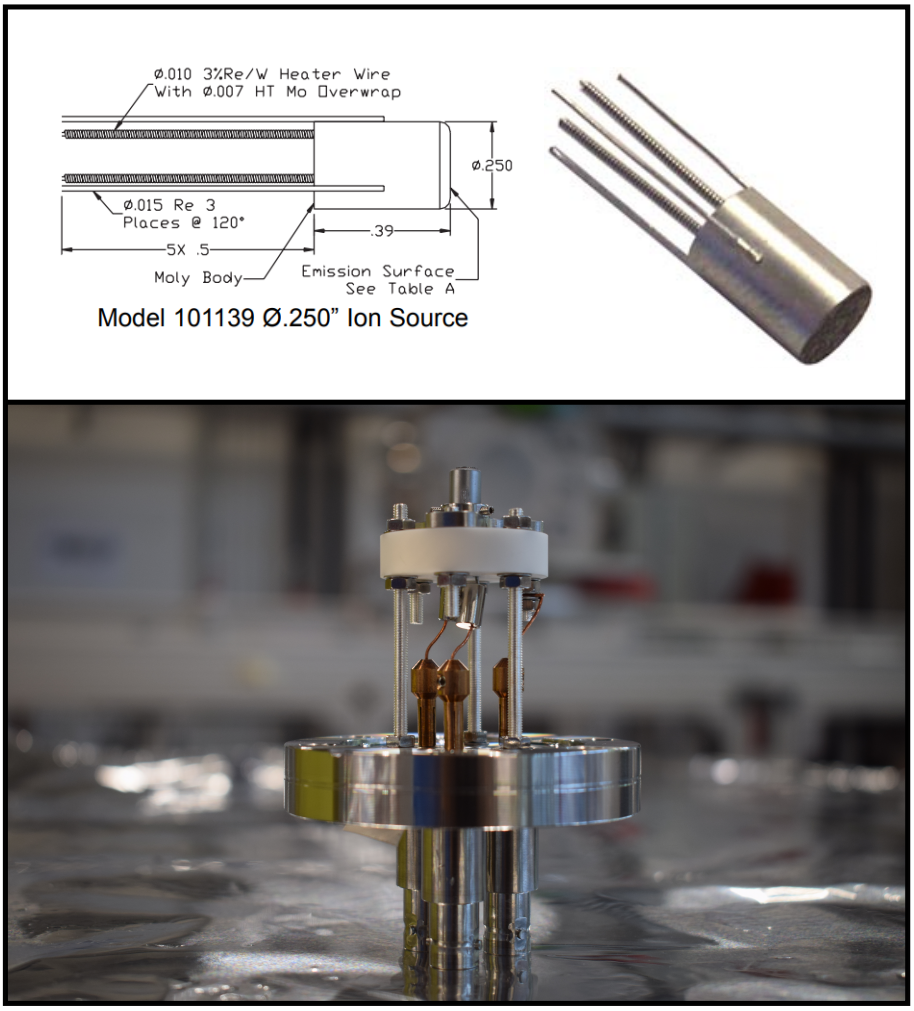

Figure 5.1: (top) Cross-sectional scheme and photograph of $^{133}Cs^{+}$ - pellet ion source. (bottom) Photograph of source, mounted on a DN40-CF flange. Electrically connected are the two heater rods as well as the source body to elevate the source to a desired potential.

5.1.2 Electron Impact Ion Source

The pellet source provided a sound starting point for the characterization of the EIBT but is restricted to $^{133}Cs^{+}$. For the next step, characterizing the REMI and performing first experiments on molecular ions, we required a source which can produce a variety of output species. The MPIK group of Andreas Wolf and Holger Kreckel kindly provided temporarily an electron impact ion source, i.e. a source in which basically every atomic or molecular gas can be ionized by the bombardment of thermionic electrons. This source has been developed by Henrik Pedersen who also made substantial contributions to the understanding of EIBT ion bunch dynamics in the group of Daniel Zajfman [35, 36]. A technical drawing is shown in figure 5.2: While the source is filled with gas, the rhenium filament is heated and emits thermionic electrons. These are accelerated towards the ionization chamber by an adjustable voltage. The electrons reach energies up to $E_{kin} = 110\,\text{eV}$, corresponding to wavelengths down to $\lambda_e = 1.17\,\text{Å}$ which covers the region of characteristic molecular bond lengths and maximizes the energy transfer to the molecule. Examples are the ions produced during this thesis which include oxygen (1.208 Å) [61], ethane (1.09 Å – 3.08 Å) [62] as well as all carbon-nitrogen bonds [63].

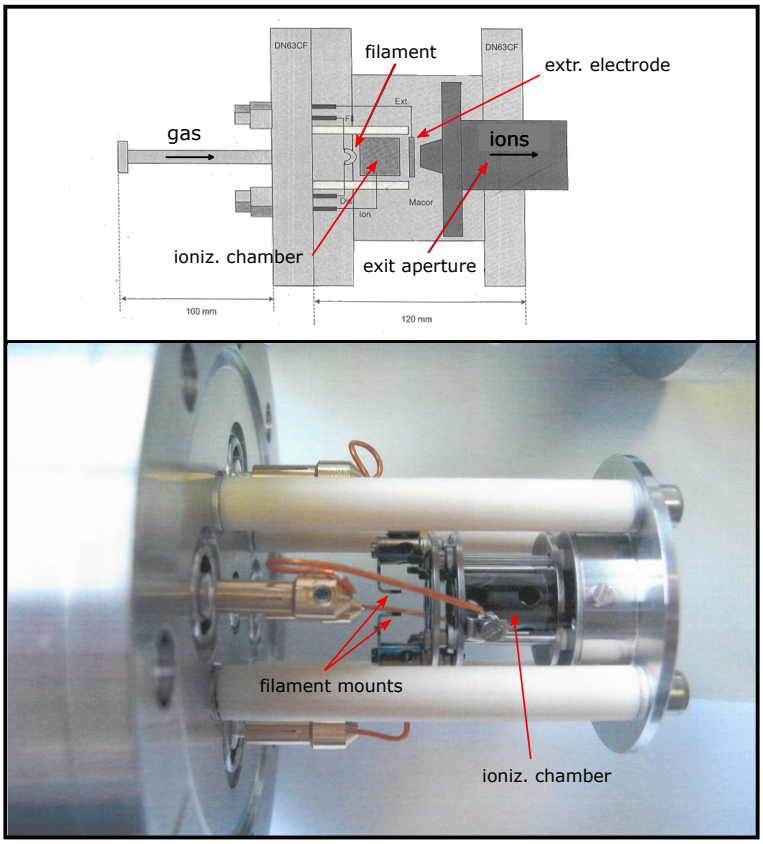

Figure 5.2: (top) Scheme of electron impact ion source and functional elements. (bottom) Photograph of the actual source.

To produce energetic ions, the inner elements of the source (ionization chamber, filament, extraction electrode) can be elevated to an electric potential of up to 7 keV. Since the exit aperture is grounded, the ions are dragged towards it, exit the source and a continuous beam is emitted. By employing the extraction electrode, the extraction potential surface can be optimized for maximum output current. We produced various ion species, including Ar^+, N_2^+, O_2^+, CO_2^+, CH_4^+, $C_2H_6^+$, $C_3H_8^+$, $C_2H_2^+$, SF_6^+. When ionizing molecules, there are usually a lot of possible fragments. To investigate which species are emitted by the ion source, we performed time-of-flight mass spectrometry. That is, we emitted a short ion pulse of 1 µs length and detected it in approx. 5 m distance on the neutral detector. In figure 5.3, we show the example of ethane. The tof-spectrum on the top is compared to a NIST reference mass spectrum on the bottom which allows to identify the emitted species. In principle, we can perform tof-mass selection by pulsing the entrance mirror of the trap and store only a single species. This would however also mean to store only a very short bunch and thus decrease the count rate in experiments. Ion currents of several hundred nA after the source have been observed for all species. Technical limiting are highly reactive species which damage the rhenium filament and species which contaminate the source by depositing material. Examples of the latter are all hydrocarbons. After a week of CH_4 ionization, the inner source elements where fully carbon coated which electrically connected initially isolated elements. Since disassembling and cleaning is effortful, the operation time with contaminating species should be minimized.

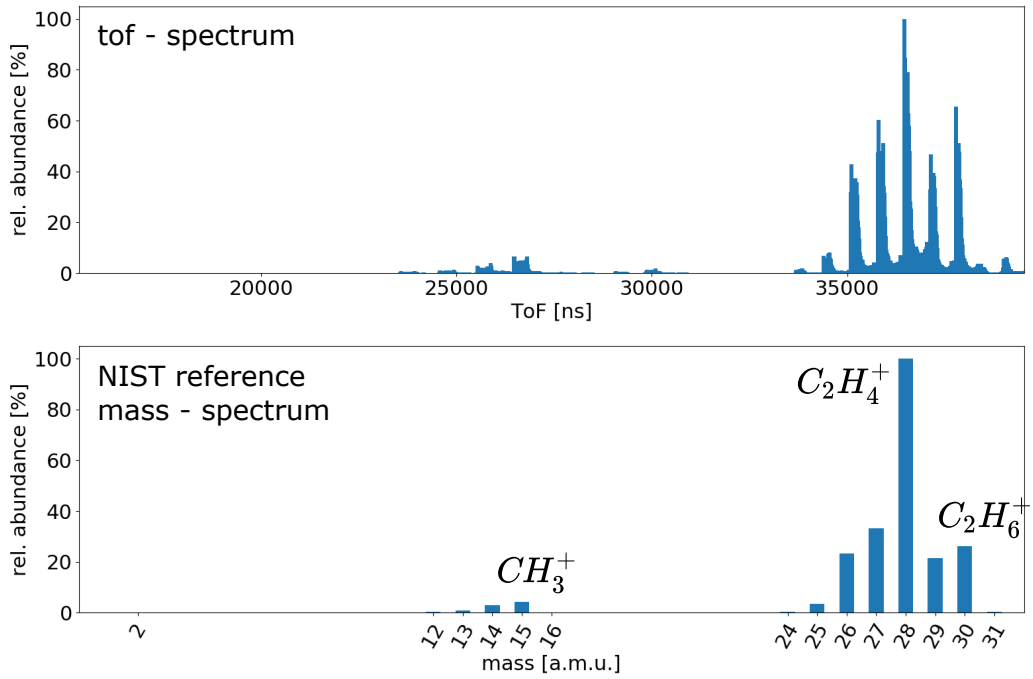

Figure 5.3: (top) tof-spectrum of a 1 µs ion bunch recorded on the neutral detector. (bottom) NIST reference mass spectrum for electron impact ionization of ethane [64].

5.1.3 Ion Optics and Beam Cleaner

In order to efficiently couple an ion beam into the EIBT, we apply several ion optic elements. As shown in figure 4.2, the source is followed by a stack of electrodes with steering and focusing elements as well as a 90°-deflector. A picture of this electrode stack is presented in figure 5.4 (right). The first electrode after the source is labeled extraction electrode because in the case of the $^{133}Cs^{+}$ - source, it controls the extraction potential. When the electron impact source is implemented, which uses an internal extraction electrode, this electrode still can be used to create a focusing potential and thus improve the ion current. Thereafter, three equally-shaped electrodes form an Einzel-lens, followed by a 4-quadrant deflector to manipulate the beam direction.

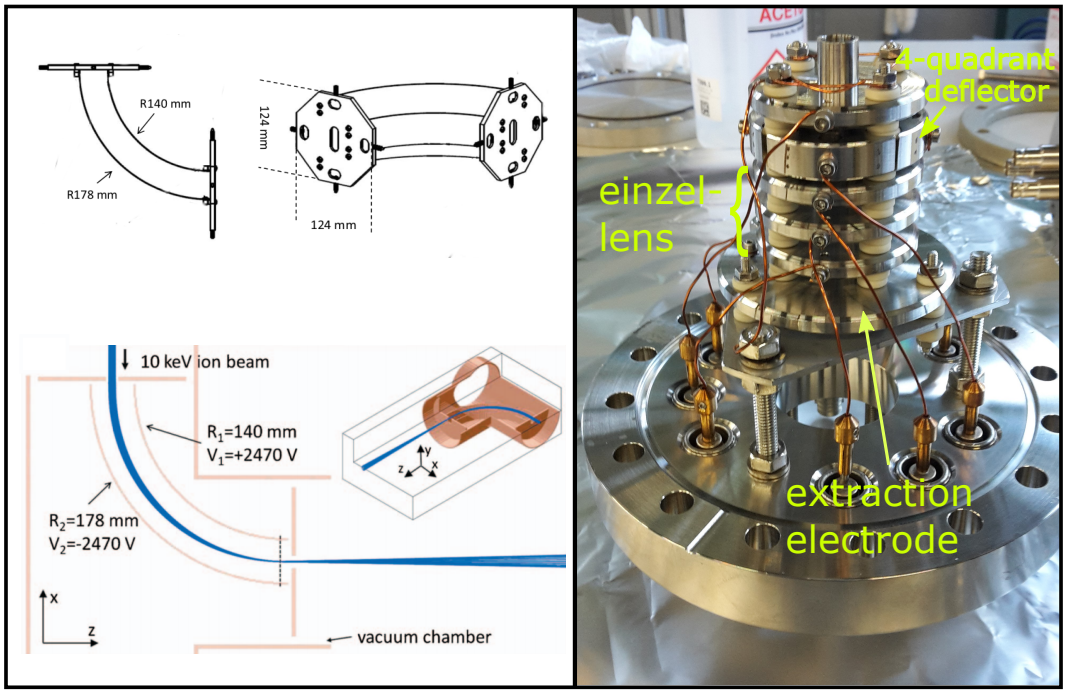

Figure 5.4: (left/top) 3D drawing of 90°-deflector which is used to clean the beam from neutral background. (left/bottom) Exemplary SIMION simulation of beam deflection for 10 keV. Pictures taken from [65]. (right) Ion source optics to further extract, focus and steer the beam into the 90°-deflector. The ion optics have been used for both ion sources.

The electron impact ion source operates at relatively high pressures between 10^{-6} mbar and 10^{-5} mbar. For various species, a maximum current has been achieved for values around 7×10^{-6} mbar. Due to this high pressure, the ion neutralization rate in the first section of the beamline is relatively high and a neutral beam background is observed on the neutral detector behind the EIBT. To clean the beam from this neutral background, we applied a 90°-deflector, developed by Kreckel et al. [65], after the source optics. As shown in figure 5.4 (left/top), it consists of two ring segment electrodes with different radius, arranged concentrically. When applying opposing voltages to these electrodes, ions are transported on an approx. circular trajectory

through the deflector. In In the bottom left of the same figure, exemplary ion optics simulations in SIMION are shown for 10 keV ions. The required voltage is usually approx. a quarter of the ion kinetic energy. The deflector additionally focuses the ion beam which has to be considered when adjusting the focusing elements of the source ion optics.

5.1.4 Ion Bunch Generation

To generate ion bunches, we pulse the electric potential on the source ion optics. For this purpose, we employ a Behlke HTS 121, specified for a max. operation voltage of ±10 kV and a rise time on the order of 100 ns. This model features a low-noise option, also called refresh pulse suppression. A low-noise potential can be crucial for efficient ion storage since the ions perform a high number of revolutions and can accumulate perturbations. A data sheet is provided by Behlke [66]. Figure 5.5 shows the profile of a Cs^+ bunch, emitted with 2500 eV by the source and measured in approx. 5 m distance on the neutral detector. We plot the MCP counts against the ion time-of-flight. This bunch was generated by pulsing the potential on one electrode of the 4-quadrant deflector in the source ion optics. Most of the time, this potential is set to 1000 V and ions are deflected onto the chamber wall. For a short time interval t_{bunch}, the HV-switch pulses the potential to ground and ions are emitted into the TrapREMI. The HV-switch is triggered by a TTL pulse as described in section 5.3.1. The measured temporal bunch length of approx. 150 µs corresponds to the length of the generated TTL pulse. The inset of figure 5.5 shows the spatial bunch profile on the neutral detector.

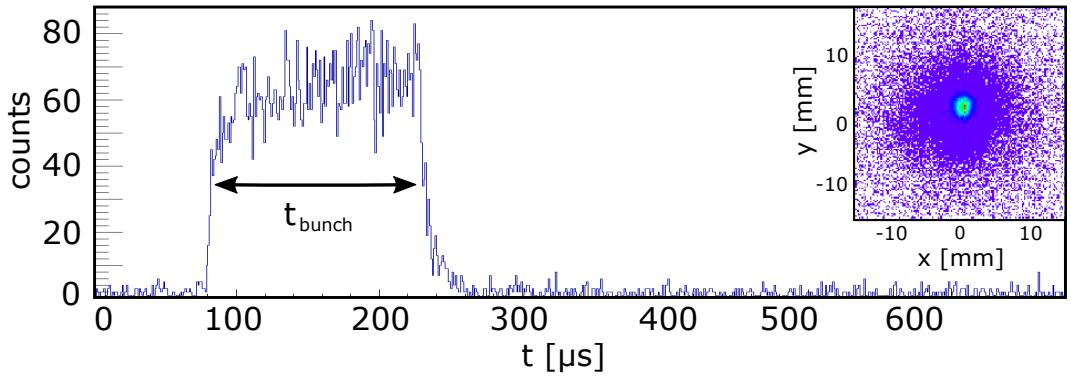

Figure 5.5: Temporal bunch profile. Cs^+ ions have been emitted with 2500 eV and detected on the neutral detector behind the trap. The inset shows the spatial bunch profile on the neutral detector.

5.2 Beam Monitoring Techniques

We designed the EIBT with the same means of beam monitoring as the original version developed by Zajfman et al.: A charge pickup electrode to non-destructively monitor a pulsed ion beam as well as an MCP detector to count neutral particles which leave the trap. Additionally, we observe a signature of the stored beam on the REMI detectors due to elastic scattering in the residual gas.

5.2.1 Charge Pickup Electrode

As shown in figure 4.4, each EIBT electrode stack is equipped with an electrostatic pickup. When an ion bunch passes, a current I_{PU} flows onto the pickup electrode and a mirror charge builds. By measuring this current, the ion bunch can be monitored. In principle, each conductor and thus all electrodes in the EIBT can be seen as a charge pickup. The pickup shown in figure 4.4 is an older version. To optimize the signal strength, we changed the design. The current signal increases with the inverse distance to the monitored charge. We chose a cylinder with a length of $L_{PU} = 18\,\text{mm}$ and a small inner radius of 7 mm as electrode shape. The inner radius is slightly bigger then the inner detector tube radius of 4.5 mm. This is to allow some clearance in the optical alignment of the TrapREMI and thus prevent the pickup electrode from cutting the beam. The signal strength depends inversely on the capacitance of the electrode with respect to ground, i.e. to the mounts and chamber walls. To decrease the capacitance we reduced the mount plate to three rods which hold the electrode in order to decrease the surface area and so the capacitance.

Figure 5.6 shows the current signal of a passing $^{133}Cs^{+}$ ion bunch with central energy of $E_{kin} = 2500\,\text{eV}$. The bunch has been generated by pulsing the ion source deflector with a TTL pulse of $t_{bunch} = 10\,\mu\text{s}$ length. The current has been amplified by a FEMTO DLPCA-200 low-noise current amplifier with 500kHz bandwidth and V/A gain of 10^6. The output voltage has been measured with an HMO3004 Rohde & Schwarz oscilloscope and averaged over 1024 cycles. The current shows the charging (purple) and decharging (red) of a capacitor: When the ion bunch enters the electrode, a high current starts to flow. Then, for approx. $t_{bunch} = 10\,\mu\text{s}$, the electrode cylinder is filled by the ion bunch. The charge inside the cylinder stays constant and the current decreases exponentially. When the bunch leaves the cylinder, the corresponding decharging occurs. The ion number N within the bunch can be obtained by integrating I_{PU} over the charging or decharging period, i.e. the bunch temporal length t_{bunch}:

$$qN(t) = \frac{L_{bunch}}{L_{PU}} \int_0^{t_{bunch}} I_{PU}(t)dt \tag{5.1}$$

With $L_{bunch} \approx 60\,\text{cm}$, the bunch is much longer in space then the pickup electrode. The capacitor charging is induced only due to the bunch fraction which is inside the electrode at one moment

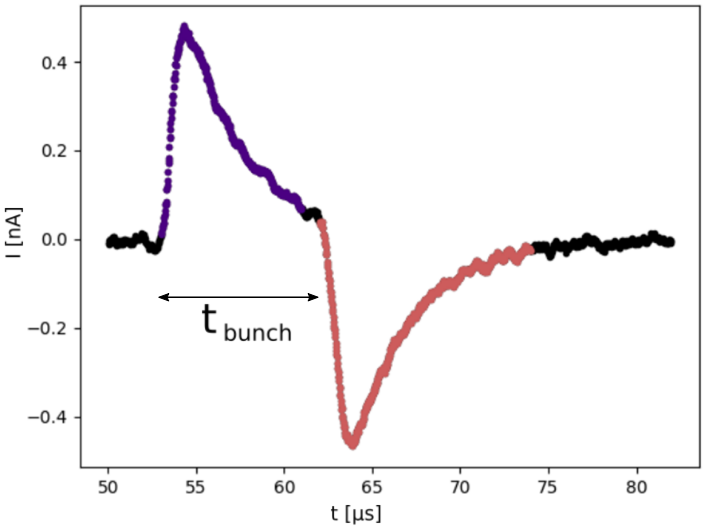

Figure 5.6: Signature of a passing ion bunch: Electric current flows to and from the pickup electrode. The latter charges as a capacitor while it is filled with ions, i.e. for the temporal bunch length t_{bunch}, and decharges when the bunch has passed. The areas under the curve are the charge accumulated on the electrode. From this, the approx. ion count inside the bunch can be extracted.

in time. To obtain the overall ion number, the integral is corrected by the length ratio of pickup electrode and ion bunch $\frac{L_{bunch}}{L_{PU}}$. In the example of the presented $^{133}Cs^{+}$ - bunch in figure 5.6, we obtain a total charge on the electrode of 1.15×10^{-13} C which corresponds to approx. 7.17×10^{5} singly charged ions. This can be compared to the ion current which traverses the EIBT: When not pulsed, a current of approx. 13 nA is measured on the Faraday-plate after the trap. A 10 µs long pulse of this current corresponds to approx. 8.11×10^{5} singly charged ions. There are several uncertainties in this measurement: The ion bunch has an electrostatic influence already when it is close to the pickup but not yet inside which increases the measured ion count. Additionally, the temporal bunch length t_{bunch} is the length to which the source-triggering TTL pulse has been adjusted. Since the HV-switches operate with a finite rise-time on the order of a few hundred ns, the actual bunch length will differ slightly. Furthermore, the Faraday-plate provides only a rough measurement of the ion current since it has no cup-geometry and correction means like secondary-electron suppression. In conclusion, the pickup-electrode is a mean to monitor single or stored ion bunches non-destructively. It can be used to optimize trap parameters and to estimate the order of magnitude of stored ions.

5.2.2 Neutralization Loss

In EIBTs, ion loss due to collisions with residual gas particles is observed [22, 30]. For positive ions, a possible loss mechanism is electron capture, as illustrated in figure 5.7. When neutralized, the ion can leave the trap through the electrostatic mirror and can be detected on the neutral detector. This path is also indicated in the TrapREMI setup overview in figure 4.3. In the case of molecular ions, collision induced dissociations with neutral fragments can contribute to the measured neutral loss. The collision induced neutralization rate is expected to be proportional to the number of stored ions $N(t)$

$$\left(\frac{dN(t)}{dt}\right)_{neutr.} = -\frac{1}{\tau_c}N(t) \tag{5.2}$$

and a corresponding exponential decay of $N(t)$ is observed. The time constant τ_c is interpreted as lifetime of the stored ion beam. For the case of electron capture, the lifetime can be expressed as

$$\tau_c = \frac{1}{<\sigma_c v>\rho} \tag{5.3}$$

with the residual gas density ρ, the ion velocity v, and the electron capture cross-section σ_c. The average $<\sigma_c v>$ is performed over one ion revolution period and accounts for the fact that the ion velocity changes and σ_c can be velocity dependent [22]. The electron capture cross-sections for many ionic species at keV energies are in the same range, see for example [67] and [68].

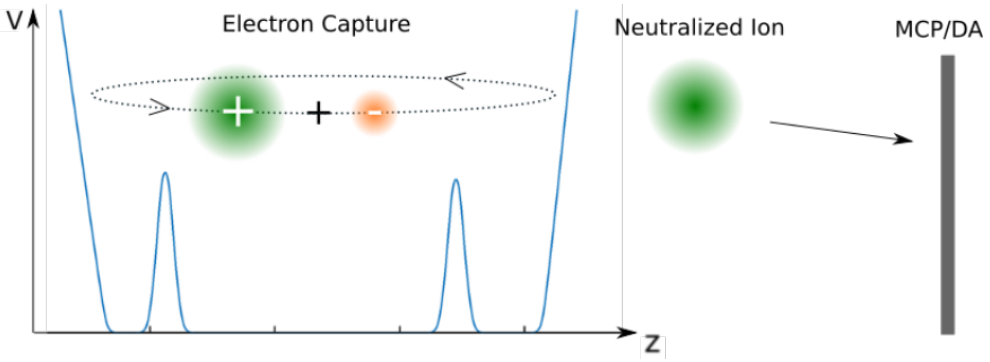

Figure 5.7: Illustration of electron capture in the residual gas. While a cation oscillates in the EIBT potential landscape, it can capture an electron from residual gas particles. It is no longer reflected by the electrostatic mirrors and can leave the trap.

5.2.3 Elastic Scattering to REMI Detectors

Another loss mechanism observed in EIBTs is elastic scattering on residual gas particles [30]. This process alters the angle of individual ions and redistributes them in phase space. Particles on the acceptance limit can be deflected out of the trap. When ions pass through the REMI, they can be scattered onto the detectors. We observe an intense ion storage signature, alternating between the REMI detectors as presented in figure 5.8 with the ion revolution period $T_{rev} \approx 68.87\,\mu s$ and the adjusted bunch length $t_{bunch} \approx 10\,\mu s$. The measurement has been performed at $p = 1 \times 10^{-9}\,mbar$ and the probability of detecting a scattered particle was around 1% for each passage of the bunch. Thus, these events do not hinder the detection of the reaction products by depleting the detector. This probability depends strongly on the actual trap configuration. As can be seen in figure 5.8, the signal intensity is not the same on ion and electron detector. The relative intensities can be varied by shifting the ion beam focus position in the REMI along the axis by changing the EIBT Einzel-lens voltages. Observing the MCP time traces on the oscilloscope while optimizing the trap voltages is a qualitative indication of the focus position.

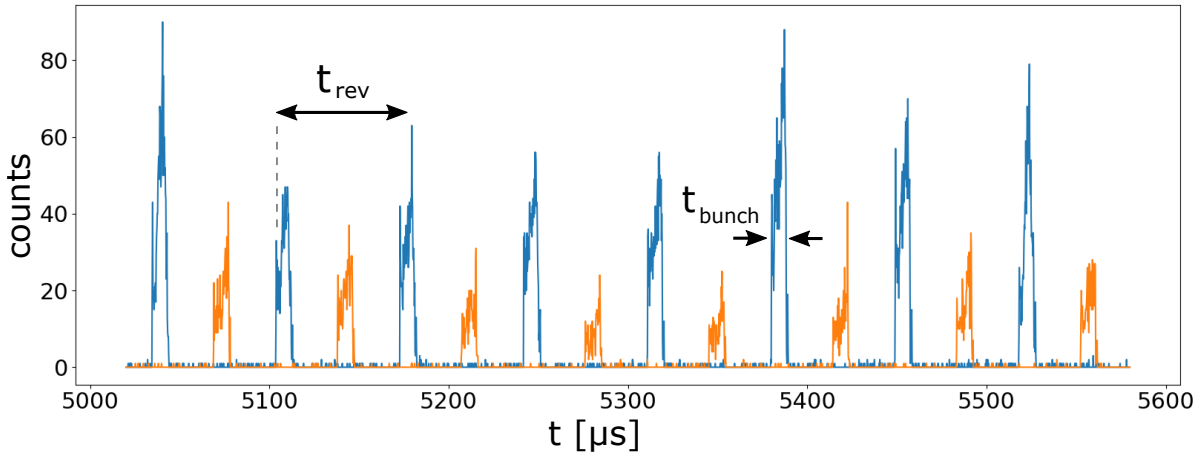

Figure 5.8: Counts on ion MCP and electron MCP respectively. Particles scatter onto the detector when the ion bunch passes. This signal can be used to monitor the stored beam and optimize the trap voltages.

The elastic scattering loss can be described analogous to the neutralization loss with

$$\left(\frac{dN(t)}{dt}\right)_{scatter.} = -\frac{1}{\tau_s}N(t). \tag{5.4}$$

Based on the differential cross-section for Rutherford scattering, the scattering lifetime has been estimated to depend on the storage energy like $\tau_s = \frac{E^{3/2}}{\chi}$ with an empirical constant χ [22].

5.3 Ion Storage and Dynamics

In this section, we present ion storage experiments to outline the trapping capabilities of the TrapREMI setup. First, we describe the general scheme and technical implementation of the injection procedure in section 5.3.1. Then, we present experiments on the ion beam lifetime and phase space projection in sections 5.3.2 and 5.3.3 respectively and finally discuss the observed longitudinal bunch dynamics in section 5.3.4.

5.3.1 Injection Over Barrier

The injection procedure is based on a fast switching of the entrance mirror potential: First, the potential is low and ions can enter the trap. When they pass the trap center, the potential is raised and the ions are trapped. The switching of the entrance mirror potential has to be performed on a timescale faster than the ion revolution period. For kinetic energies up to 10 keV, this period is above 1 µs. We applied an HV-switch (Behlke HTS 121) with a rise-time on the order of 100 ns. In the original EIBT as well as in the CTF at MPIK, all electrodes which generate the entrance mirror potential have been pulsed to ground to allow for ion injection [20], [22]. In the TrapREMI setup, a larger number of electrodes is used to apply the mirror potential. Lowering the potential on all mirror electrodes simultaneously requires an individual HV-switch and HV-source for each electrode. This would increase cost as well as electric switching noise. A straight-forward solution is to lower only the mirror peak, i.e. the potential on the outermost mirror electrode. Figure 5.9 illustrates the two operational trap modes: injection and storage. In the injection mode, the entrance mirror potential V_{mirror} is lowered below the ion kinetic energy E_{kin} and the ions can overcome the barrier. As described in section 3.2.3, the ion beam phase space has to match the trap phase space for efficient ion storage. The ion beam phase space is manipulated by each ion optics element. Since during the injection, the entrance mirror potential is close to E_{kin}, it constitutes an ion lens with very short focal length and strongly manipulates the beam phase space such that no ion storage is possible.

Phase space matching can be achieved by employing another lens in front of the trap. In figure 5.9, it is labeled injection lens. To investigate how the this lens has to be adjusted to efficiently inject ions over the entrance barrier, we performed the SIMION simulation presented in figure 5.10: We generated ions with a Gaussian position, angle and energy distribution and injected them over the barrier. The red data points show the injection efficiency, i.e. the percentage of injected ions which was stored on stable trajectories, depending on the focus position of the injection lens. The magnitude of efficiency depends on the distributions the ions are simulated with. However, we always obtain that focusing the ions in the vicinity of the entrance barrier leads to the most efficient injection. By applying this procedure in the experiment, ion storage was achieved. Without the injection lens, no ion storage was observable. This is an example where the flexible EIBT design has proven valuable: It was not necessary to fabricate an additional ion

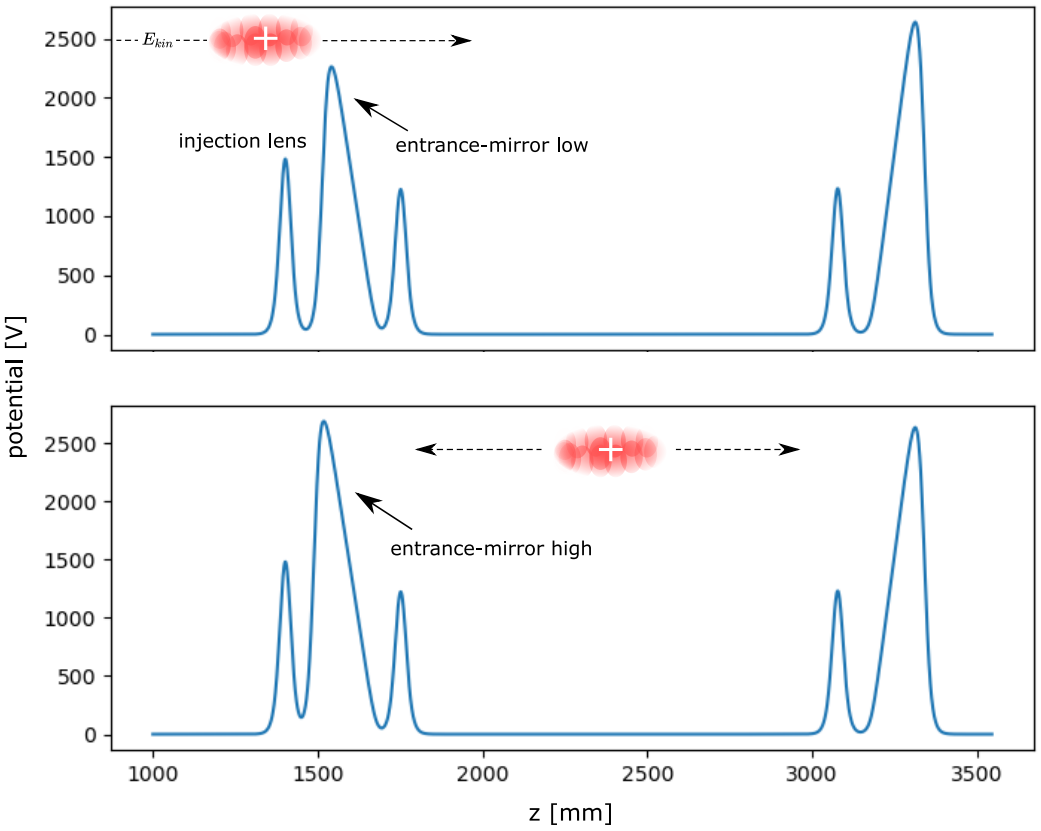

Figure 5.9: (top) Injection mode: The entrance mirror potential is lowered below the ion kinetic energy so that the ions can pass. This potential constitutes a strong ion lens which prohibits storage. In order to compensate this effect, we apply an injection lens in front of the EIBT. When focusing in the vicinity of the entrance mirror, ions can be stored efficiently. (bottom) Storage mode: When the ion bunch reaches the trap center, the entrance mirror potential is raised again.

lens for the beamline. We reduced the number of electrodes which form the trap potential, i.e. we reduced the trap length, and used one of the electrodes which has become available to form the injection lens. To adjust the latter in practice, we numerically investigated the focal length depending on the applied voltage in [69].

The injection procedure has been implemented as illustrated in figure 5.11. A LabVIEW program controls a counter/timer module (National Instruments PCIe-6612) to generate four TTL trigger pulses of adjustable length. One trigger (black) provides a global time reference t_0 for the data acquisition. At t_0, the ion injection starts and all subsequent event timings are recorded with respect to this reference. The time reference is defined by the rising edge, the pulse length has no effect. The next two TTL trigger control the source and trap HV-switches. The trigger states high/low correspond to closed/open source and trap potentials respectively. The source is opened at t_0 for a time t_{bunch} (blue trigger), defining the temporal length of the emitted bunch.

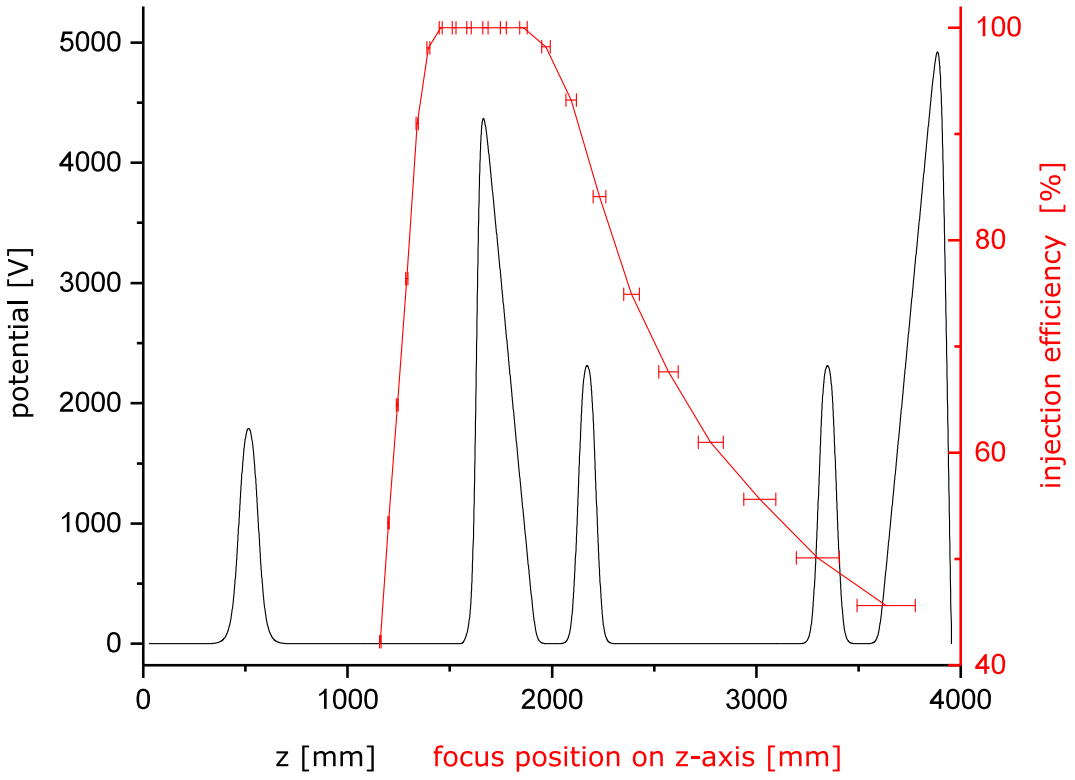

Figure 5.10: (black) Simulation of the potential landscape on axis of the EIBT. In front of the entrance mirror, an additional ion lens focuses the ion beam. (red) Simulated storage efficiency depending on the focus position of this lens. The beam can be most efficiently coupled into the EIBT when it is focused in the vicinity of the entrance mirror. Graph adapted from [69].

The trap is opened at t_0 as well and closed at a time t_t (green trigger). This time has to be chosen such that the trap closes when the bunch is inside. Preferably, the bunch is on the other side of the trap to be not effected by the closing of the trap entrance mirror. In our setup, the ion revolution period has proven to be a good starting value for t_t. The orange trigger is sent to the CFD veto input and suppresses all MCP signals for a time t_{dead}. This is necessary to prevent the ADC buffer dead time due to extremely high count rates in the first 200 µs as discussed in section 4.3. After an adjustable storage cycle t_{store}, the trigger sequence is repeated and another ion bunch is injected. Before the cycle ends, the trap is opened again by the green trigger to clear the trap and record background.

Figure 5.12 shows a generic signature of ion injection. At t=0, we emitted $^{133}Cs^+$ ions from the source with $E_{kin} = 2500\,\text{eV}$ and $t_{bunch} = 2\,\mu\text{s}$ and monitored the storage with the electron detector. We observe intense HV-switching noise at $t = 0$ and $t = 55\,\mu\text{s}$, corresponding to the adjusted trap opening time t_t. Thereafter, the dominating signal is the ion bunch revolution with a period of $t_{rev} \approx 68.7\,\mu\text{s}$ and bunch length of $t_{bunch} \approx 2\,\mu\text{s}$. Additional minor signals are observed which decay a few ms later and are not discussed in detail. Since no mass selection is performed in the ion beam line, the initial ion bunch is expected to be contaminated with other species.

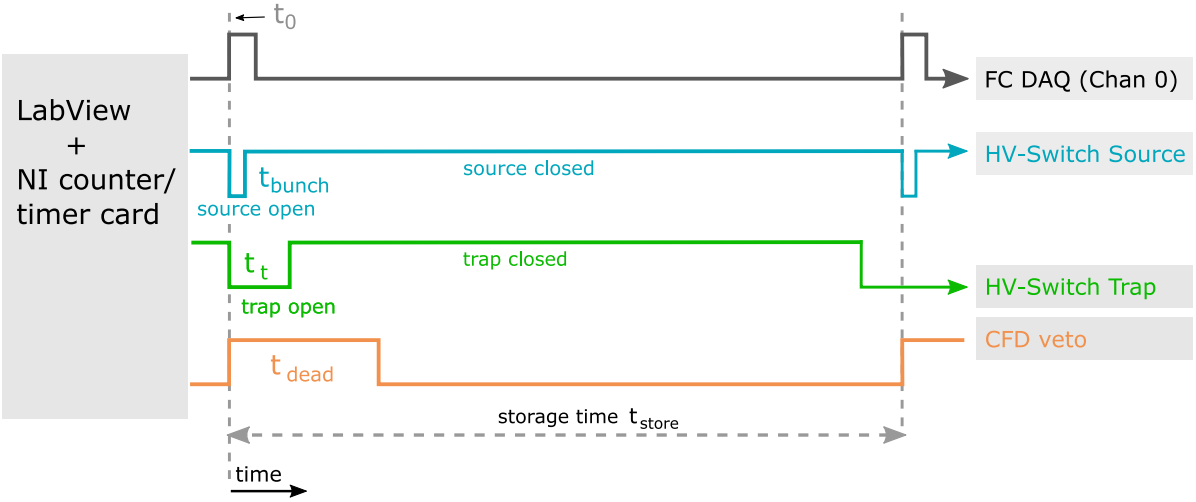

Figure 5.11: Ion storage triggering scheme: Three TTL trigger pulses are generated by a National Instruments PCIe-6612 counter/timer card. (black) TTL trigger providing a global time reference t_0 for the DAQ system. All event timings are recorded relative to this reference. (blue) Triggering of the HV-switch to open the ion source and emit a bunch of length t_{bunch}. (green) Triggering of the HV-switch to open the trap entrance mirror and allow the ion injection. (orange) CFD veto trigger to suppress MCP events in the case of high count rates.

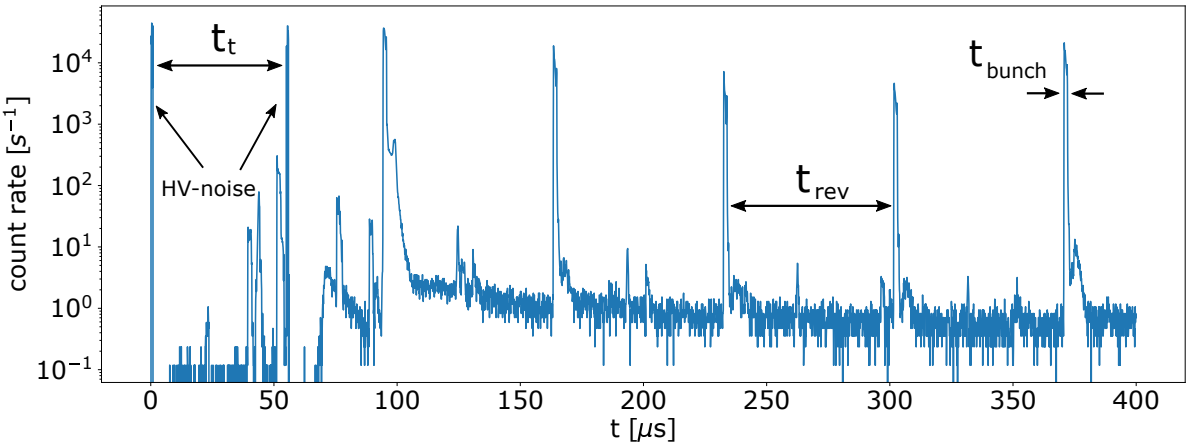

Figure 5.12: First 400 µs after injection of $^{133}Cs^+$ with 2500 eV. We plot the electron detector count rate depending on the ion tof. Ion revolution period $t_{rev} \approx 68.7\,\mu s$ and bunch length $t_{bunch} \approx 2\,\mu s$ are observed. Switching noise of the trap HV-switch indicates when the trap is opened and closed. For this measurement, no CFD veto was applied since the count rate was moderate.

5.3.2 Beam Lifetime and Ion Count

The storage signature observed in the EIBT can vary strongly with trap configuration, residual gas pressure and ion energy. In figure 5.13, we present exemplary the storage of Ar^+ with 2500 eV kinetic energy during a storage time of 2 s. The experiment has been performed at rather high pressure $P = 5 \times 10^{-8}$ mbar. The count rates on ion MCP (blue) and neutral MCP (green) have been measured simultaneously. As explained in section 5.2, on the neutral detector only events which originate from electron capture can be observed. On the ion detector, we expect to measure mostly events due to scattering on residual gas particles.

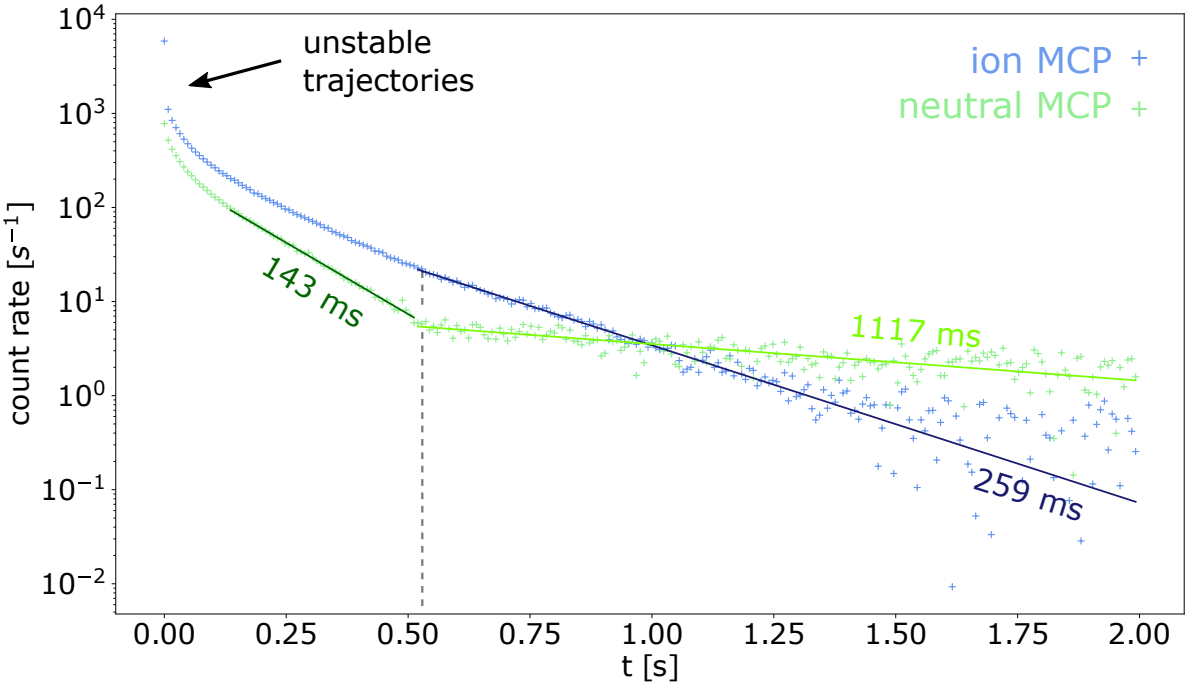

Figure 5.13: Ar^+ storage up to 2 s after injection. In the first 5 ms, the count rate drops by two orders of magnitude due to ions injected on unstable trajectories. Thereafter, regions of different lifetime are observed. This count rate has been averaged over 25989 injections.

We observe an early drop of the count rate by about one order of magnitude in the first 5 ms. This time interval corresponds to approx. 135 ion bunch revolutions. Hence, this drop can be attributed to ions which revolve on unstable trajectories and are lost from the trap after a few oscillations [30]. After 5 ms, a slower but still over-exponential decay is observed. In our interpretation, this is due to intra-beam scattering. During these early storage times, the ion count is still relatively high and the ion bunch is compressed in the mirrors close to the turning regions which can increase the density by several orders of magnitude [35]. After this, we can identify an exponential decay of the ion detector count rate from approx. $t \approx 520$ ms on with a lifetime of $\tau^{ion} \approx 259$ ms. This behaviour qualitatively agrees with the observed decay in other EIBTs

[22, 30] and the lifetime is comparable to the literature values provided in table 2.1. However on the neutral detector, we observe an exponential decay between $t \approx 133\,\text{ms}$ to $520\,\text{ms}$ with a lifetime of $\tau_1^{neutr} \approx 143\,\text{ms}$. Then, a sudden change in the decay rate is observed and a region with a lifetime of $\tau_2^{neutr} \approx 1117\,\text{ms}$ follows. The cause of this behaviour is not clear. Around $t = 520\,\text{ms}$, both decays show a qualitative change which indicates a change in dominating loss mechanism. Possible mechanisms are electron capture, elastic scattering, perturbations by unstable trap potentials and intra-beam scattering. Each loss mechanism alters the stored ion count and is expected to influence the decay rate on both detectors. However, when ions are scattered from the bunch to the ion detector, it is expected that mainly ions from the outer beam region are detected [22]. Thus, geometric effects can influence the observed decay when the ion count and bunch size decreases over time.

We can estimate a lower limit for the number of stored ions from the measured loss:

$$N_{stored} = 2\left(\frac{\Sigma N_{ion} + \Sigma N_{neutr}}{N_{inj}}\right) = 2\left(\frac{4823483 + 4797939}{25989}\right) \approx 740 \tag{5.5}$$

where we add the total count on ion and neutral detector, ΣN_{ion} and ΣN_{neutr}, and divide by the number of injections N_{inj} to obtain the average loss for one storage cycle. The factor of 2 accounts for the fact that ions can leave the trap in both directions. From this lower limit, we expect to store an ion number on the order of 10^3. Hence, we store significantly less ions than other EIBTs (see table 2.1). This is expected since the detector tubes restrict the trap phase space. For most REMI experiments, this is not a disadvantage. A larger phase space would also mean larger uncertainties in reaction position and transverse target momenta. If a higher number of ions is required for certain experiments, the injection procedure and the beam emittance provided by the ion source can be improved.

5.3.3 Neutral Background and Beam Profile

Information on the stored Ar^+ beam presented in the previous section can be extracted from the neutral detector picture presented in figure 5.14 (top). Around the center, we observe molecules which are lost from the stored beam due to neutralization in the residual gas. Ions can neutralize at any position in the beam and then propagate on with their momentary velocity. The observed structure is a projection of the transversal phase space which the stored ion beam occupies, averaged along the trap axis. It can be argued that we mainly observe the phase space projection from the REMI region. This is because the MCP efficiency decreases for lower kinetic energy of the neutrals as shown in [70]. This energy is maximal in the REMI center. Regions in which the beam profile differs strongly, like the turning regions in the trap mirrors and the crossing of strong Einzel-lenses, are also regions of high potential/low kinetic energy and thus contribute less to the observed phase space [54]. An intense neutral spot is located at (x,y) = (−1.4 mm, 0.2 mm) which is interpreted as beam signature from the REMI region. Additionally, a weak, circular background of approx. 18 mm diameter is observed.

Uncertainties in Target Preparation. In the bottom of figure 5.14, the detector picture projection on the x-axis is shown. The beam spot exhibits a FHWM of 2.1 mm in x- and y-direction. This can be interpreted as upper limit for the transverse beam size, i.e. for the uncertainty in reaction position $\Delta x_0 = 2.1\,\text{mm}$. The maximal angle of the observed neutrals can be calculated from the observed spot to be $tan(\theta_{max}) = \frac{2.1\,\text{mm}}{151\,\text{cm}} \approx 1.4 \times 10^{-3}$. This corresponds to an initial transversal momentum uncertainty of $\Delta p_{0,x} \approx tan(\theta_{max}) \cdot p_{0,z} = 2.28\,\text{a.u.}$ If a more accurate characterization of the beam size in the interaction region is required, neutralization has to be induced more localized, e.g. in the $z = 0$, plane. This can for example be achieved by photodetachment of negatively charged ions. Then, it is possible to back-propagate the spot size from the neutral detector picture to $z = 0$ by employing the β-function. This is a machine-specific function which can be obtained by simulating the trap phase space. Descriptions are provided in [31] and [54] (p.78).

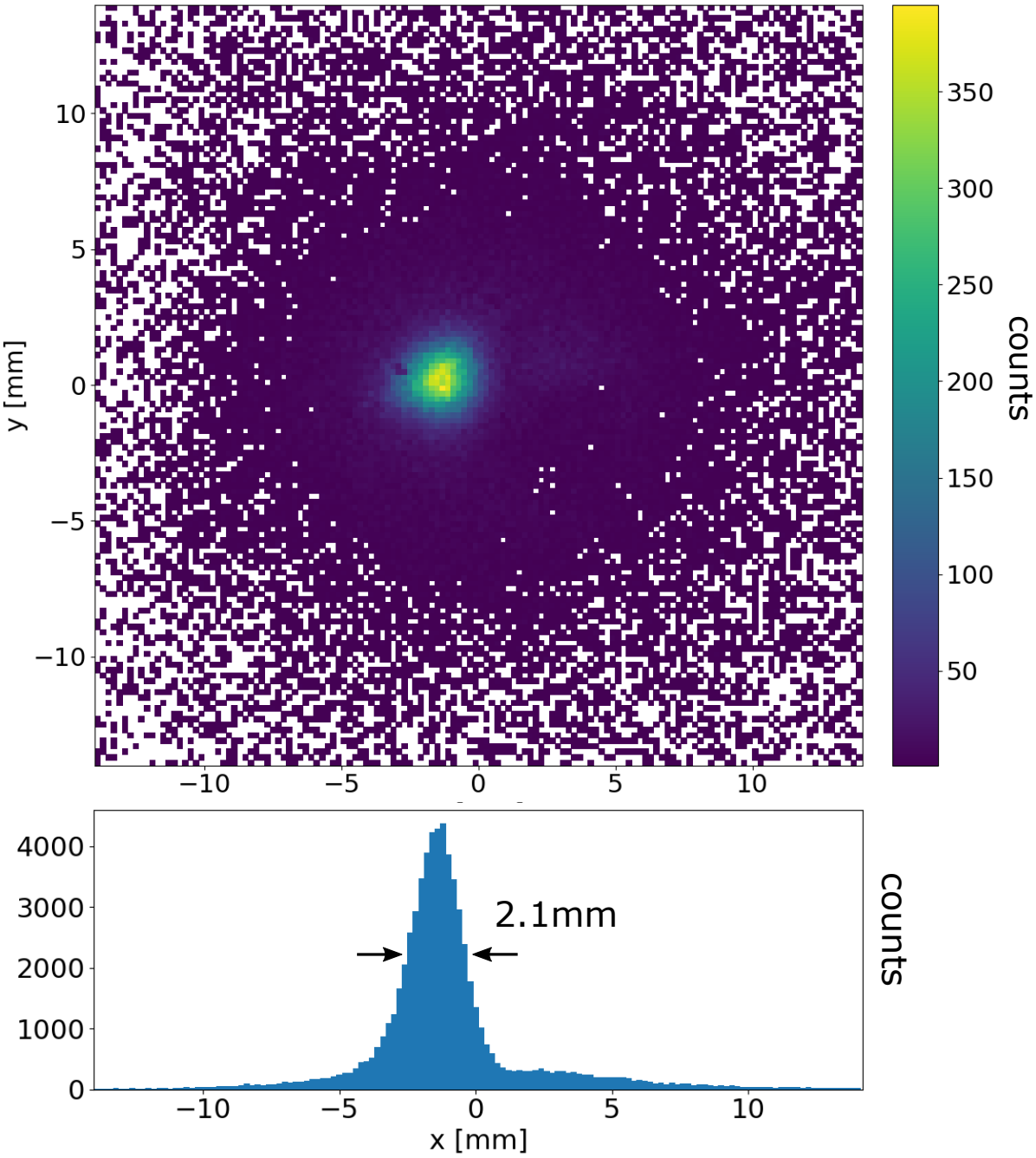

Figure 5.14: (top) Neutral detector picture for ion storage, monitoring the beam phase-space averaged along the trap axis. (bottom) x-projection of detector picture. This storage has been performed with trap "config 4", listed in table 9.3.

5.3.4 Bunch Dynamics

Ion bunch dynamics have been investigated extensively in previous EIBT experiments [35], [71]. Due to their initial energy distribution, ion bunches disperse in most trap configurations. Under special conditions, a synchronization phenomenon is observed and the ion bunch shape is maintained during most of the storage time. This so called self-synchronization mode can be obtained under three conditions, discussed in detail by Pedersen et al. [35]:

- **Kinematical Condition**. Ions with more kinetic energy have to oscillate in the trap with longer revolution period, i.e. $\eta = \frac{dT}{dE} \geq 0$, where η is called slip factor. This can be achieved by adjusting the mirror potential slope such that ions with higher kinetic energy propagate an over-proportional longer path into the mirror. This is illustrated in figure 5.15.

- **Focusing Condition**. For a bunch of ions to synchronize, the individual ion phase spaces have to be coupled by collisions. This requires strong radial focusing at the turning points in the mirror which can also be controlled by the mirror potential.

- **Collision Condition**. The collision probability in the mirror region has to be in an intermediate regime. For too low probabilities, the bunch diffuses kinematically according to it's initial momentum spread. For too high probabilities, collisions can lead to enhanced diffusion.

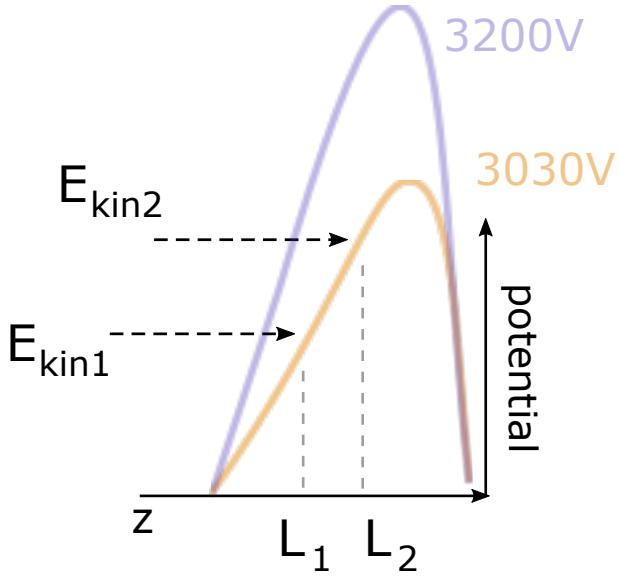

Figure 5.15: This graphic illustrates two things: (1) When the potential on the last mirror electrode is varied, the mirror potential shape changes. (purple) potential applied linearly. (orange) potential lowered at peak. (2) Ions with higher kinetic energy propagate a longer path into the mirror and experience different trap lengths L.

Figure 5.15 illustrates how the mirror potential changes close to the peak when varying the potential on the last mirror electrode V_{peak}. The case of 3200 V is the usual one in the sense that a linear mirror potential is applied. For 3030 V, the peak potential is lowered. This parameter changes slope and curvature of the potential and therefore the slip factor η as well as the radial focusing in the mirror. We identified voltage configurations in which the normal "dispersive" and the self-synchronization mode are observed. Figure 5.16 compares the bunch development for the two mentioned voltages. We present three 200 µs time windows for 5 ms, 50 ms, and 95 ms after injection respectively. The ions for V_{peak} = 3030 V (top) remain bunched for a longer time. At 95 ms, intensity has decreased but the bunch width has not changed. In the case of the linear mirror potential, V_{peak} = 3200 V (bottom), the bunches have broadened already after 50 ms. The extracted bunch widths for these two cases are presented in figure 5.17. In the dispersive mode with 3200 V, the width increases up to the ion revolution period of 68.7 µs. In the self-synchronizing mode with 3030 V it stays constant during the whole storage time of 100 ms. For this experiment, we stored $^{133}Cs^{+}$ with 2500 eV kinetic energy.

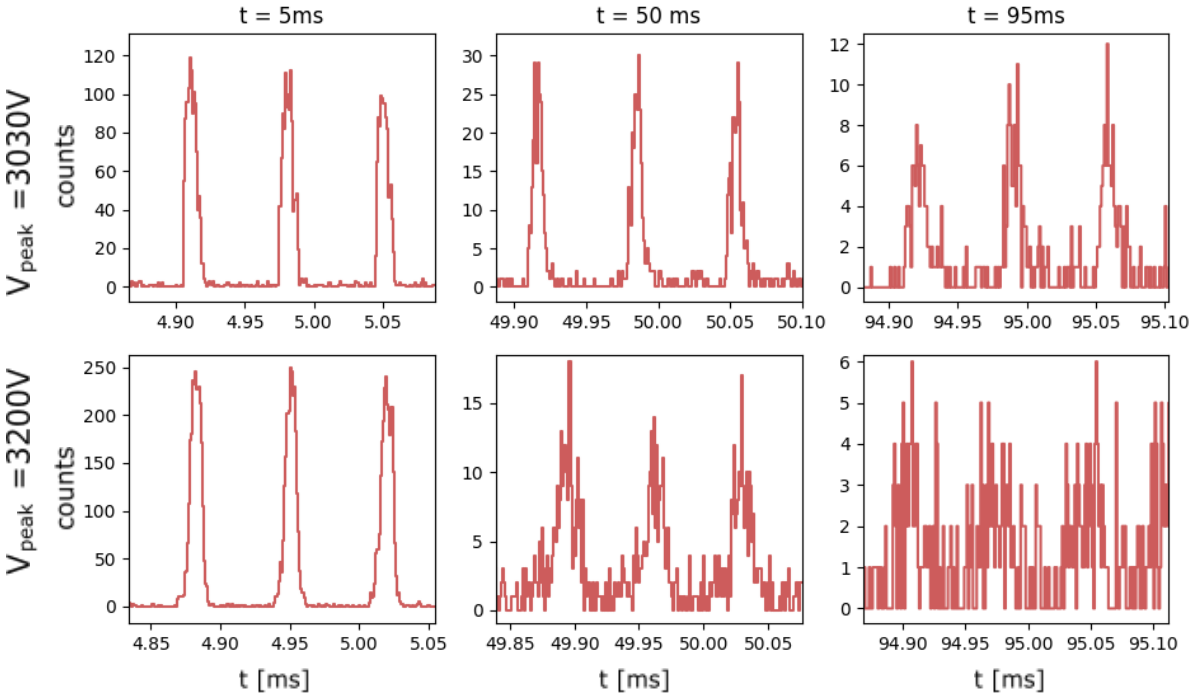

Figure 5.16: Comparison of bunching (top) and dispersive mode (bottom). We show the ion MCP signal for three time windows: around 5 ms, 50 ms and 95 ms after bunch injection. Figure adapted from [34]

This longitudinal dynamic is reflected in the frequency spectrum. Higher frequency components decay much slower in the self-synchronising state which is not shown here. Instead, we present a close view on the fundamental frequency in figure 5.18. In the case of the self-synchronizing mode,

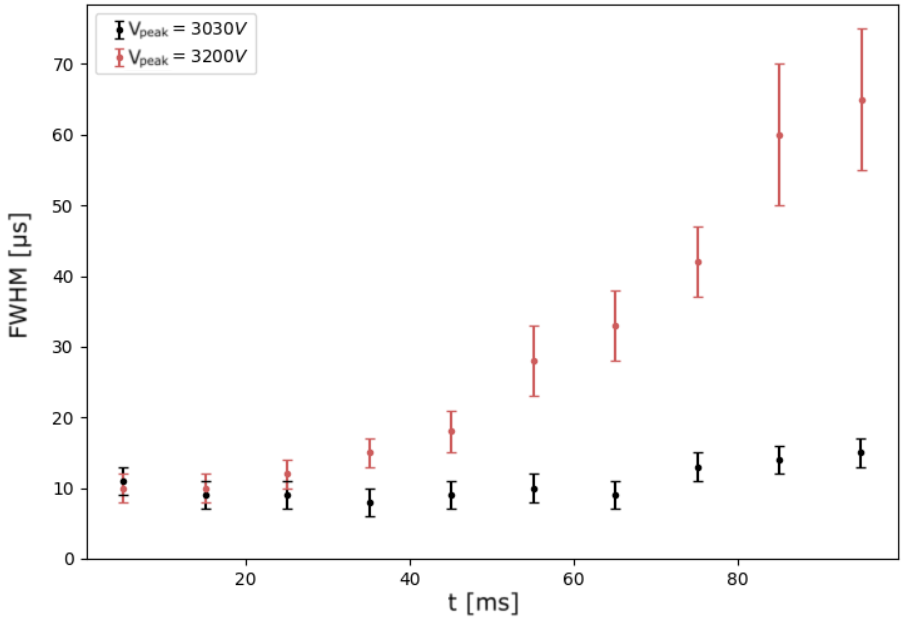

Figure 5.17: Development of the bunch width over 100 ms of storage. (red) In the dispersive mode, the bunch width increases until it reaches the ion revolution period and the bunch structure vanishes. (black) In the self-synchronizing mode, the width stays constant over the storage cycle of 100 ms. In this experiment we stored $^{133}Cs^{+}$ with $E_{kin} = 2500\,\text{eV}$. Figure adapted from [34]

the revolution frequency is shifted to lower values since the trap length is increased. In addition, the distribution is significantly sharper. An EIBT is a multi-pass time-of-flight mass spectrometer. For the relative mass resolution we can extract only an upper limit of $\frac{\Delta M}{M} = 2\frac{\Delta f}{f} < 10^{-4}$ since the peak FWHM is below the frequency resolution of this measurement. To increase the resolution, the experiment needs to be performed with a longer storage cycle.

This self-synchronization is not a purely kinematical phenomenon but additionally relies on collisional redistribution of momenta in the ensemble of ions. The narrowing in frequency distribution can indicate a smaller uncertainty in initial longitudinal target momentum. Therefore, this storage mode can be advantageous for REMI experiments. However, it has to be investigated how the transversal momentum distributions are effected.

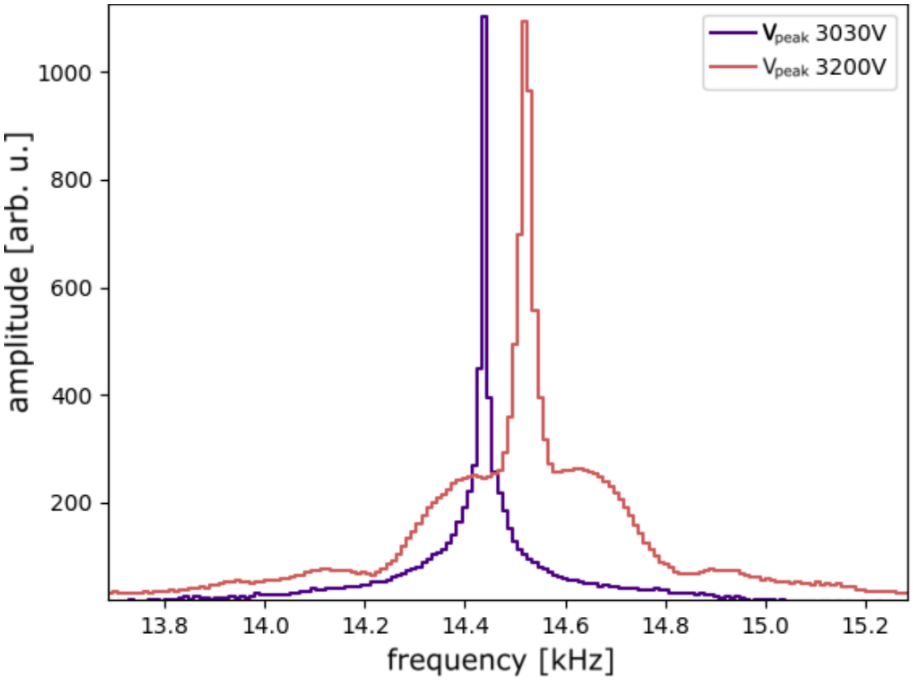

Figure 5.18: Fundamental frequency component of stored $^{133}Cs^{+}$. In the self-synchronizing mode, the distribution is shifted to lower frequencies and significantly sharper. Figure adapted from [34].

CHAPTER 6

PHOTODISSOCIATION OF THE MOLECULAR OXYGEN CATION

In this chapter, we present the first experiment on molecular ions performed with the TrapREMI setup. The photodissociation spectrum of O_2^+ has been investigated in the visible photon range, e.g. by McGilvery et al. [9]. A photodissociation pathway in the IR-regime has been used to even probe the shape of O_2^+ potential energy curves (PECs) [10]. However, in usual REMI experiments no neutral products are measured. Here, we induce the dissociation of stored O_2^+ by a 250 fs IR-laser pulse with a central wavelength of 1033 nm. We measure both reaction products, i.e. a charged O^+ and a neutral O, in coincidence which allows to extract information on the momentum spread in the stored target beam. This experiment constitutes the commissioning and provides a proof of principle for coincident momentum spectrometry on stored molecular ions in the TrapREMI. First, we provide a physical picture of the dissociation process in section 6.1. Then we describe the experimental preparation of target beam and IR laser in section 6.2. The observed photodissociation, product identification and analysis of coincident events is discussed in section 6.3. Finally, we reconstruct momenta of detected products and calculate the kinetic energy release of this photodissociation in 6.4.

6.1 Basics of the Dissociation Process

In this section, we provide a general picture of the physical processes which result in the observed photodissociation. We start with the **molecular excitation scheme** presented in figure 6.1 to illustrate the sequence of events, divided into the 3 following steps. Thereafter, we discuss each step in more detail.

1. **Electron impact ionization** in the ion source: The neutral molecule is promoted from the electronic ground state to an excited ionic state O_2^{+*} where a set of vibrational levels is

occupied according to the Franck-Condon principle (blue arrow).

2. **Photoexcitation** in the REMI: While the O_2^{+*} ions are stored in the EIBT and crossed with the laser, they can be resonantly excited to a dissociative PEC by absorbing an IR photon (red arrow).

3. **Dissociation**: When excited to a repulsive PEC, or with sufficient electronic/vibrational energy to a weakly bound PEC, the molecule dissociates to the $O + O^+$ continuum. The kinetic energy release (KER) of this process is carried by the products which can be detected in the REMI (black arrow).

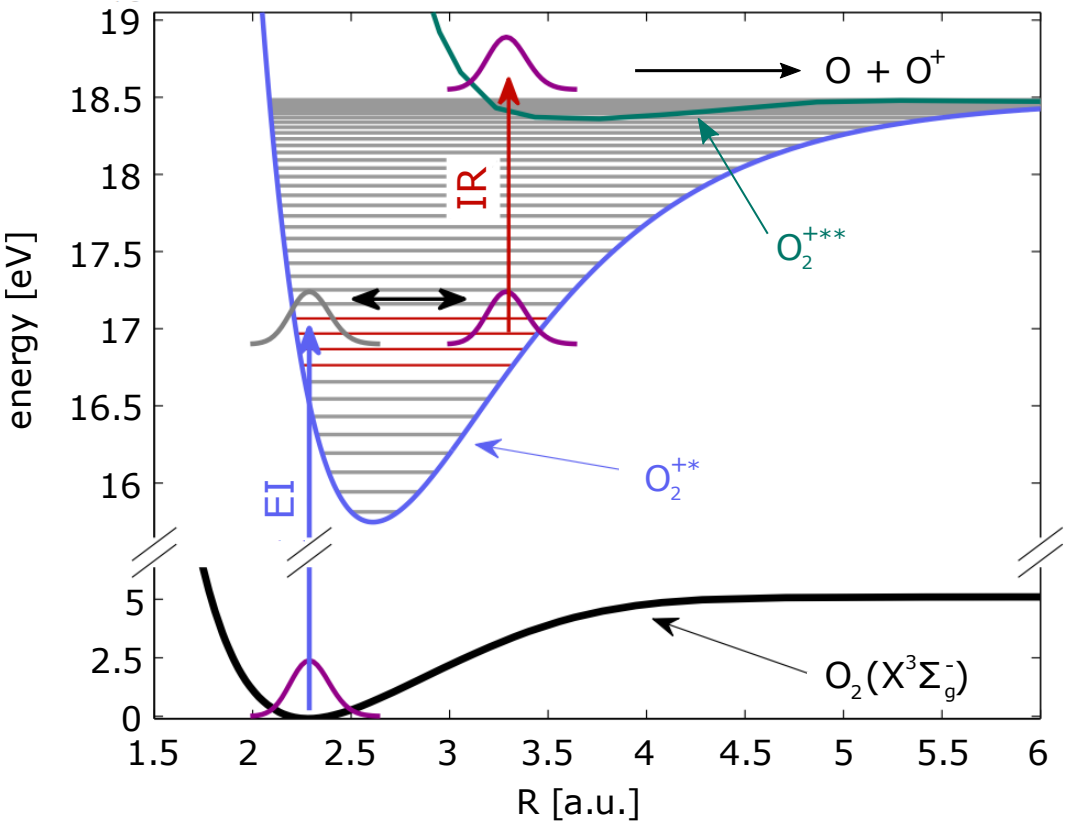

Figure 6.1: Scheme of O_2 photodissociation: In the ion source, the molecules are promoted from the neutral $O_2(X^3\Sigma_g^-)$ ground state to an excited, ionic O_2^{+*} PEC. A statistical mixture of vibrational states is occupied according to the Franck-Condon principle. Therafter, the ion can be excited by an IR photon to a repulsive or weakly bound PEC from which it can dissociate to the $O + O^+$ continuum. We plot the $O_2^+(f^4\Pi_g)$ and $O_2^+(a^4\Pi_u)$ PECs as examples. The PECs have been calculated in [7]. The neutral ground state PEC and vibronic wave function are extracted from [72]. Figure adapted from [10].

6.1.1 Electron Impact Ionization and Occupation of Vibrational States

In the first step, the oxygen molecules are ionized by collisions with electrons in the ion source. Figure 6.2 illustrates how the molecular state is modified by this process

The initial state is determined by the temperature of the O_2 gas which enters the ion source. At $T \approx 294.5\,\mathrm{K}$ the molecules carry an average energy of $\overline{E} = k_B T \approx 25\,\mathrm{meV}$ per degree of freedom. In the electronic ground state ${}^3\Sigma_g^-$ of the neutral molecule, the energy separation between the ground and first excited vibrational states is $E_{v=1} - E_{v=0} = 192.5\,\mathrm{meV}$ [72]. Thus, it can be assumed that most neutral molecules are in the ground electronic and vibrational state. Figure 6.2 displays the PEC of this ground state (black) together with the vibrational ground state wave function (green). Both have been calculated by Bytautas et al. [72].

The ionization takes place fast compared to the timescale of nuclear motion which proceeds on the order of 10-100 fs [73]. Thus, the internuclear distance R can be regarded as constant during the process. As indicated by the vertical arrow in figure 6.2, the system is promoted to the ionic state where it occupies a statistical mixture of vibrational levels. The molecules can be excited to any ionic PEC for which the collision energy of the electron is sufficient. In the ion source, electrons can be accelerated to 110 eV. For kinetic energies between 60 eV and 100 eV, the electron's de Broglie - wavelength lies in the range of typical internuclear distances ($1.2 - 1.5\mathring{A}$) which maximizes the energy transfer to the molecule. However, there are several reasons why it is less probable that high-lying PECs get occupied. The electrons' mean kinetic collision energy is far below 100eV. This is because they can collide with and ionize O_2 molecules on all their trajectory while being accelerated from the rhenium filament towards the anode. Further, only a fraction of the available collision energy will be transferred to the molecule and 12.063 eV of this fraction are expended to ionize it [74]. Finally, the cross section for an excitation to a high-lying PEC decreases with the PEC energy. In conclusion, it is more probable that low-lying PECs are occupied.

The vibrational state occupation can be deduced by the Franck-Condon principle. It allows to calculate the probability amplitudes **P** of vibronic transitions, i.e. transitions which involve simultaneous changes in electronic and vibrational state. With the molecular dipole operator $\boldsymbol{\mu} = \boldsymbol{\mu_e} + \boldsymbol{\mu_n}$ for electrons and nuclei, we can write

$$\begin{aligned} \boldsymbol{P} &= \langle \Psi' | \boldsymbol{\mu} | \Psi \rangle \\ &= \langle \psi'_e \psi'_n \psi'_s | \boldsymbol{\mu_e} + \boldsymbol{\mu_n} | \psi_e \psi_n \psi_s \rangle \\ &= \langle \psi'_e \psi'_n \psi'_s | \boldsymbol{\mu_e} | \psi_e \psi_n \psi_s \rangle + \langle \psi'_e \psi'_n \psi'_s | \boldsymbol{\mu_n} | \psi_e \psi_n \psi_s \rangle . \end{aligned} \tag{6.1}$$

where $\Psi(\boldsymbol{r},\boldsymbol{R})$ and $\Psi'(\boldsymbol{r},\boldsymbol{R})$ denote initial and final state depending on the set of electronic

$\boldsymbol{r}$ and nuclear $\boldsymbol{R}$ coordinates respectively. Additionally, we wrote the overall wave function $\Psi(\boldsymbol{r},\boldsymbol{R}) = \psi_e\psi_n\psi_s$ in Born-Oppenheimer approximation as a product of electronic, nuclear and spin part. By further assuming that the electronic transition dipole matrix element $\langle\psi_e|'\boldsymbol{\mu_e}|\psi_e\rangle$ varies only slowly with $\mathbf{R}$, which is called the Condon approximation, we can factorize $\mathbf{P}$ like

$$\begin{aligned}\mathbf{P} &= \langle\psi_n'|\psi_n\rangle\langle\psi_e'|\boldsymbol{\mu_e}|\psi_e\rangle\langle\psi_s'|\psi_s\rangle + \langle\psi_e'|\psi_e\rangle\langle\psi_n'|\boldsymbol{\mu_n}|\psi_n\rangle\langle\psi_s'|\psi_s\rangle\,. \\ &= \langle\psi_n'|\psi_n\rangle\langle\psi_e'|\boldsymbol{\mu_e}|\psi_e\rangle\langle\psi_s'|\psi_s\rangle\end{aligned} \tag{6.2}$$

where the second summand vanishes since different electronic states are orthogonal $\langle\psi_e'|\psi_e\rangle = 0$. The first term is the so-called **Franck-Condon factor** $\langle\psi_n'|\psi_n\rangle$. It states, that the transition probability amplitude is proportional to the nuclear wave function overlap of initial and final state. From the second and third term, angular momentum and spin selection rules can be deduced. A detailed description of this topic is provided by Atkins and Friedman [75]. Figure 6.2 shows the vibrational wave functions for quantum numbers $v = 0, 5, 10$ and 15 and illustrates their occupation by exemplarily plotting the Franck-Condon factors as purple dots on the left.

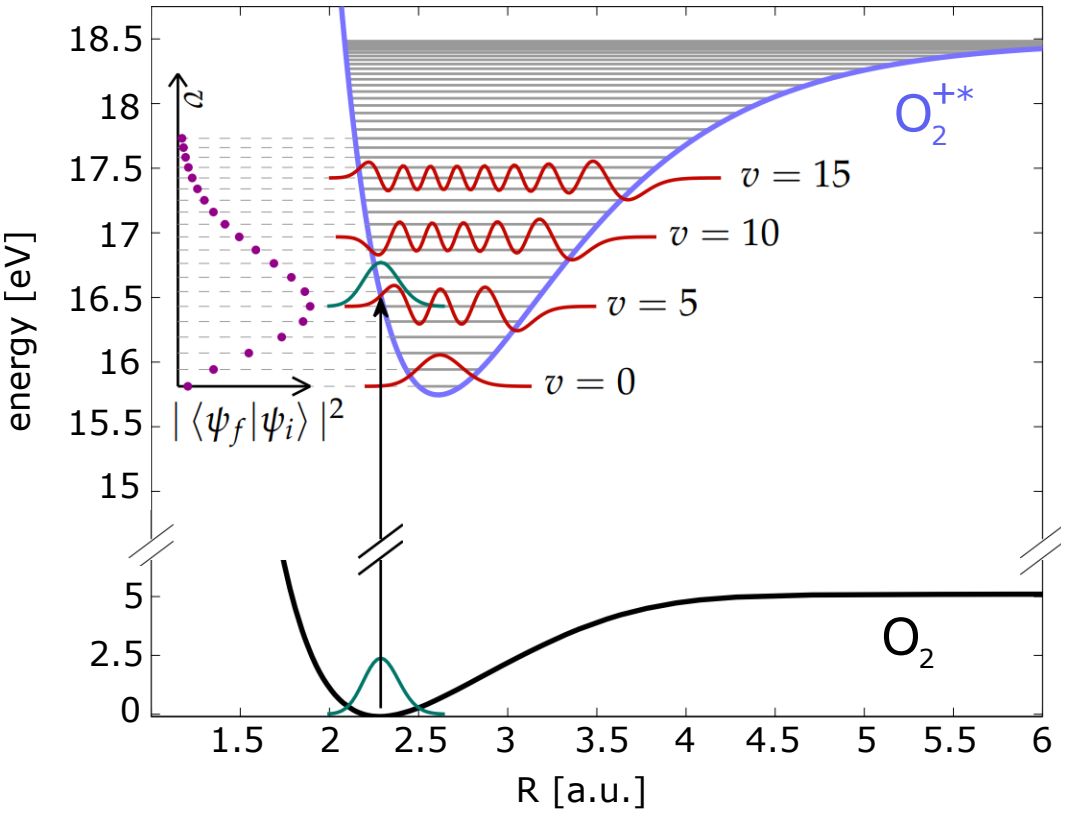

Figure 6.2: Scheme of electron impact ionization (EI) in the ion source: Neutral oxygen molecules in the vibronic ground state are ionized and promoted to an ionic PEC. As discussed in the text, the occupation of low-lying PECs is most probable. Further, the occupation depends on the nuclear wave function overlap between initial and final vibrational states. These overlaps, also called Franck-Condon factors, are plotted as purple dots in the inset and characterize the resulting statistical mixture of occupied vibrational states. Here, we exemplarily plot the wave functions for vibrational quantum numbers 0,5,10 and 15. Figure adapted from [10].

6.1.2 Photoexcitation and Relevant Potential Energy Curves of O_2^{+*}

In the second step, the ion is excited by an IR-photon while being stored in the trap. The initial PEC is stable on the timescale of the storage cycle. The final state is a repulsive or weakly binding PEC, i.e. with no or only a shallow minimum. First, we introduce the nomenclature which summarizes molecular quantum numbers and symmetry properties. Electronic molecular states are labeled with term symbols of general form

$$^{2S+1}\Lambda^{+/-}_{g/u} \tag{6.3}$$

where S is the total electron spin quantum number, Λ the projection of the orbital angular momentum on the internuclear axis, g/u (gerade/ungerade) denotes the wave functions parity [1], i.e. symmetry with respect to point inversion at the center-of-charge and +/- the symmetry with respect to reflection at an arbitrary plane which contains the internuclear axis [73] (p. 60). We can apply three assumptions to restrict the set of relevant PECs:

- The initial PEC is an excited state O_2^{+*}. The ionic ground state lies approx. 6 eV below the first dissociative curve. Given the IR-intensities estimated in the following section 6.2.3, it is not probable that the photodissociation occurs from the ground state.
- Low-lying PECs within the Franck-Condon region are most probable to be occupied as discussed in section 6.1.1. Thus, we neglect high-lying PECs for the explanation of the observed signal.
- Only transitions between PECs which satisfy the electric dipole selection rules for single-photon transitions are considered relevant.

For multi-atomic, nonlinear molecules, group theory is employed to deduce the dipole selection rules [73] (p. 266). In the simpler case of a homonuclear, diatomic molecule like O_2^+, symmetries and the coupling between the different angular momenta have to be considered. These couplings are described by Hund's cases [73] (p. 61). The electric dipole selection rules for single-photon transitions in O_2^+ are

- total electron spin $\Delta S = 0$
- total electron orbital angular momentum $\Delta\Lambda = \pm 1$
- total angular momentum: $\Delta J = \pm 1$
- parity $g \rightarrow u$ or $u \rightarrow g$

[1] Note that the g/u symmetries are only defined for homonuclear diatomic molecules. For heteronuclear molecules, the symbol of the according group representation is used.

Further, the relative orientation of laser polarization and molecular axis plays a role for which transitions are allowed. Dunn et al. summarize possible transitions for orientation parallel and perpendicular to the laser polarization in the case of diatomic, homonuclear molecules, in [76]. In this experiment, the molecules are expected to enter the interaction region with arbitrary orientation.

According to these conditions, we extracted a selection of O_2^+ PECs, calculated by Marian et al. [7]. We color-coded the stable and dissociative PECs and marked the Franck-Condon region with dashed, green lines. The latter has only an illustrative purpose and indicates the region of internuclear distances in which the initial wave function is promoted vertically to the excited PECs. By applying the dipole selection rules, we can identify 12 possible single-photon transitions to dissociating PECs. As an example, we indicate the transition from $^2\Pi_u$ to $^2\Sigma_g^+$.

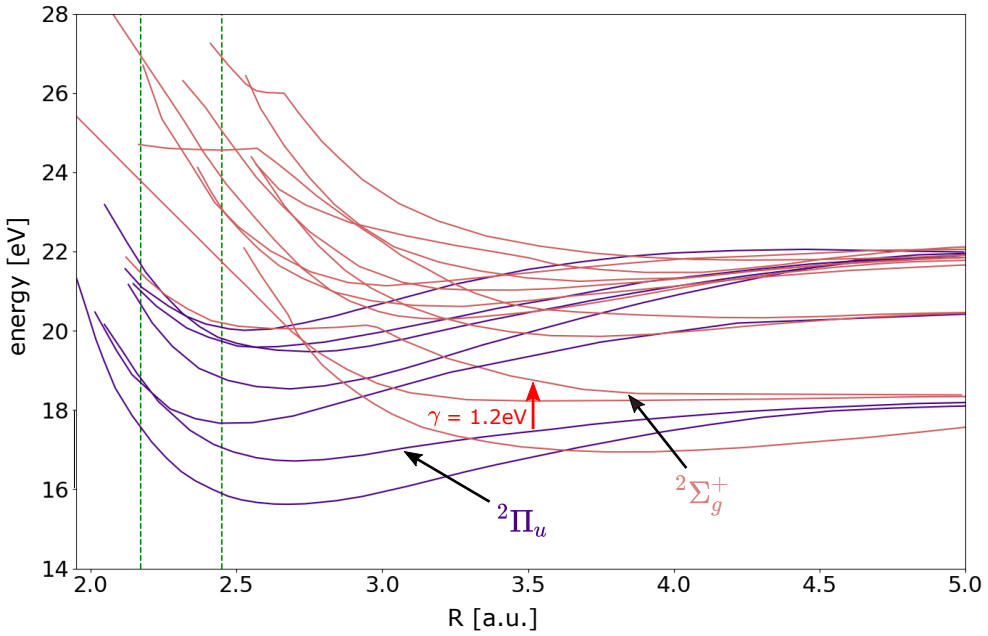

Figure 6.3: Selection of O_2^+ PECs calculated by Marian et al. [7], grouped by color in stable and dissociative ones. The Franck-Condon region for electron impact ionization in the previous step is indicated by green, dashed lines. A red arrow illustrates an exemplary excitation from the $^2\Pi_u$ to the $^2\Sigma_g^+$ PEC with an 1.2eV photon.

6.1.3 Dissociation and Kinetic Energy Release

When the molecule has been excited to a repulsive PEC, it dissociates to the $O + O^+$ continuum. It is also possible that the molecule dissociates from a weakly bound PEC, given that it is excited to an energy which lies above the dissociation limit. A dissociation from a repulsive PEC is illustrated in a simplified picture in figure 6.4 with the same example of molecular PECs as in figure 6.3: The molecule has been excited by an IR-photon vertically to the $^2\Sigma_g^+$ - curve at $R \approx 3.5$ a.u.. From this PEC, it dissociates into O and O^+. The combined kinetic energy which these products gain, is called kinetic energy release (KER). It is the difference between the potential energy of the molecular geometry at which the transition takes place and the dissociation limit, i.e. the potential energy for $R \to \infty$.

$$KER = E(R_{trans}) - E(\infty) \tag{6.4}$$

In the case of products with equal mass, each of them carries the same kinetic energy, i.e. KER$= 2E_{kin}$. The description in figure 6.4 neglects vibrational and rotational contributions. The dissociations from PECs presented in figure 6.3 are estimated to result in a rather small product energies. In a similar experiment with slightly higher photon energies of 1.6 eV the dissociation via the transition $a^4\Pi_u \to f^4\Pi_g$ has been measured which resulted in a KER of 80 meV [10]. For the transition indicated in figure 6.4, a KER around 300 meV is estimated.

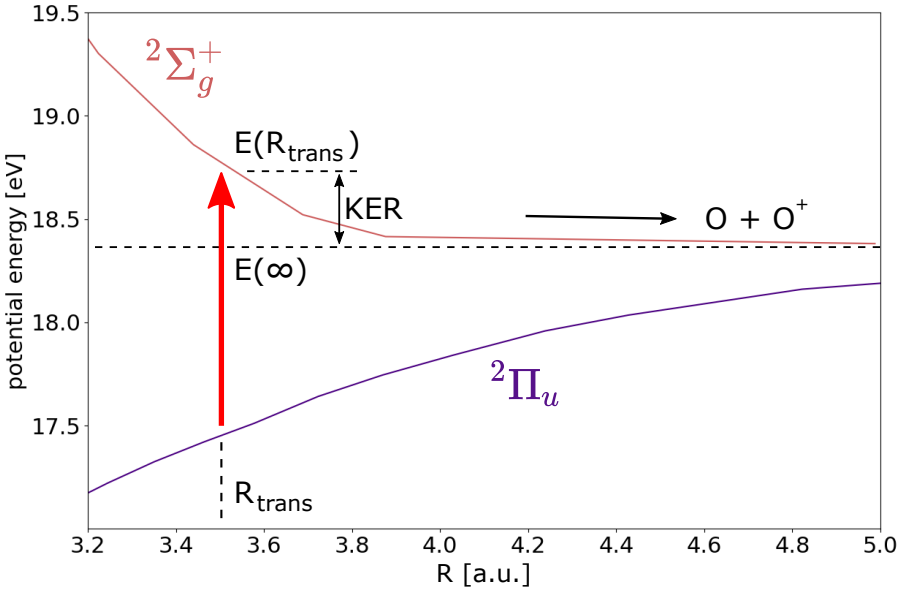

Figure 6.4: Simplified energy scheme for O_2+ dissociation. We exemplarily plot a possible transition between two PECs. When the molecule dissociates, the products gain the kinetic energy release (KER).

6.2 Experimental Preparation

6.2.1 Mass Spectrum and Ion Storage

Ion Mass Spectrum. To analyse which ion species are emitted by the source, we performed tof-mass spectrometry. The steerer of the source ion optics was pulsed for 1 µs to produce a short ion pulse. This pulse was detected approx. 5 m further at the neutral detector behind the EIBT. The tof-spectrum is presented in figure 6.5 together with a NIST reference mass spectrum for electron impact ionization [77]. The two most intense tof signals we observe correspond to mass 32 u and 16 u respectively.

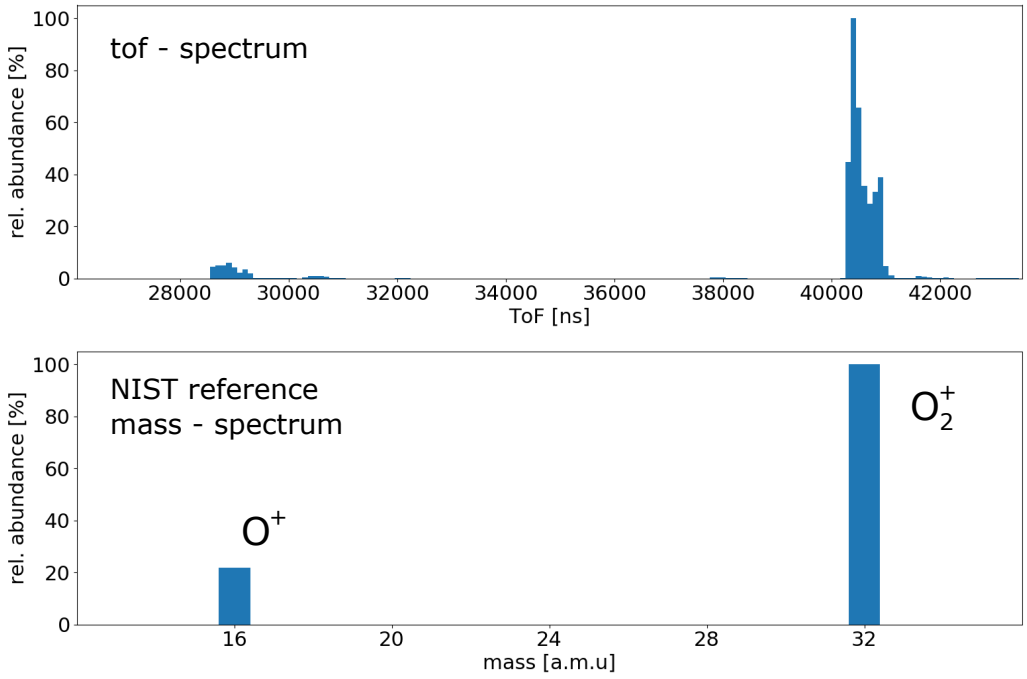

Figure 6.5: (top) Time-of-flight spectrum Oxygen pulse with 1μs length, recorded by the neutral detector behind the EIBT. (bottom) NIST reference spectrum for electron impact ionization of Oxygen [77].

Ion Storage. For the photodissociation experiment, we injected an approx. 30 µs long ion bunch with an ion kinetic energy of 2500 eV. The temporal bunch length was chosen to approximately match the revolution period in the trap so that the same is filled entirely. Usual output currents and source parameters for normal operation are listed in table 6.1. Higher currents of several 100 nA can be obtained by increasing the heating voltage. This however damages the rhenium filament over time. By measuring an ion current on the order of 10 nA on the Faraday-cup after the EIBT, we estimated the number of injected ions to be on the order of 2×10^6. Figure 6.6 shows the corresponding count rate on the ion MCP detector as well as the Fourier spectrum. The ions

Source Parameters		Output Current [nA]		Ion Properties	
heating voltage	0.2 arb.u.	after source	100	bunch length	30 µs
emission current	1 arb.u.	after trap	10	ion energy	2500 eV
extraction voltage	100 V			rev. period	33.7 µs
source pressure	7×10^{-6} mbar			Rev. Frequency	29.72 kHz

Table 6.1: Typical source parameters for O_2^+ ion production, output currents and ion parameter Note: The controller of the electron impact ion source allows to adjust heating voltage and emission current but does not display meaningful values of these quantities. Instead, it provides a reference value in arbitrary units which we list here.

revolve with a frequency of 29.72 kHz and a period of 33.7 µs respectively. The detector count rate decreases rapidly during the first few revolutions by a factor of 10^3 as can be seen from figure 6.6. We expect to store an ion number on the order of 10^3. Even though ions are stored much longer, we chose a short storage cycle of 10 ms to increase the overall count rate for the photodissociation experiment. To prevent ADC dead time, we suppressed all signals for the very first 120 µs by employing the CFD veto as described in section 4.3. The count rate during this time is very high due to HV-switching noise and high initial ion loss to all REMI detectors. We optimized the trap potentials to the values listed in table 9.2 as "config 2".

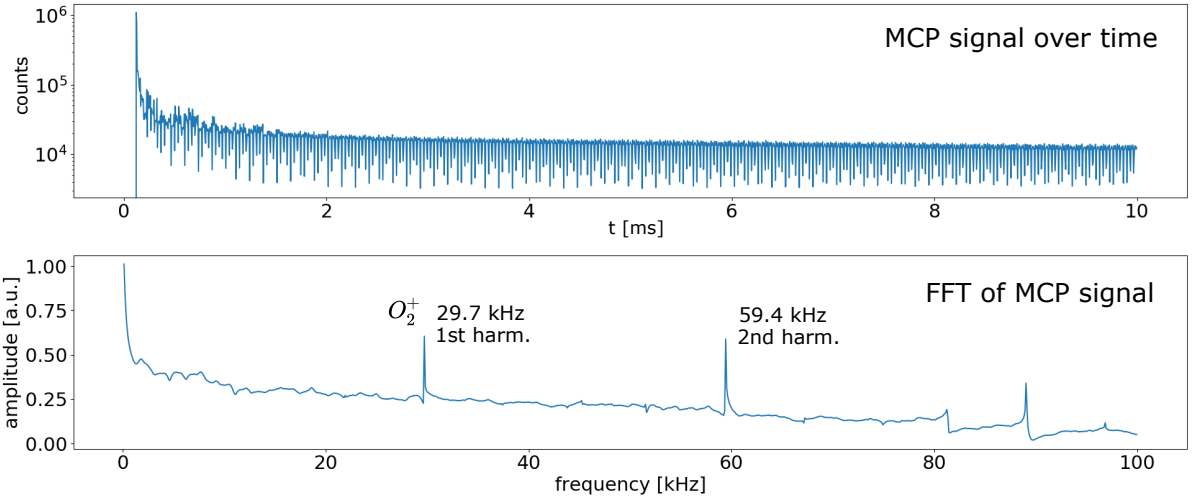

Figure 6.6: (top) Time trace of MCP counts on REMI detector while storage of O_2^+ with 2500 eV for 10 ms. The periodic structure mirrors the revolving ion pulse. (bottom) Fourier transform of the same time trace to extract revolution frequency and period.

6.2.2 Neutral Background and Beam Profile

Profile Interpretation. The detector picture in figure 6.7 (bottom) shows two spots, the dominant one is located at $(x_0, y_0, z_0) = (4.7\,\text{mm}, -0.7\,\text{mm}, 0\,\text{mm})$. This can indicate that the beam mainly revolves in two components. It is not clear however, which relative angle or spatial separation these components have in the interaction region. Another interpretation is that there is only one beam component and the two spots originate from different regions of the trap. Since we use electrostatic deflectors to compensate alignment imperfections, it is imaginable that the beam is slightly bent and thus exhibits two regions with slightly different angle. Ions which neutralize in these two regions would be projected onto two spots on the detector. The reaction region is not defined by the ion beam alone but by the overlap with the laser. In the case of two components it can be possible to overlap the laser with only one of them. Particularly when a tight focus is used, this can lead to a good definition of the interaction region.

Uncertainties in Target Preparation. Figure 6.7 (bottom) shows the x-axis-projection of the detector picture. The stronger spot dominates approx. by a factor of 3 and exhibits a FWHM of 3.6 mm. Assuming that the reaction is induced in this dominating component, the width can be interpreted as upper limit for the uncertainty in reaction position $\Delta x_0 = 3.6\,\text{mm}$. The uncertainty in initial transverse target momenta can be estimated by the maximal angle of these neutrals $tan(\theta_{max}) = \frac{3.6\,\text{mm}}{151\,\text{cm}} \approx 2.4 \times 10^{-3}$ to be $\Delta p_{0,x} \approx tan(\theta_{max}) \cdot p_{0,z} = 3.9\,\text{a.u.}$ According to equation 3.14, these two contributions result in an uncertainty of transversal reaction momentum of $\Delta p_{R,x} \approx 5.5\,\text{a.u.}$ For symmetry reasons, we assume the same uncertainty in y-direction. The momentum uncertainty estimations for this experiment are summarized in section 3.4.3.

The detector picture exhibits additional minor features: On the top, bottom and right-hand edge, counts are suppressed. This behaviour is related to the settings of hardware CFDs used in this specific experiment. On the left, there is a region indicated by a red, dashed line in which less counts are observed. This is a shadow cast by the Faraday-plate in front of the detector which can hinder particles to be detected in this region.

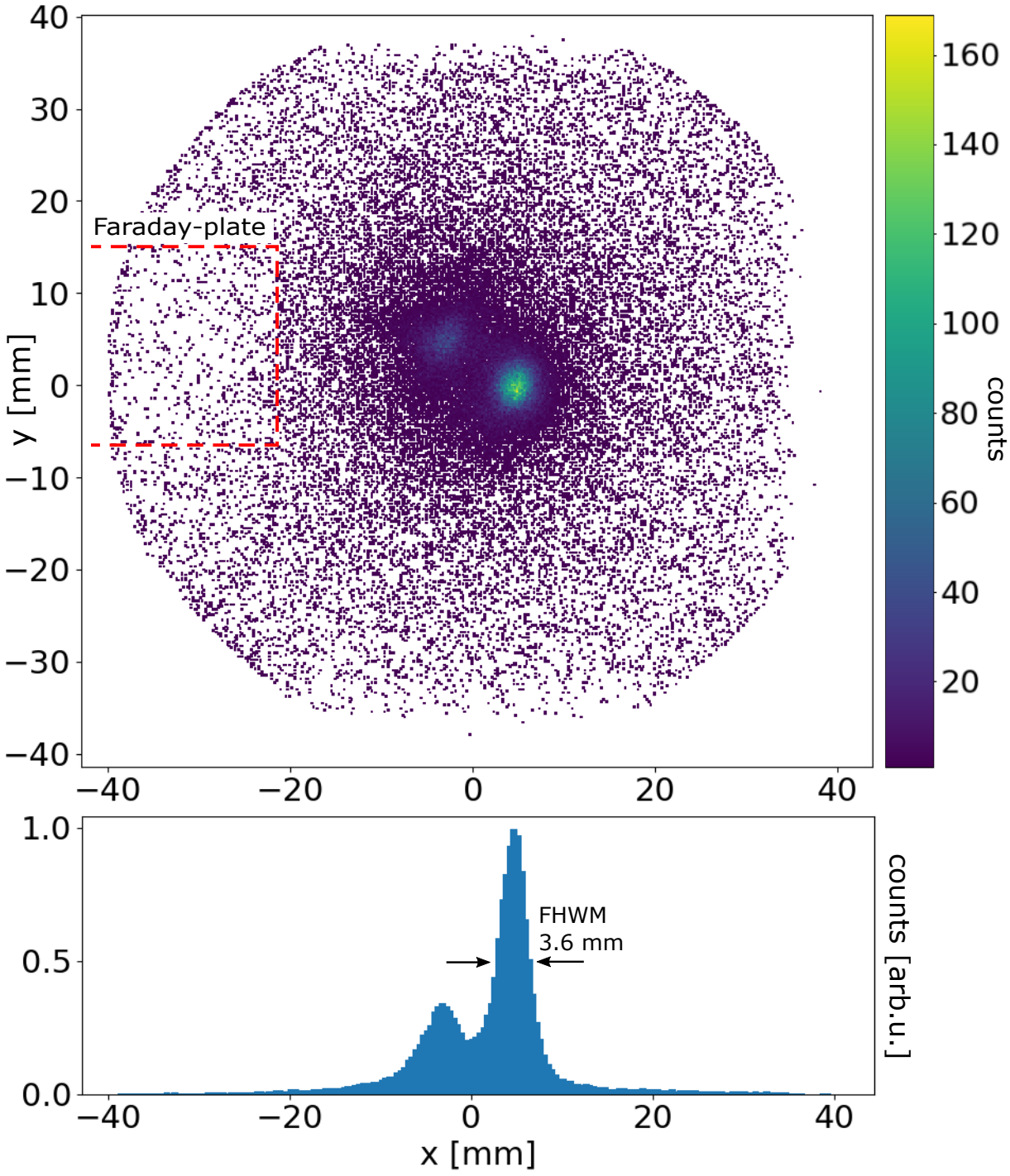

Figure 6.7: (top) Position of neutral loss from the stored beam on neutral detector. The structure indicates that the beam revolves in two components in the EIBT. On the left, a shadow is cast by the Faraday-plate and on the top, bottom and right-hand edge, counts are suppressed. This is related to hardware CFDs applied in this experiment. (bottom) X-axis-projection of detector picture. The right-hand component dominates approx. by a factor of 3 and exhibits a FWHM of 3.6 mm.

6.2.3 IR Intensity and Interaction Region

Figure 6.8 illustrates the IR laser, focused on the stored ion beam. We can estimate the IR intensity by assuming a Gaussian laser pulse [78]. Using the laser spot radius on the focusing lens $r_L \approx 1\,\mathrm{cm}$, the Gaussian beam waist w_0 can be calculated to

$$w_0 = \frac{\lambda}{\pi}\frac{1}{\Theta} \approx \frac{\lambda}{\pi}\frac{f}{r_L} \approx 33\mu m. \tag{6.5}$$

Where Θ is the half-divergence angle of the laser. Focal length f, central wavelength λ and other generic laser parameters are listed in table 6.2. From w_0, we can estimate the IR peak intensity in the focus to be

$$I_{peak} = \frac{E_{pulse}}{\tau_{pulse} A_{focus}} = \frac{E_{pulse}}{\tau_{pulse}\left(\pi w_0^2\right)} \approx 2 \cdot 10^{14} W/cm^2. \tag{6.6}$$

With the pulse energy E_{pulse}, length τ_{pulse} (FWHM) and cross-sectional area of the focus $A_{focus} = \pi w_0^2$. This estimation should be considered an upper limit. We intentionally introduced an astigmatism by slightly rotating the focusing lens to reduce signal background originating from residual gas ionization. Thus, we expect to operate in the mid $10^{13}\,\mathrm{W\,cm^{-2}}$-regime. As illustrated in figure 6.8, the Rayleigh-length

$$z_R = \frac{\pi w_0^2}{\lambda} \approx 3.3mm, \tag{6.7}$$

i.e. the longitudinal extension of the focus, exceeds the ion beam radius. The latter has an upper limit of $R_{max} = 2.25\,\mathrm{mm}$, imposed by the detector tubes which the ions have to pass. In conclusion, the IR intensity is moderate and multi-photon excitations of the stored molecules are expected to play a subordinate role. Further, the IR intensity is on the same order throughout all the beam overlap and so the photodissociation is expected to occur in the entire overlap volume.

Laser Parameters					
central wavelength λ	1033 nm	pulse length τ	250 fs	rep. rate r_{rep}	47 kHz
average power $\overline{P}$	90 W	pulse energy E_{pulse}	1.9 mJ	focal length f	1 m

Table 6.2: Nominal parameters of the laser setup. The Pulse length is given as FWHM of pulse intensity.

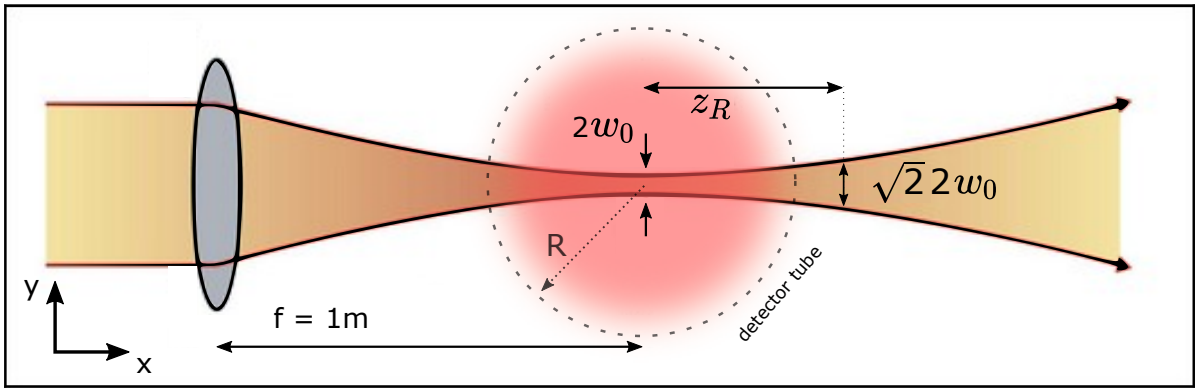

Figure 6.8: Focused IR laser and stored ion beam. The latter is depicted in a cross-sectional view as red cloud. The radial extension of the ion beam is restricted by the detector tubes with $R = 2.25\,\mathrm{mm}$ (indicated by dashed circle). Due to the rather long focal length of $f = 1\,\mathrm{m}$ and wavelength $\lambda = 1033\,\mathrm{nm}$, the Rayleigh-length $z_R = 3.3\,\mathrm{mm}$ exceeds the ion beam radius. Thus, the moderate IR intensity is expected to be on the same order throughout all the beam overlap.

6.3 Observation of Photodissociation

6.3.1 Laser-Induced MCP events

After ensuring that we store O_2^+ ions, we aligned the laser into the REMI, crossing it with the stored beam. The linear polarization was chosen in y-direction, i.e. perpendicular to the ion beam and to the REMI axis respectively as depicted in figure 4.13. The laser parameters in this experiment are summarized in table 6.2. We optimized the count rate to approx. $10\,\mathrm{cts\,s^{-1}}$ by varying the vertical laser focus position with the last mirror before the REMI and by shifting the focusing lens along the laser beam axis. That is, we scanned the beam overlap in the x,y-plane. From this, we expect the laser to overlap with the dominating component of the stored ion beam which has been presented in figure 6.7 and that most of the dissociations will be induced around the respective position. Noticeably, the signal was rather insensitive on the lens position. The lens could be shifted by approx. $\pm 5\,\mathrm{mm}$ while still obtaining a clear signal which fits our estimation in section 6.2.3 that we operate with a rather long focus.

MCP-Laser correlation spectrum. So far, the timing of all MCP events has been recorded relative to the ion injection which reoccurs every 10 ms. In order to observe a photodissociation signal on the ion detector, we subtracted the laser pulse timing from each ion MCP event. The laser pulses are monitored by a photo diode. The generated correlation spectrum is presented in figure 6.9. It ranges from 0 to approx. $21\,\mu\mathrm{s}$ which is the laser repetition time. For technical reasons, the creation of this spectrum is not straightforward. The details are explained in appendix 9.2. The correlation spectrum exhibits a strong peak around 2750 ns. This is the expected arrival time for O_2^+-fragments with $m = 16\,\mathrm{u}$ and $E_{kin} = 1250\,\mathrm{eV}$.

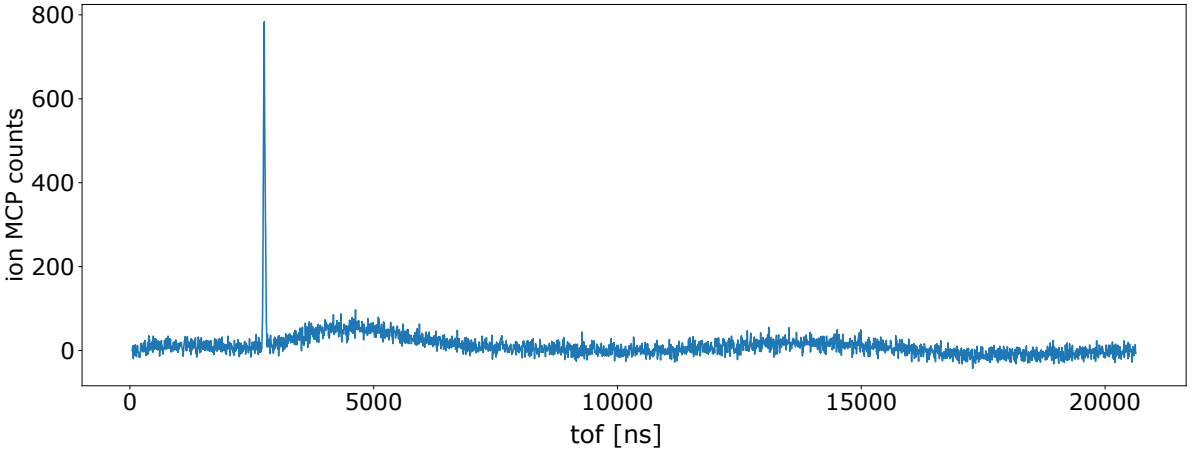

Figure 6.9: Correlation spectrum of laser and ion MCP event timing. The laser pulse can induce a reaction at t = 0. There is a strongly correlated MCP signal around 2750 ns and a background structure from residual gas ionization.

Retarding REMI spectrometer. This experiment has been performed without bake-out of the vacuum chambers at a residual gas pressure of 1×10^{-9} mbar. We observed significant residual gas ionization. To obtain a better signal-to-noise ratio, we applied ±30 V on the REMI spectrometer to accelerate residual gas ions away from the ion detector. This is an example of the different role of the REMI spectrometer in this setup with respect to conventional REMIs: As depicted in figure 6.10 the ions exhibit a high momentum p_0 towards the detector when the reaction takes place. Active ion extraction from the reaction region thus is not necessary in many cases. To the contrary, since the fragments in this experiment do not gain a high KER from the reaction, it is advantageous to decelerate them and so increase their acceptance. To ensure a homogeneous potential up to the detector, the grid and tube are set to a potential which linearly continues the one generated by the spectrometer.

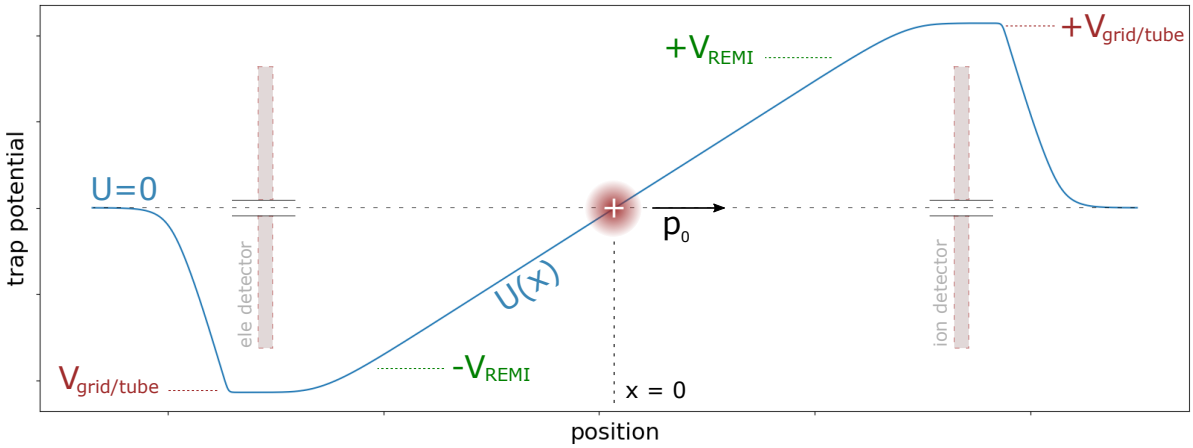

Figure 6.10: Simulated REMI potential from electron detector on the left to ion detector on the right as used in the presented experiments. Charged reaction products are decelerated by a potential ramp to increase their acceptance on the detector. Additionally, ions from residual gas ionization are withdrawn from the ion detector, resulting in a cleaner signal.

To identify the reaction products, we performed the experiment with three different retarding voltages on the REMI spectrometer (V_{REMI} = 30 V, 100 V, 200 V). Figure 6.11 presents a zoom on the obtained signals. With increasing voltage, the single peak splits into a double peak. However, only one peak moves to longer time-of-flights while the other stays constant. This indicates that we measure both products on the REMI ion detector: The constant peak results from neutral O and the moving one from charged O^+ which is retarded by the voltage. The O^+ signal is expected to be more intense since V_{REMI} increases the acceptance for charged products. The expected time-of-flight can be expressed as

$$tof = \frac{f\sqrt{m} \cdot 2d}{\sqrt{E_{kin}} + \sqrt{E_{kin} - qV_{REMI}}} \tag{6.8}$$

where we can work with the product mass m in u, charge q in e, distance d in cm, ion kinetic energy E_{kin} in eV as well as retarding voltage V_{REMI} in V and obtain tof in ns. The unit conversion factor is $f \approx 719.7$ [43]. Figure 6.12 presents the O^+ peak positions for the different retarding voltages. The best fit of equation 6.8 to this data is obtained for a fit parameter of $m = 15.69\,\mathrm{u}$ which indicates that we measure oxygen ions.

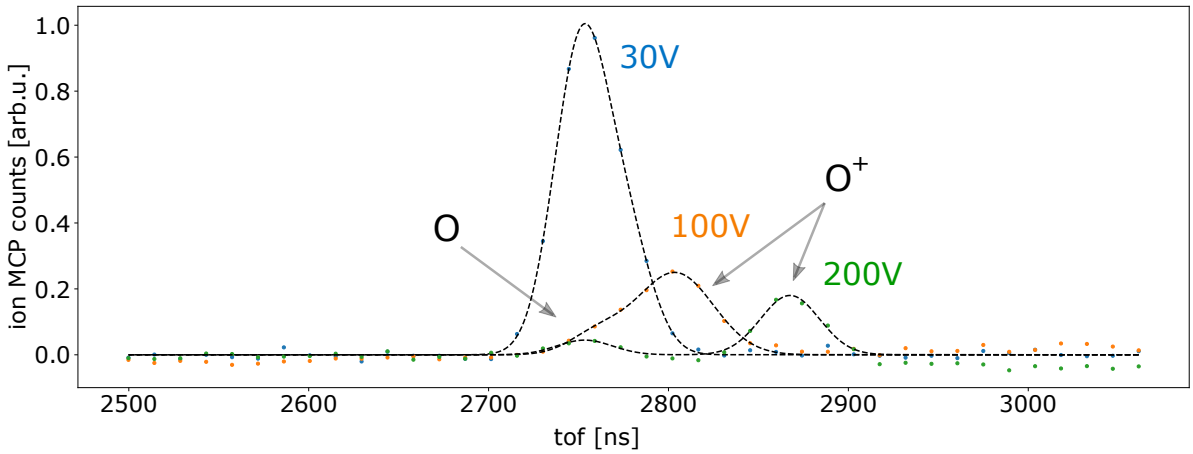

Figure 6.11: Tof on ion MCP relative to laser pulse for three experiments: with 30 V, 100 V and 200 V retarding voltage on the REMI spectrometer. The signal consists of two peaks which largely overlap at 30 V. With increasing voltage, one peak moves to longer tofs while the other remains constant. This indicates that the signal consists of a charged product which is retarded by the REMI voltage and a neutral product. The spectra have been normalized to the maximum of the 30V measurement for relative comparison.

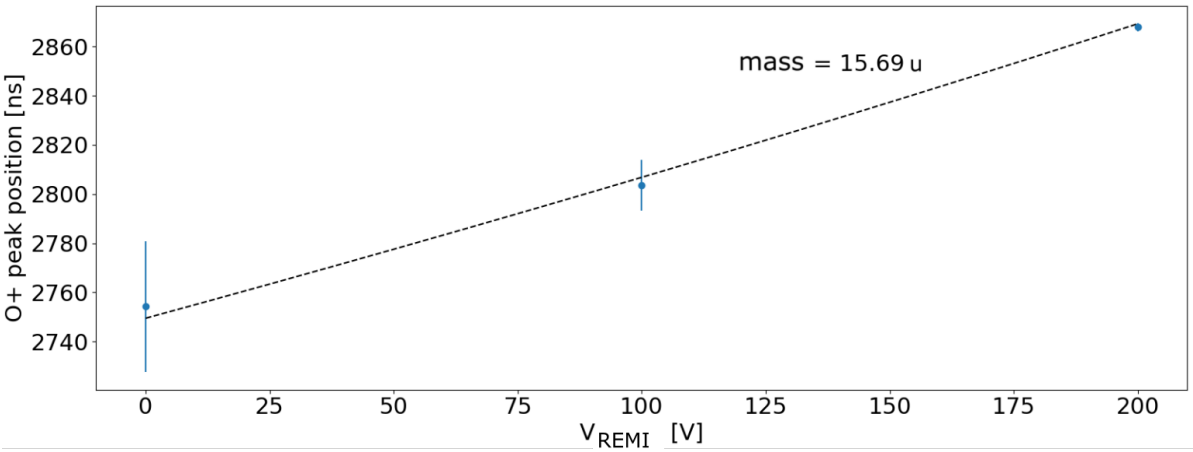

Figure 6.12: Charged product tof from figure 6.11 depending on retarding voltage. How much the product is decelerated depends on it's mass to charge ratio. Assuming a singly charged product, the fit of equation 6.8 yields a mass close to 16 u as expected from Oxygen.

6.3.2 The Neutral Detector Complementing the REMI

Usual REMI experiments detect all massive, charged products, namely electrons and ions. Photons involved in the reaction can usually be neglected in terms of momentum. Neutral products can not be extracted from the reaction region and if they are emitted towards the MCP, their kinetic energy is too small to induce secondary electron emission. Our setup however offers the advantage to detect neutral products as presented in figure 6.12. This is because the target ions are stored with high kinetic energy. The MCP efficiency for neutral atoms depends strongly on the impact kinetic energy which reaches a maximum around 1000 eV [70]. In the case of O_2^+, the initial 2500 eV are shared approx. equally between O^+ and O according to the mass ratio. However, the efficiency for O^+ is higher since the ion potential energy also contributes to the probability of secondary electron emission.

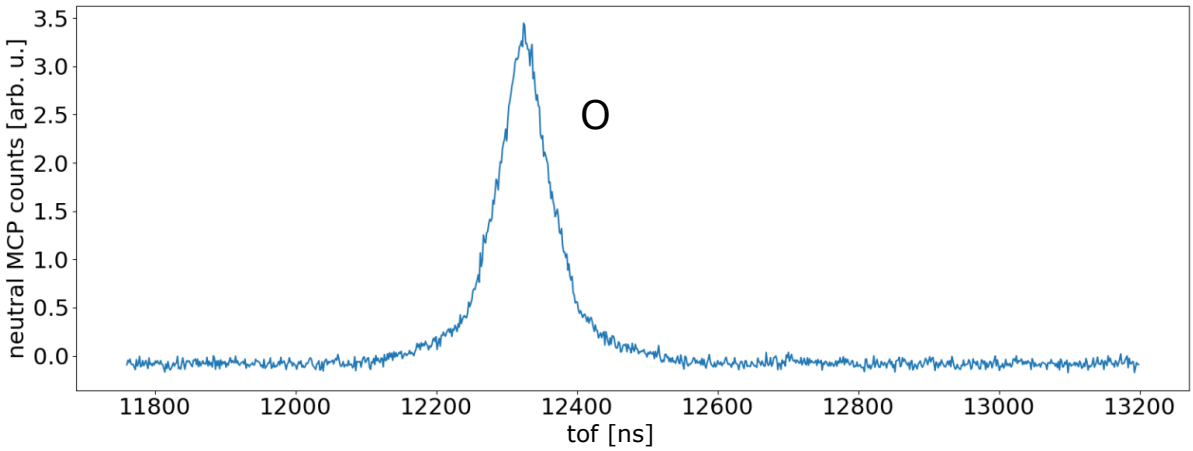

Figure 6.13: Time-of-flight on neutral MCP relative to laser pulse. The peak corresponds to neutral oxygen fragments from the photodissociation in the REMI. They originate with a central energy of 1250 eV and a distance of approx. 151 cm from the detector.

The neutral detector behind the EIBT complements the REMI detectors. When neutral reaction products are emitted with an angle to the trap axis smaller than 11 mrad, they can pass the ion detector tube and leave the trap towards the neutral detector. The events on the same are correlated with the laser as the time-of-flight plot in Figure 6.13 shows. The peak around $tof = 12300$ ns corresponds to neutral Oxygen fragments which originated in the reaction region approx. $d_{neutral} = 151$ cm from the detector with a central energy of $E_{kin} = 1250$ eV.

6.3.3 Detecting Fragments in Coincidence

The detection of coincident events, i.e. multiple products which originate from the same molecule, is a key feature of REMI experiments. As explained in section 3.4, it allows to obtain kinematically complete information on the reaction. Here, O_2^+ dissociates in two products, O^+ and O, which are emitted back-to-back with reaction momenta $\mathbf{p}_R^{O^+} = -\mathbf{p}_R^{O}$. Detecting only one product is in principle sufficient to determine the momenta of both particles. However, this is only true if the initial momentum of the target molecule is known. Looking at it the other way round, we can gain information on the initial target momentum by detecting both products in coincidence. Here, we analyse our data for coincident event pairs to provide a proof-of-principle and obtain information on uncertainties in initial target momentum and thus on the experimental resolution.

To select for coincident events, we programmed the Go4 data analysis to:

- count for each individual laser shot how many subsequent events have been detected within a time window of $T_{rep} \approx 21\,\mu s$, i.e. until the next laser shot arrived.
- If the count was 2, we plotted the time-of-flight of these events against each other, labeled tof1 for the event which has arrived first and tof2 for the event which has arrived second. Cases with a count of higher than 2 were very rare and thus negligible.

In this experiment, we detected two types of coincidences: ion/ion detector coincidences in which both products hit the ion detector as well as ion/neutral detector coincidences, i.e. pairs where the charged O^+ hits the ion detector while the neutral O leaves the EIBT and is measured on the neutral detector. The products can be distinguished by their time-of-flight.

Ion/Ion Detector Coincidences: The events recorded on the ion detector with $V_{REMI} = 200\,V$ have been analysed for coincident pairs. Figure 6.14, shows the corresponding time-of-flights. The anti-diagonal line indicates a correlation between the two products. This results from the mutual back-to-back repulsion during the photodissociation, i.e. from momentum conservation. Briefly speaking, this coincidence line shows that if one of the products arrives earlier at the detector, the other arrives later and vice-versa. The count of coincident pairs was 46401 out of 479643 total ion detector events, corresponding to a fraction of approx. 10%. One reason why mostly single events are recorded is the higher acceptance for O^+ due to the retarding potential, as we saw in section 6.3.1. Another reason is the finite efficiency of the detector due to which the detection probability decreases exponentially with the number of coincident particles. The coincidence line is suppressed on its lower-right end. Here, the time-of-flights of both products become close to equal as indicated by the red line. When detecting a particle, the detector is dead for a short time and no second particle can be detected. One reason is the finite width of the electronic signals. From this measurement, we can extract a dead time of approx. 15 ns which is below specified

values of commercial detectors [**?**]. The additional diagonal line as well the diagonal cut through the coincident events are expected to result from signal reflections in the electronics.

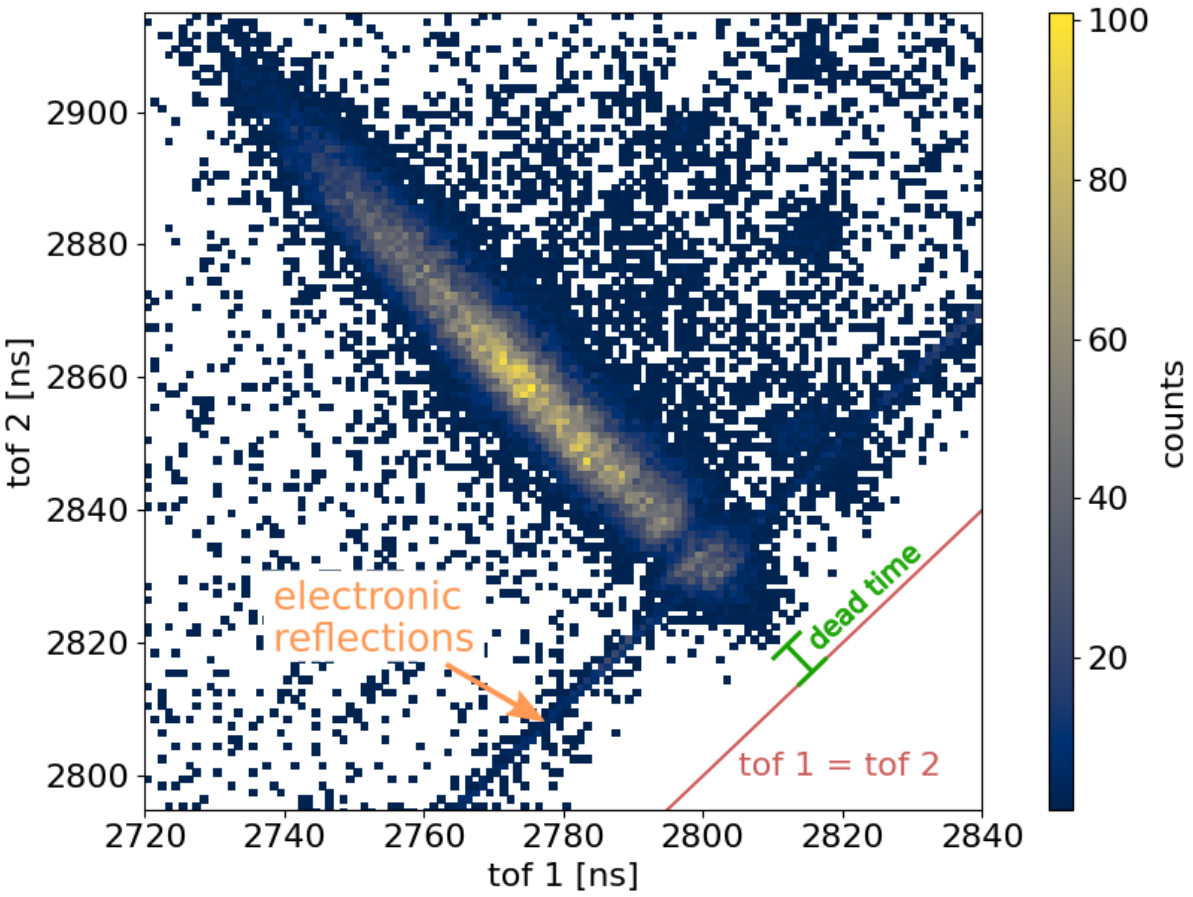

Figure 6.14: Ion/Ion Detector Coincidences. Tof of coincident event pairs, O on the x- and O^+ on the y-axis, both detected on the ion MCP. The line indicates a clear correlation which results from the back-to-back repulsion during the photodissociation, i.e. momentum conservation. Close to the line of equal time-of-flights $tof1 = tof2$, indicated by the red, dashed line, the coincident events are suppressed. For the detection of subsequent events, the detector exhibits a dead time of approx. 15 ns.

Ion/Neutral Detector Coincidences: The same coincidence analysis applied to the events on the ion and the neutral detector respectively yields the 2D histogram in figure 6.15. Again, a clear coincidence line is visible. With 1728 counts, this coincidence accounts for only approx. 0.4% of the observed photodissociations. For diatomic molecules, the detection of these event pairs on ion and neutral detector is a rather special case. The products repel each other and are emitted back-to-back from the reaction with $\mathbf{p}_R^{O^+} = -\mathbf{p}_R^{O}$. Thus, for a reaction taking place on the trap axis, either both products are expected to hit the ion detector or none. To investigate how this case can occur, we performed a Monte-Carlo simulation, varying the initial kinematic conditions. The results are presented in figure 6.16: We illustrate the setup geometry from reaction point on the left to neutral detector on the right. The distances are not to scale. The trap axis is represented by a dashed line. In the simulation, we varied the initial radial distance Δr of the O_2^+ ion to the trap axis and the transverse reaction momentum p_{trans} which the products gain. The inset shows the corresponding phase space plot: The red region indicates the phase space area for which this coincidence can be observed. For $\Delta r < 1.2\,\text{mm}$, the range of possible p_{trans} shrinks to zero. Thus, the observed products are expected to originate from a decentered position.

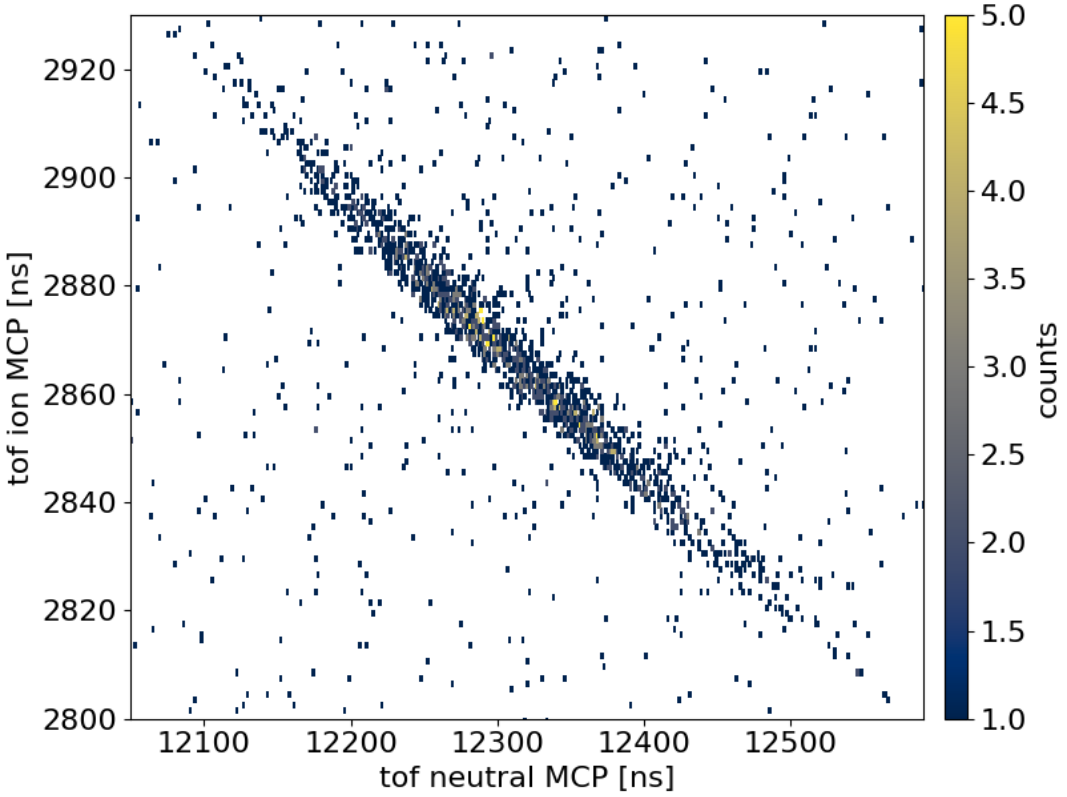

Figure 6.15: **Ion/Neutral Detector Coincidences**. Tof of events on neutral MCP (x-axis) and ion MCP (y-axis) plotted against each other. The line indicates a clear correlation which results from the repulsion during photodissociation. The distance to the neutral detector is approx. 4.5 times larger than to the ion detector. As a result, the tof distribution of O is broader by this factor.

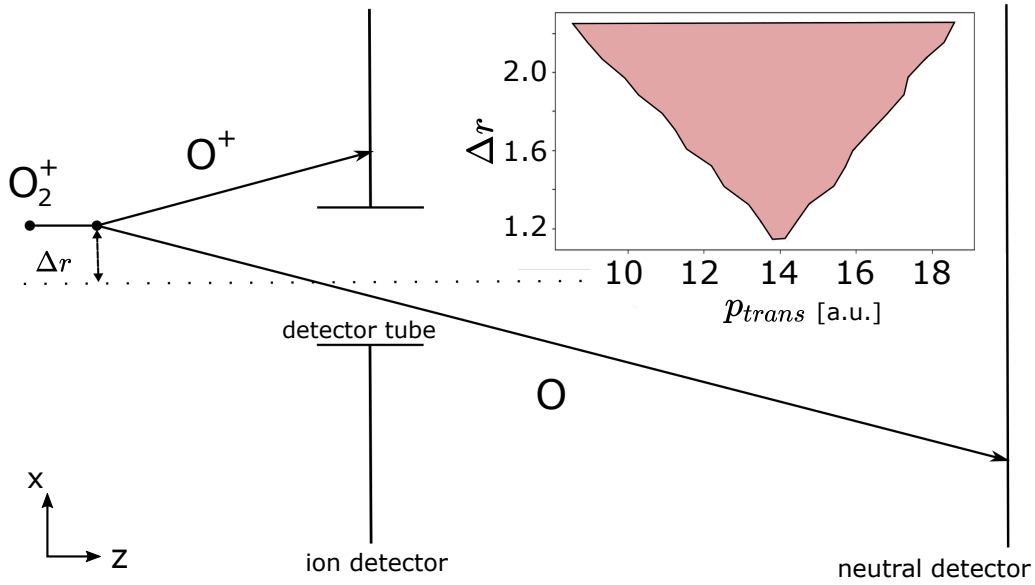

Figure 6.16: Scheme of O_2^+-photodissociation resulting in the detection of a coincident pair with O^+ on the ion detector and O on the neutral detector. For better illustration, the distances are not true to scale. The inset presents the simulated phase space for which this coincidence can be detected in our setup.

6.4 Momentum Reconstruction

6.4.1 Longitudinal Momentum

As described in section 3.4, we can reconstruct the longitudinal reaction momentum from the time-of-flight. Further, we need the distance d to detector and REMI spectrometer voltage V. Since d varies with the laser alignment into the REMI, we calibrated it using the neutral product. Because we expect the distribution of reaction momenta $p_{R,z}$ to be symmetric around zero, the mean reconstructed momentum of the neutral product

$$\frac{md}{\langle tof \rangle} \stackrel{!}{=} \langle p_{0,z} \rangle \tag{6.9}$$

should correspond to the mean initial product momentum $\langle p_{0,z} \rangle \approx 1637\,\text{a.u.}$ or energy of 1250 eV respectively. Doing so, we assume that the reaction takes place at $V(z=0)=0$. However, with the distance d also the potential $V(z)$ at the reaction position varies. In this case, the target molecules would enter the reaction with a modified $\langle p_{0,z} \rangle$. For a clean calibration of d, an experiment without applied REMI fields should be performed. Here, the data in figure 6.12 show that the position of the neutral peak is constant within the uncertainties of measurement, indicating that the above mentioned assumption holds. Similarly, we can calibrate V using the charged product

$$\frac{md}{\langle tof \rangle} - \frac{1}{2} q \frac{V}{d} \langle tof \rangle \stackrel{!}{=} \langle p_{0,z} \rangle \tag{6.10}$$

which originates in the same distance d. Thus, the distribution of longitudinal reaction momenta $p_{R,z}$ can be calculated by

$$p_{R,z} = \frac{md}{tof} - \frac{1}{2} q \frac{V}{d} tof - \langle p_{0,z} \rangle \tag{6.11}$$

The former 2D time-of-flight coincidence histogram 6.14 can thus be transformed into a 2D momentum histogram presented in figure 6.17. The individual products can gain over 20 a.u. of momentum along the trap axis from the reaction. The coincident events lie along the line of $p_{O} + p_{O^+} = 0$. This momentum conservation holds exactly for every single reaction. Therefore, the finite width of the coincidence line results from experimental uncertainties. As deduced in section 3.4.3, the uncertainty of longitudinal momentum is governed by the initial momentum spread of the stored target molecules $\Delta p_{0,z}$. The line profile, or in other words the distribution of initial target momenta, can be obtained from the momentum sum $p_{0,z} = p_{O} + p_{O^+} = 0$ for each coincident pair. It is presented in the bottom left of figure 6.17. When assuming a Gaussian distribution, it exhibits a standard deviation of $\sigma = 2.5\,\text{a.u.}$ which can be interpreted as the momentum resolution. This corresponds to an energy resolution of approx. 2.9 meV.

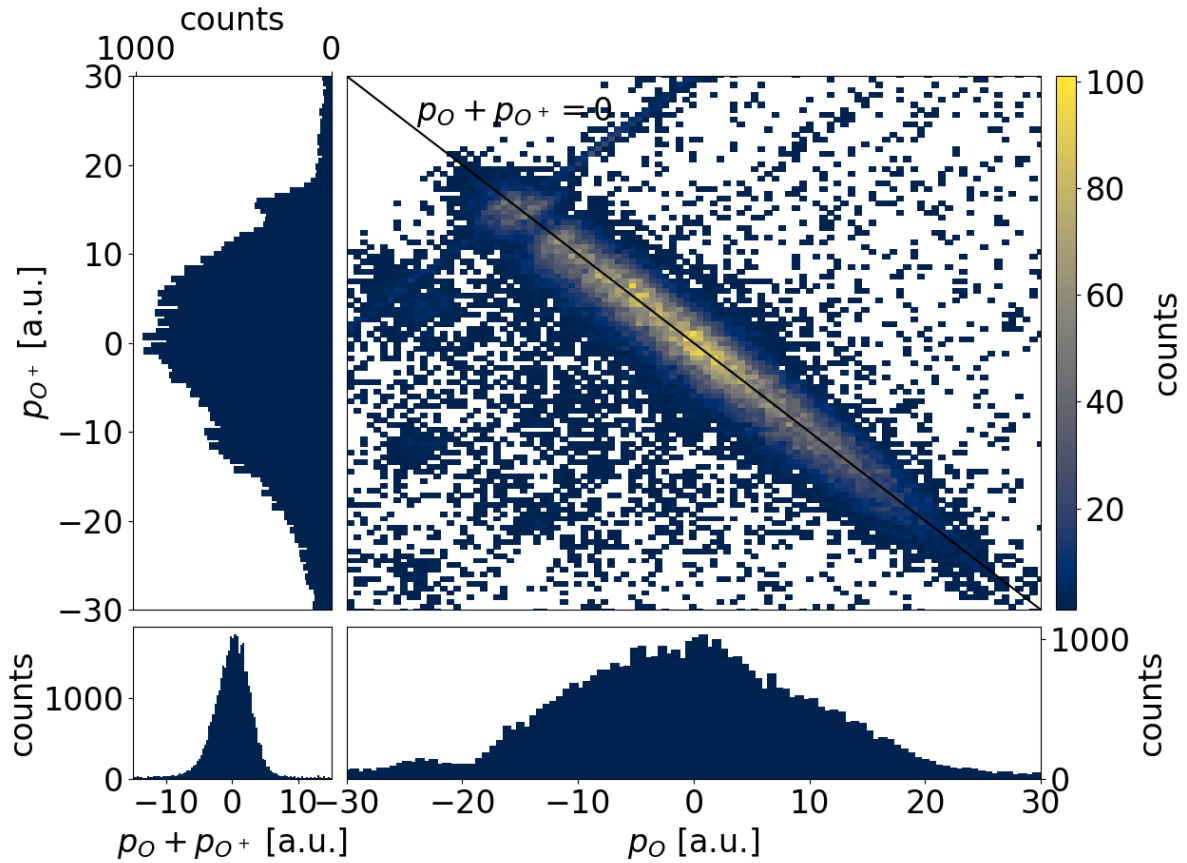

Figure 6.17: Longitudinal reaction momentum of ion/ion detector coincidences in the center-of-mass frame. Reconstructed from the tof data in figure 6.14 together with projections on both momentum axes. The coincidence line extends along the axis of zero sum momentum $p_O + p_{O^+} = 0$ as expected from momentum conservation. The distribution of sum momenta $p_O + p_{O^+}$, calculated for each coincident pair, is presented in the bottom left. As discussed in section 3.4.3, the width of this distribution ($\sigma = 2.5\,$a.u.) yields information on the spread of initial target momenta and can be regarded as experimental resolution.

The same momentum reconstruction can be performed for the coincident event pairs on ion and neutral detector. Figure 6.18 presents the resulting coincidence line. The momentum distributions of the single products agree with the ones obtained in figure 6.17. The sum distribution, i.e. the distribution of the initial molecular target momenta, exhibits a standard deviation of $\sigma \approx 1.6\,$a.u. and is thus more narrow. This is not expected from the estimation of uncertainties in section 3.4. One reason could be the fact that the different coincidence types, on ion/ion and ion/neutral detectors respectively, measure different cutouts from the full momentum distribution.

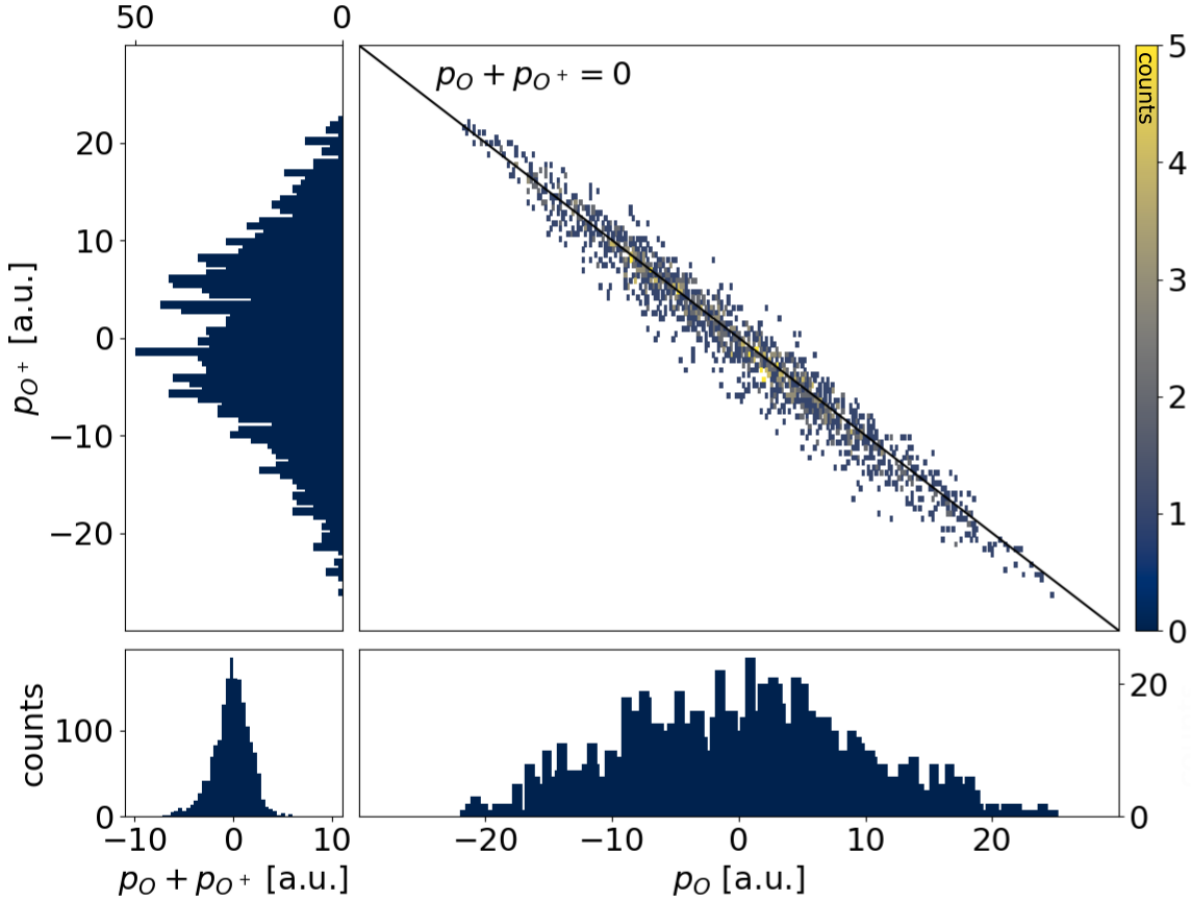

Figure 6.18: Longitudinal reaction momentum of ion/neutral detector coincidences in the center-of-mass frame. Reconstructed from the tof data in figure 6.15 together with projections on both momentum axes. The momentum sum distribution is with $\sigma = 1.6$ a.u. more narrow than in the case of ion/ion coincidences.

6.4.2 Positions, Transverse Momentum and Kinetic Energy Release

Photodissociation on Neutral Detector. While longitudinal momentum distributions can be reconstructed solely from the time-of-flight, the reconstruction of transverse momenta requires detector hit positions in addition. As starting point for an interpretation of the observed positional structures, we compare the neutral beam background, which has been previously presented in figure 6.7, to the photodissociation signal. Figure 6.19 illustrates how we distinguish between this signal and the background events: We select two equally-sized time-of-flight regions from the same measurement, one which contains the photodissociation signal and neutral background (left) and another which contains only background (right).

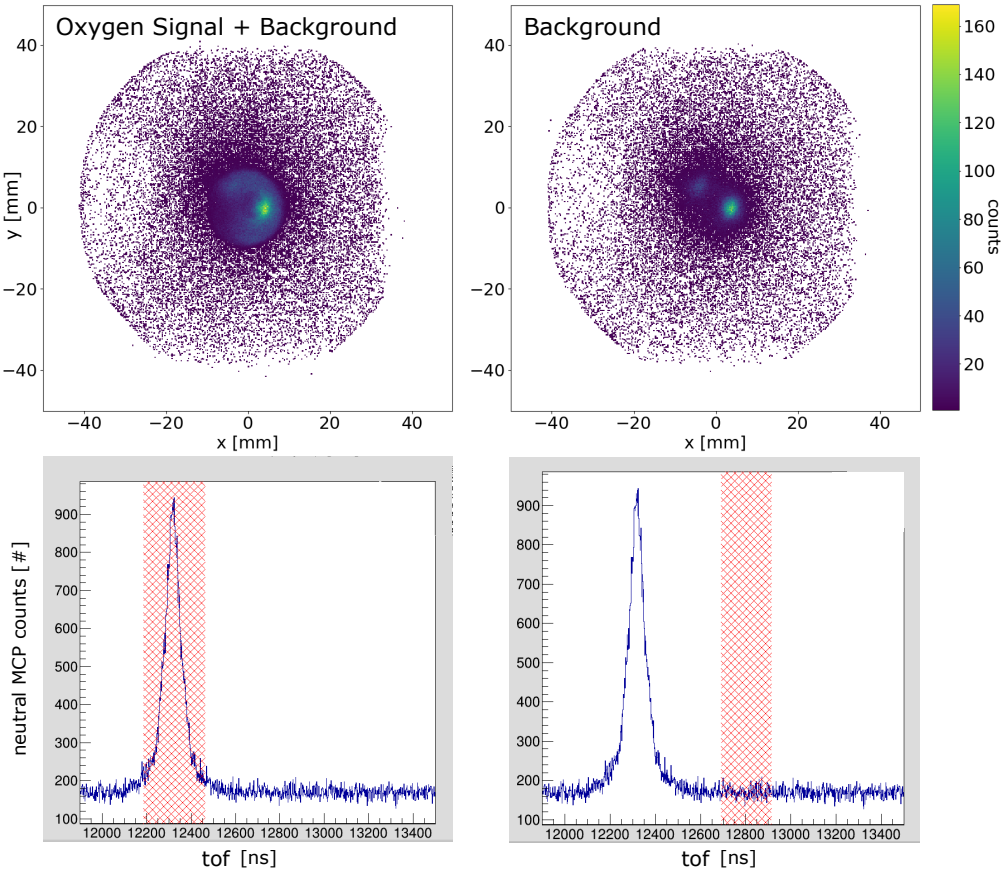

Figure 6.19: Positions on neutral detector (top) and tof-selection to distinguish between photodissociation signal and background (bottom). We select regions in the neutral MCP tof-spectrum: photodissociation signal (left) and background (right) and plot the position of the events in the selected regions. The photodissociation signal is radially restricted to a circle by the detector tubes. The background events stem from ions which neutralize during storage by capturing an electron from the residual gas (see section 5.2.3) and the structure of this position depends on the storage mode (see section 5.3.2). The colorcode expresses the number of accumulated counts per 2D-bin. The suppression of detector events on the edges is related to the use of hardware CFDs.

In the top of the same figure, the positions of the corresponding events are presented. An obvious difference is, that in the case of the signal on the left, a circular region of approx. 20 mm radius is "illuminated". This is a projection of the detector tube aperture onto the neutral detector. This aperture restricts the trajectories of products to the neutral detector. Thus, only a certain cutout of the full momentum distribution is detected. In figure 6.20 (left), we plot the background-subtracted signal, i.e. the difference of the position distributions in figure 6.19. The numbered features are interpreted as follows:

- (1) We observe a maximum at the same position as in the neutral background. These are dissociation products which originate from the dominating component of the stored beam. This supports our expectation from section 6.3.1 that the laser overlaps with this component.
- (2) The circular region is less filled on the left side. This fits to the interpretation that the reaction products mainly emerge from the dominating beam component, and their whole distribution is decentered to the right.
- (3) There is a smaller circular region in which less counts are observed. This feature is not visible in the neutral background. The cause of it is not clear, a possibility is the deflection of neutral products on the inside of the detector tube.

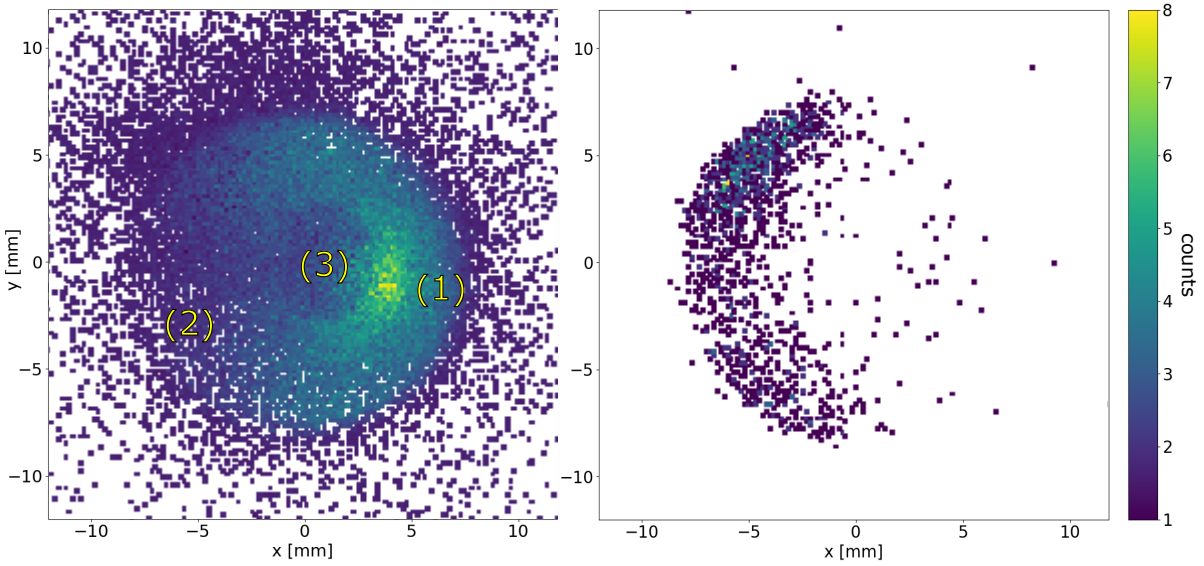

Figure 6.20: (left) Neutral detector positions of all oxygen atoms from photodissociation, background-subtracted. (right) Neutral detector positions of oxygen atoms which are coincident with an oxygen ion on the ion detector.

Coincidence Position on Neutral Detector. The position of oxygen atoms on the neutral detector which have been detected in coincidence with an O^+ on the ion detector are plotted in figure 6.20 (right). The positions are restricted to a circle due to the detector tube aperture. The events are mainly detected on the left of the observable region. This fits the interpretation that the photodissociation is mainly induced at the position of the dominating beam component (see figure 6.7). This position is on the right of the REMI axis. As shown by our simulation in figure 6.16, the ion/neutral coincidence is more probable to be observed when it is induced off-axis. As indicated in the same figure, the neutral products are expected to propagate on a tilted trajectory.

Positions on Ion Detector. In figure 6.21 (left), we present the position of the background-subtracted photodissociation signal on the ion detector. The products are detected only at small radii around the central gap. This is because in this specific case of O_2^+ photodissociation, the products gain only relatively small energy as estimated from the possible PEC transitions in section 6.1.3. The majority of the products hits the dead region around the central gap. Additionally, close to the central gap there are non-linear distortions of the position detection. On the right of the same figure, we show the position of products which have been detected in coincidence with an atom on the neutral detector. Many events are located along the edges of the delaylines which obviously is a technical mis-detection instead of an actual position. In this experiment, the delayline signals of the ion detector exhibited a low signal-to-noise ratio and many electronic reflections where observed. In conclusion, the event positions on the ion detector can not be used for reconstruction of transverse momentum.

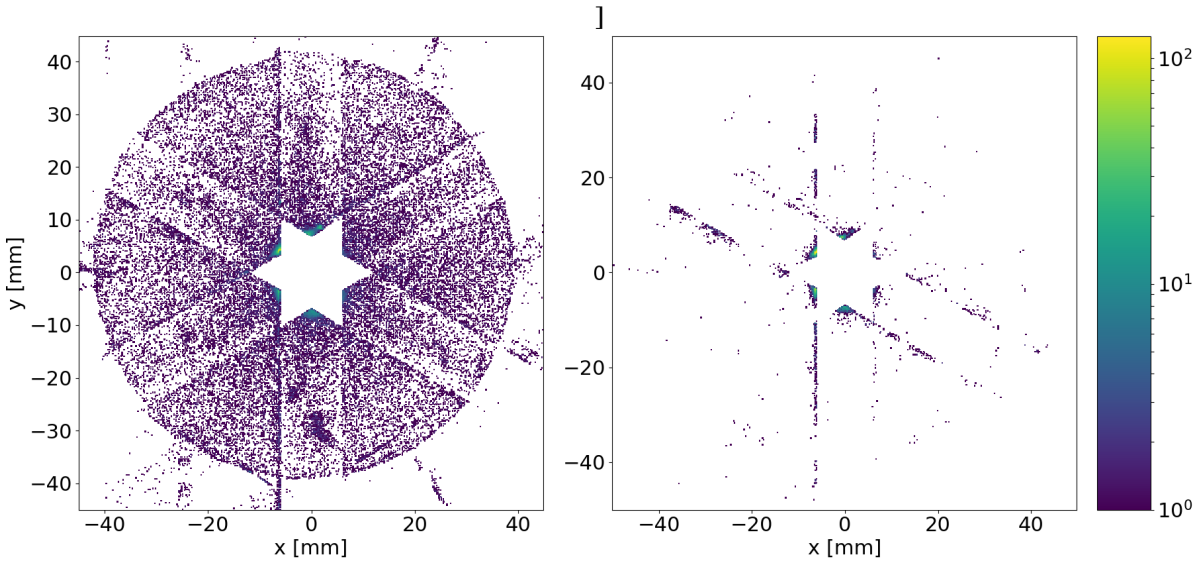

Figure 6.21: (left) Rear detector positions of all oxygen products from photodissociation, background-subtracted. (right) Rear detector positions of oxygen ions which are coincident with an oxygen atom on the neutral detector.

In this specific case, the acceptance for ions can be increased by decelerating them with the REMI spectrometer voltage. Another possibility is to store ions with less kinetic energy. We increased the radius at which oxygen ions are observed by a combination of both: E_{kin} has been decreased from 2500 eV to 1000 eV and V_{REMI} has been increased from 200 V to 400 V. The resulting detector picture of the photodissociation signal is shown in figure 6.22. The ions are distributed up to a radial distance of approx. 15 mm to the trap axis. This experiment has to be repeated since no neutrals where detected and more statistics have to be acquired.

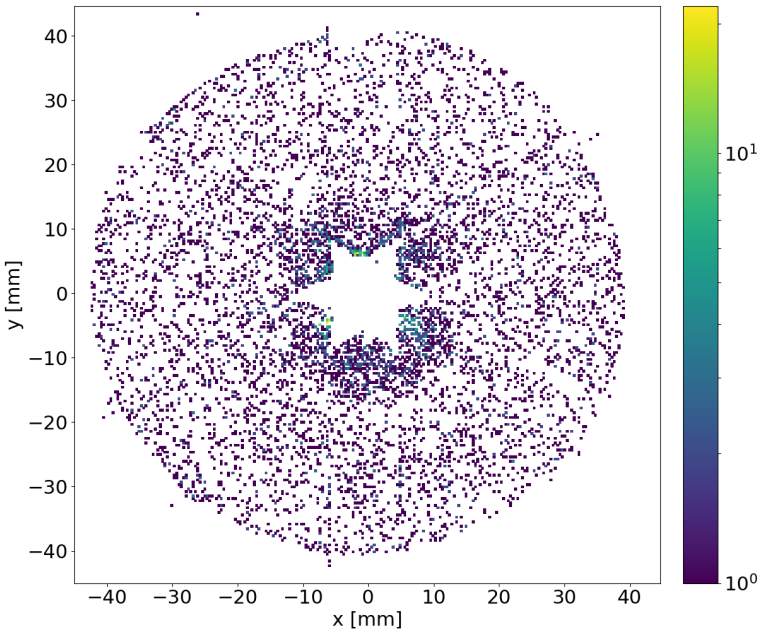

Figure 6.22: Background-subtracted position distribution of O^+ products on the ion detector. By reduction of the ion kinetic energy and stronger retardation by the REMI spectrometer voltage, a higher ion acceptance has been achieved.

Kinetic Energy Release. The transverse momenta of the coincident events measured on the neutral detector (figure 6.20, right) can be reconstructed. The reaction is assumed to take place at the projected position of the dominating beam component $(x_0, y_0, z_0) = (4.7\,\text{mm}, -0.7\,\text{mm}, 0\,\text{mm})$. As described in section 3.4.2, the total transverse product momenta can be calculated by

$$\begin{bmatrix} p_x \\ p_y \end{bmatrix} = \frac{m}{t} \begin{bmatrix} x - x_0 \\ y - y_0 \end{bmatrix} \tag{6.12}$$

which includes reaction momentum and initial target momentum. We measure only a cut-out of the full momentum distribution. However, for the dissociation of diatomic molecules, the KER is expected to be isotropic and can be calculated from this momentum cut-out like

$$KER = 2E_{kin} = 2 \cdot \frac{p_x^2 + p_y^2 + p_z^2}{2m} \tag{6.13}$$

The KER distribution is presented in figure 6.23. As estimated from the O_2^+ PECs in section 6.1.2, the photodissociation results in relatively small KER values.

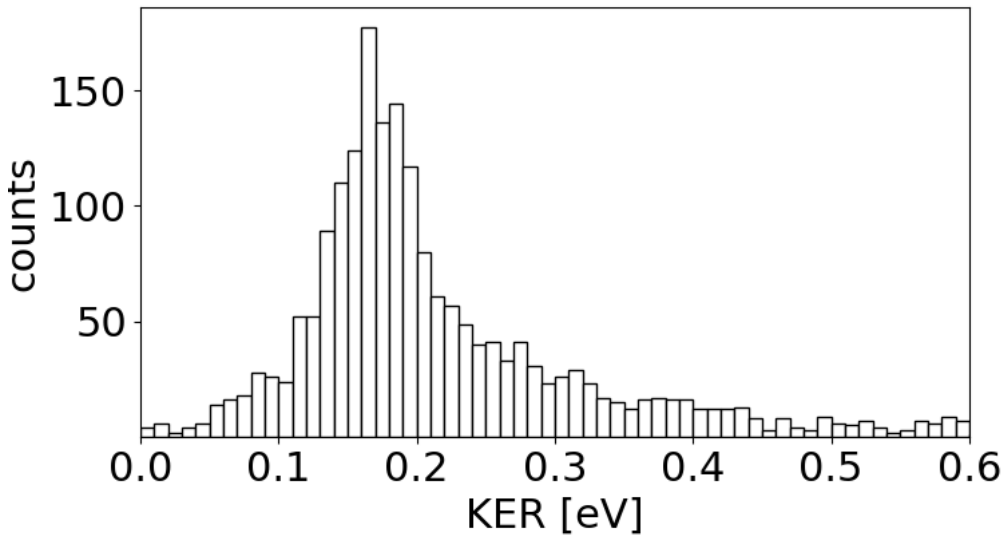

Figure 6.23: Kinetic energy release of O_2^+ photodissociation calculated from the reconstructed momenta of coincident oxygen atoms on the neutral detector.

CHAPTER 7

PHOTODISSOCIATION OF THE METHANE CATION

In this chapter, we present the photodissociation of CH_4^+ as prototypical hydrocarbon ion. We observe the dissociation in CH_3^+ and H which has been previously reported in [79] and a low intensity signal of CH_2^+ products. Contrary to previous experiments, we are able to detect dissociation products in coincidence. The ion production and storage is documented in section 7.1. Time-of-flight measurements for different spectrometer voltages and the comparison to ion optics simulations allow to identify the reaction products as presented in section 7.2. The first experiment with both REMI detectors running resulted in the unexpected observation of "delayed products". These have been identified to perform additional revolutions in the EIBT before being detected. In section 7.3, we show that the momenta of these products can be reconstruced with the help of ion optics simulations.

7.1 CH_4^+ Production and Storage

Ion mass spectrum. The production of CH_4^+-ions by electron impact ionization was performed with similar source parameters as for O_2^+, listed in table 7.1. A slightly higher heating current and source pressure was necessary to obtain the same output current. Since CH_4 is more complex than the diatomic O_2, more ionic species can emerge in the source. To identify the species, we performed the same tof-mass spectrometry as described in 6.2.1: We generated a short ion bunch of 1 µs temporal length and measured the tof of the emitted species on the neutral detector. Figure 7.1 shows the comparison with a NIST reference spectrum for electron impact ionization of methane. We produce mainly mass 16 u (CH_4^+), followed by slightly less mass 15 u (CH_3^+). Smaller fragments with mass 12 u (C^+), 13 u (CH^+) and 14 u (CH_2^+) and the isotope with mass 17 u ($^{13}CH_4^+$) are detected with low intensities as well.

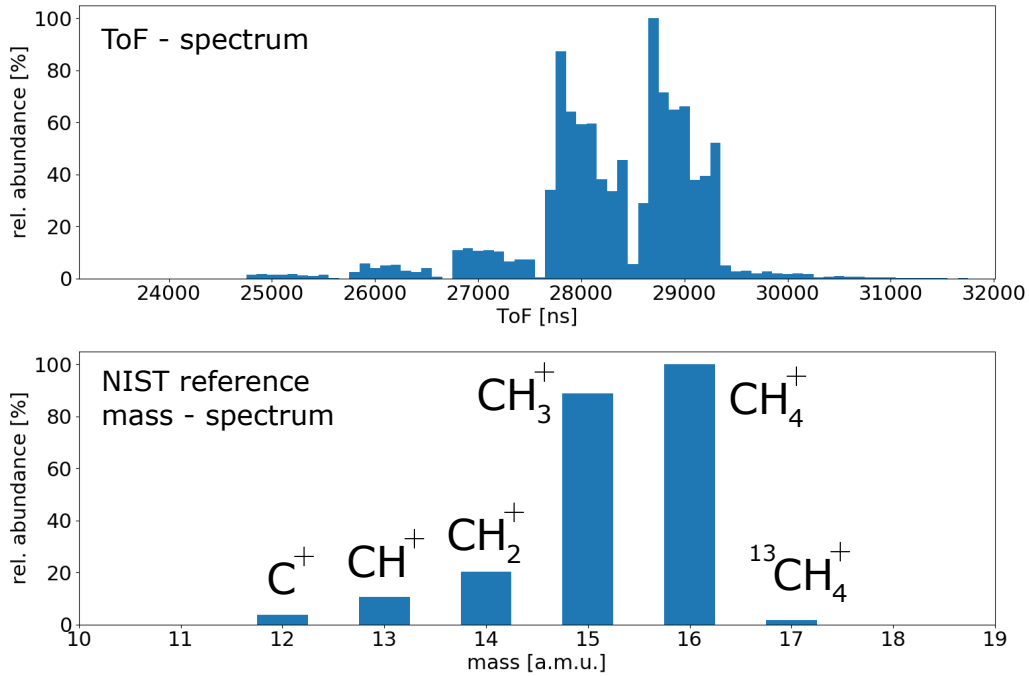

Figure 7.1: (top) Tof - spectrum of Methane pulse with 1μs length, recorded by the neutral detector behind the EIBT. (bottom) NIST reference spectrum for electron impact ionization of Methane [80].

Source Parameters		Output Current [nA]		Ion Properties	
heating voltage	0.35 arb.u.	after source	100	bunch length	20 µs
emission current	1 arb.u.	after trap	10	ion energy	2500 eV
extraction voltage	100 V			rev. period	23.86 µs
source pressure	10^{-5} mbar			rev. frequency	41.9 kHz

Table 7.1: Typical source parameters for CH_4^+ ion production, output currents and ion properties. Note: The controller of the electron impact ion source allows to adjust heating voltage and emission current but does not display meaningful values of these quantities. Instead, it provides a reference value in arbitrary units which we list here.

Ion Storage. Produced with 2500 eV kinetic energy, they revolved with a period of 23.86 µs in the trap. For the photodissociation experiment, we generated a longer bunch with $t_{bunch} = 20\,\mu s$ to fill the trap and increase the photodissociation count rate. As the Fourier-spectrum in figure 7.2 shows, there are two frequency components in the storage signal. Since we did not mass select the injected ion bunch, these components most probably stem from the ion species produced with highest intensity: CH_4^+ and CH_3^+. This is supported by the fact that the ratio of revolution frequencies corresponds to the ion's mass ratio like $\frac{f_{CH_4^+}}{f_{CH3^+}} = \sqrt{\frac{m_{CH_3^+}}{m_{CH_4^+}}} \approx 0.968$. Since both ions are stored, we possibly detect products from both of them when inducing a reaction with the IR-laser. However, these products can be distinguished by their time-of-flight. From the velocity of the stored ions, one can estimate that two reaction products which stem from CH_4^+ and CH_3^+ respectively, differ in tof to the ion detector by around 60 ns. The trap voltage configuration is listed in table 9.2 as "config 3.

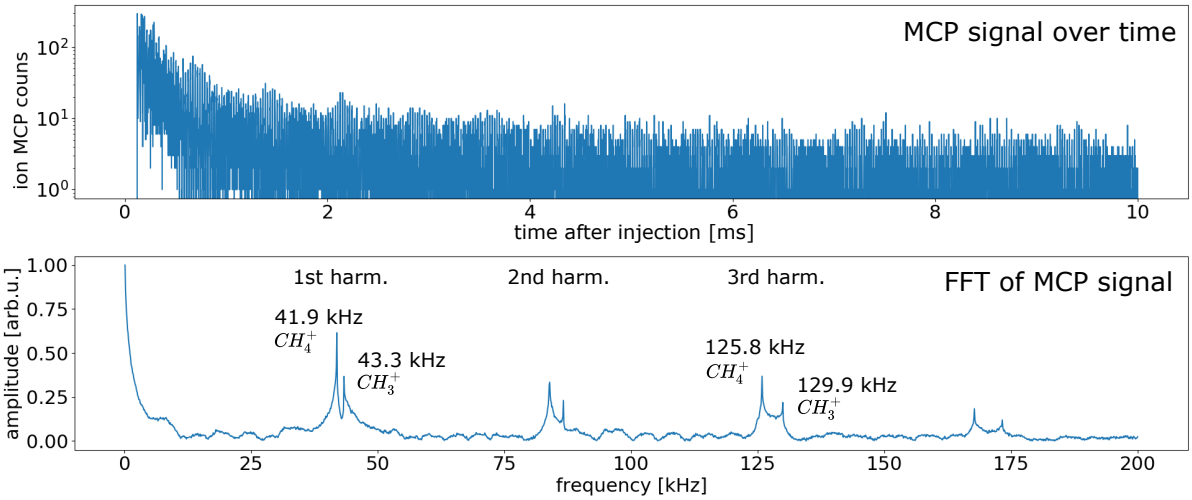

Figure 7.2: (top) Ion storage monitored by the ion MCP. The storage cycle is repeated every 10 ms. (bottom) FFT of MCP storage signal. We observe two frequency components, corresponding to CH_4^+ ad CH_3^+.

7.2 Identification of Reaction Products

The photodissociation of CH_4^+ can result in several reaction products. In order to identify the detected species, we performed the experiment with four different REMI spectrometer voltages: 10 V, 100 V, 200 V and 300 V. For positively charged products moving towards the ion detector, these voltages act decelerating. For neutral products, the expected tof to the detector is around 1930 ns, estimated from the initial target energy of 2500 eV. The nominal laser parameters were the same as for the O_2^+ experiment, listed in table 6.2. As in the case of O_2^+, this experiment has been performed with only the REMI ion detector and the neutral detector. For the REMI electron detector, the coupling box was still in production. Figure 7.3 presents the MCP signals on the ion detector. The tof-spectrum relative to the laser pulses exhibits four peaks, labeled product 1 to 4.

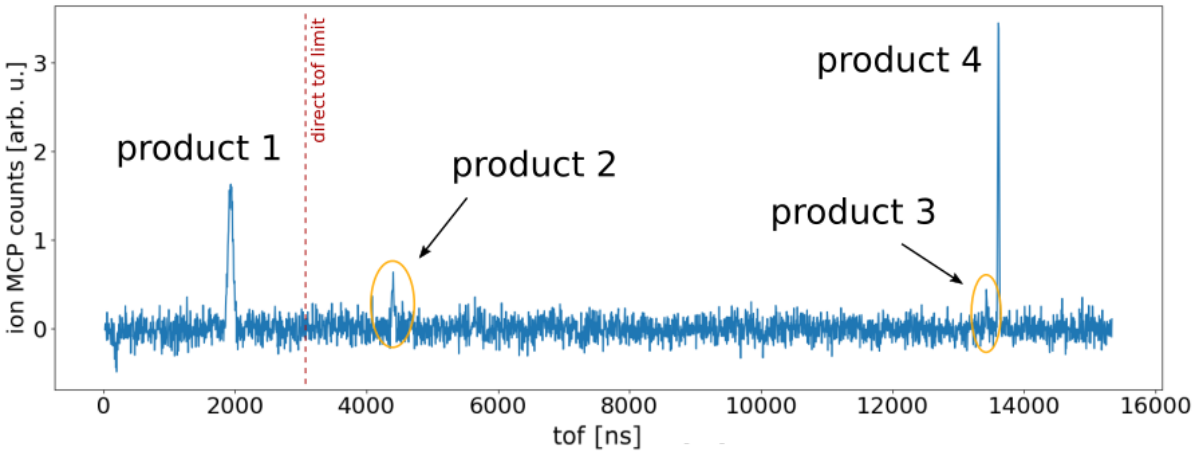

Figure 7.3: Tof on rear MCP relative to the preceding laser pulse. We observe four reaction products, two of which are highlighted in yellow for convenience. The red dashed line indicates the maximum tof of a direct trajectory to the detector to be approx. 3050 ns. This spectrum has been generated as described in 9.2. The time until the next laser pulse was ≈ 21 ns but the upper part of the spectrum has been cut since no products are observed there.

Neutral Reaction Product. A closer view on the first peak is presented in Figure 7.4. The tof corresponds to the expected value for a neutral particle. Further, the peak position is independent of the applied REMI voltage within the measurement uncertainties. As estimated from equation 6.8, even for the product with highest possible mass, and thus for the least sensitive one, the tof retardation from 10 V to 200 V would be around 60 ns. In conclusion, the first peak results from a neutral reaction product. From this information however, we can not identify the product's mass. Since all products move with the same mean velocity after the reaction, the observed signal could be a conflation of multiple neutral species.

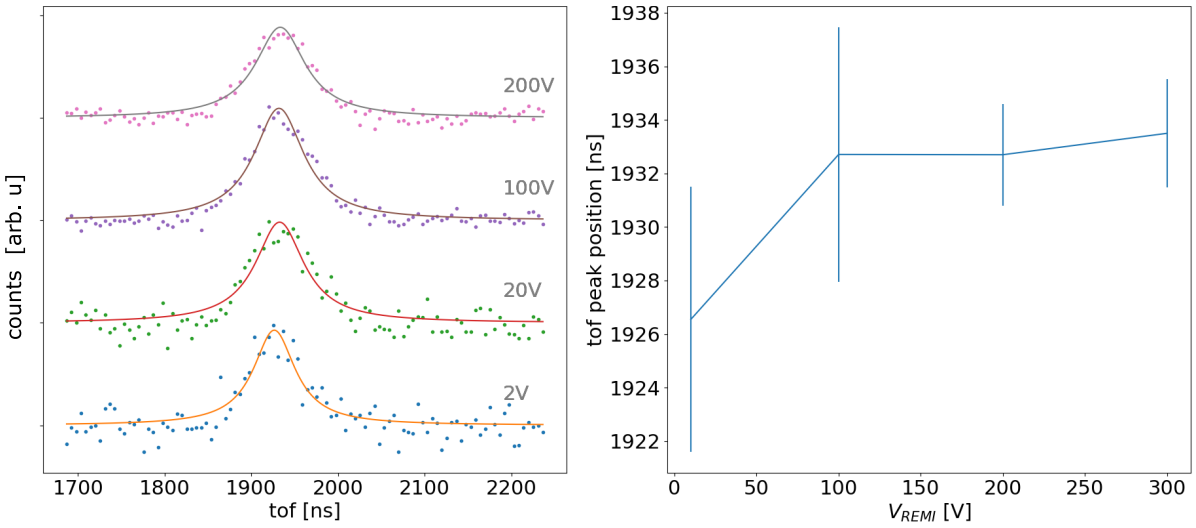

Figure 7.4: (left) Time-of-flight peak of reaction product 1 for different REMI voltages. The measurements have been shifted along the y-axis for better illustration. (right) Peak position on REMI voltage. Within the uncertainties, the position is independent of the applied voltage. In conclusion, a neutral product is observed.

Delayed Products. The remaining signals stem from fragments following a different trajectory. Their tofs exceed the duration of a direct trajectory from reaction region to the detector. This can not be explained by a light-weight product which is retarded strongly by the REMI voltage. Even for the smallest product and highest voltage, H^+ and 300 V, the maximum time for a direct trajectory to the detector is estimated to be around 3050 ns which we indicated by the red dashed line in figure 7.3. Figure 7.5 shows how the tof of the strongest signal, product 4, depends on the REMI voltage. With increasing voltage, the product arrives earlier. This is not expected since the REMI voltage decelerates positively charged products. The excess tof of product 4 is similar to a half-revolution period $T/2 \approx 11.93\,\mu s$ in the EIBT. To investigate possible trajectories to the detector, we performed ion optics simulations in SIMION. Figure 7.6 presents a trajectory which can explain the experimental signals: While being stored, target ions cross the interaction region in both directions. As illustrated in green, the neutral product originates from a molecule moving towards the ion detector. In red we show the case of a molecule moving away from the ion detector. A dissociation product of this molecule, emitted under a small angle to the trap axis, can pass the detector tube and leave the REMI. If it is charged, it can be reflected by the trap mirror, enter the REMI again and impinge upon the ion detector. During this half-turn in the left part of the EIBT, it crosses the region of negative REMI voltage two times. Thus, when increasing this voltage, the duration of the half-turn reduces which explains the shift to shorter arrival times. Further, it is noteworthy that the delayed product signal is sharper then the direct one. During steady motion, particle ensembles disperse and the resulting tof distributions broaden. Here, the mirror has a time-focusing effect similar to a mass reflectron [81]. This reduces the effect of momentum

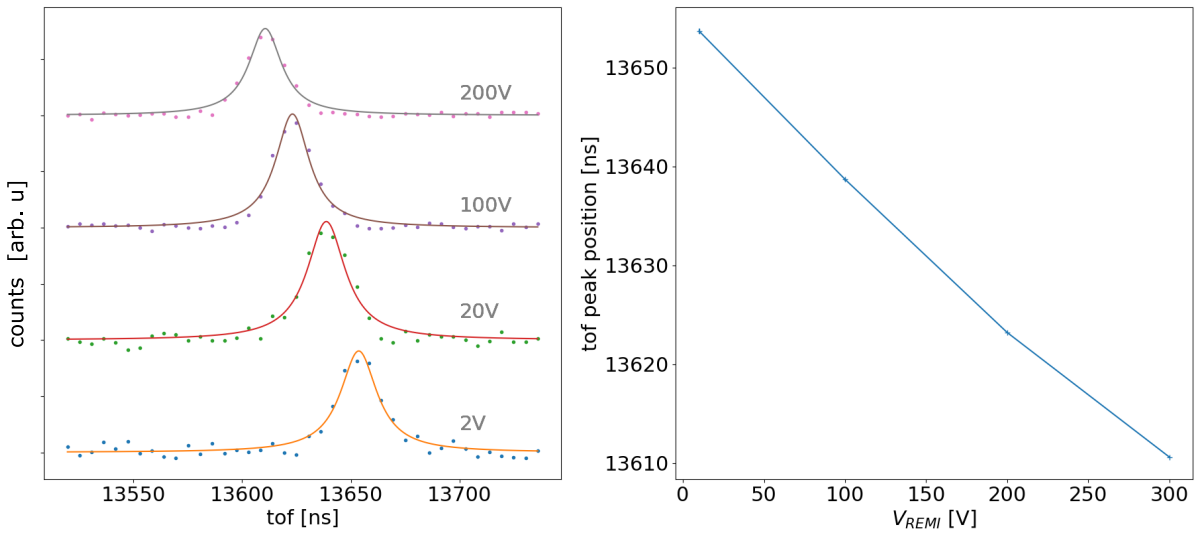

Figure 7.5: (left) Time-of-flight of delayed product (product 4) for different REMI spectrometer voltages. (right) The peak position shifts to shorter time of flights with increasing voltage.

spread in an ensemble of ions with the same charge-to-mass ratio and thus increases the ability to distinguish ion species. This is an interesting feature of our setup, which however decreases the momentum resolution of the observed species. Thus, it will be of use only in special cases rather then usual REMI experiments.

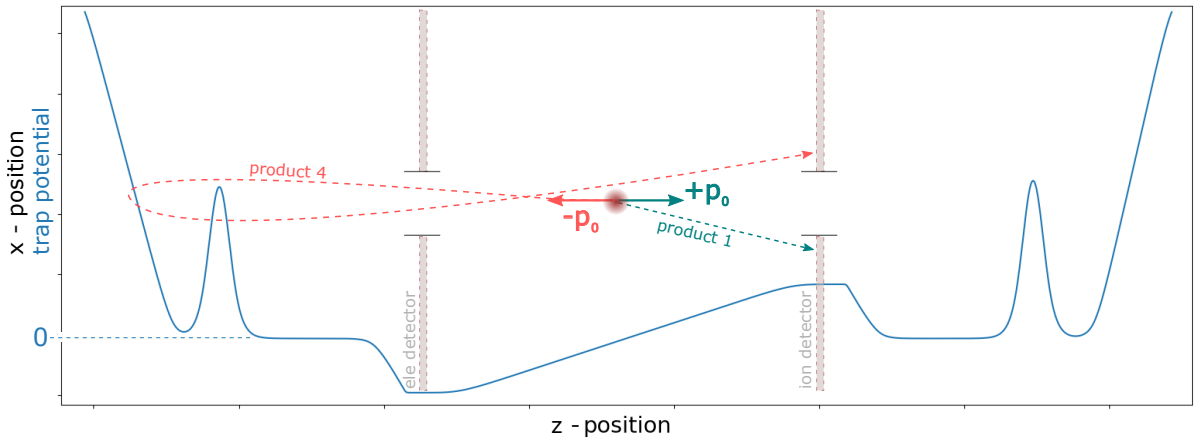

Figure 7.6: (Green) The neutral, "direct" product 1 originates from a molecule moving towards the ion detector, i.e. in z-direction, and is emitted under a sufficiently large angle. (Red) The other observed products perform an extra revolution in the EIBT. The tof of product 4 can be explained by the illustrated trajectory: Originating from a molecule which initially moves in -z direction, the product leaves the REMI through the detector tube, is reflected by the trap mirror and impinges upon the ion detector. During this half-turn it crosses the region of negative REMI voltage two times. Thus, the half-turn duration gets shorter with increasing REMI voltage.

Product Identification by tof-Simulation. The observed products can originate from CH_4^+ as well as CH_3^+ which are both stored with $E_{kin} = 2500\,\text{eV}$ as shown in section 7.1. To identify the species, we simulated trajectories for all possible fragments in SIMION. A close view on product 2 (left) and product 4 (right), depending on the applied REMI voltage is shown in figure 7.7. In each case, only the simulation of a specific fragment can reproduce the observed time-of-flights and the observed voltage dependency: A CH_3^+, originating from CH_4^+ and thus moving with the respective mean kinetic energy of $E_{kin} = 2343.75\,\text{eV}$. In the case of product 4, it performs an additional half-turn and in the case of product 2 even an additional full-turn in the EIBT. The simulated time-of-flights of product 2, indicated by vertical, dashed lines, are slightly too small. However, none of the other possible products is detected in this tof-region in our simulation. Product 2 did not originate from a reaction at $t = 0$ but from the preceding laser shot at $t \approx -20\,953\,\text{ns}$. Thus, the total tof of product 2 (e.g. for 200V) is not 4406 ns, as plotted in figure 7.7 but $4406\,\text{ns} + 20\,953\,\text{ns} = 25\,359\,\text{ns}$. Product 3 is not shown in the voltage dependent plot of figure 7.7 since it is only observed at 200V. For the other voltages, not enough statistics have been acquired. The time-of-flight of product 3 has been reproduced by a CH_2^+ fragment, performing an additional half-turn.

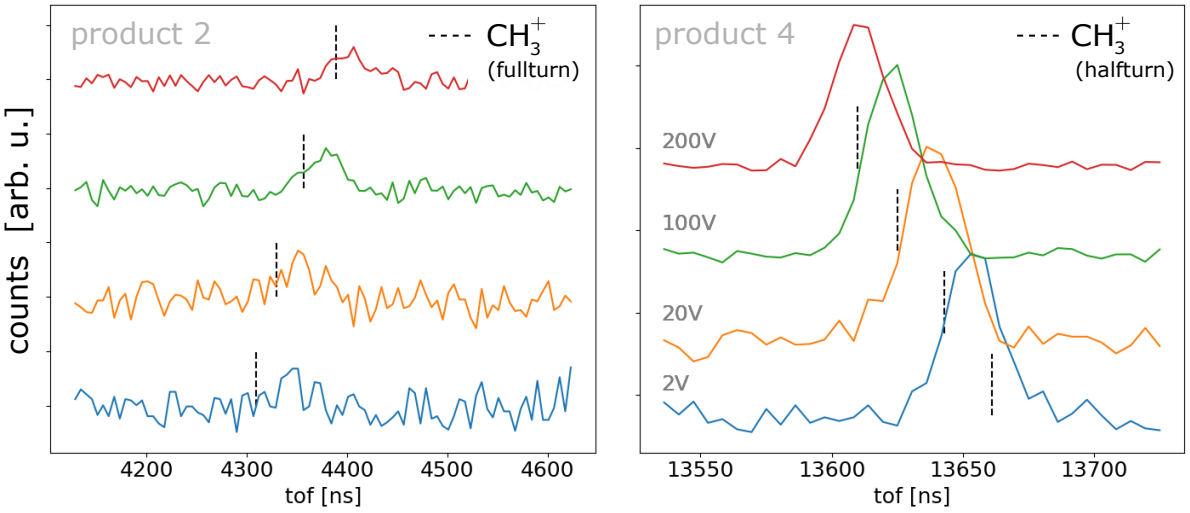

Figure 7.7: Observed time-of-flights of delayed products for different REMI voltages. The simulated tofs which reproduce the observation the best are indicated by vertical, dashed lines. (left) Product 2, reproduced by the simulation of CH_3^+ performing an additional full-turn after photodissociation. (right) Product 4, reproduced by the simulation of CH_3^+ performing an additional half-turn after photodissociation.

As presented in figure 7.8, all charged products could be identified by ion optics simulations. As mentioned before, the neutral product can be a conflation of multiple species. In the next section, we present the coincident detection of methane fragments which can allow the identification of the neutral product mass.

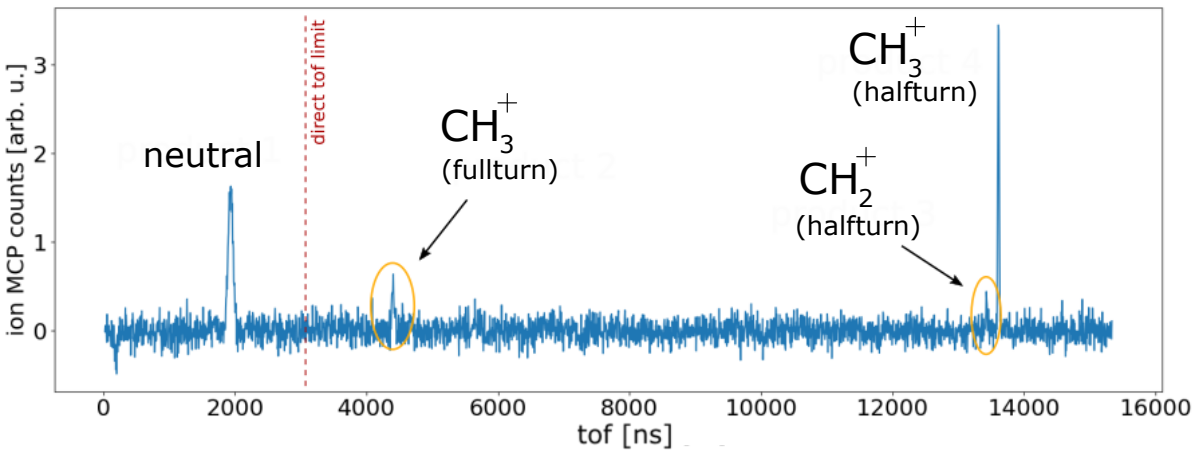

Figure 7.8: Tof spectrum of methane photodissociation. The unknown, charged products presented in figure 7.3 have been identified. All of them are detected at delayed tofs since they perform additional motions in the EIBT. Since product 2, which has been identified as CH_3^+, performs another full-turn in the EIBT, it arrives even after the next laser pulse. Thus, it's tof values are measured shifted by the laser repetion time of 20953 ns and the actual values exceed this tof spectrum.

7.3 Coincident Detection and Delayed Product Momentum

We repeated the CH_4^+ photodissociation experiment, this time with all three detectors. It was not reasonable to set up a REMI detector for electron detection since no bake-out has been conducted so far. At a pressure around 10^{-9} mbar, the electrons from residual gas ionization would deplete the data acquisition system by overflowing the ADC buffers and so prevent the other detectors from efficiently recording ionic and neutral products. Instead, we set up both REMI detectors for ion detection. This can bare several advantages: Target molecules and reaction products can pass through the interaction region in both directions. In this scheme, a higher count rate can be achieved by detecting the products on both sides of the reaction. Further, the combined information of both detectors yields information on the reaction position (x_0, y_0, z_0).

Since the delayed products perform additional turns in the EIBT, their observance is expected to be sensitive on the trap voltage configuration. By slightly changing the voltages compared to the previous experiment in section 7.2, we managed to detect signals on both detectors, as shown in figure 7.9: The neutral product 1 impinges on the rear detector after approx. 1965 ns and a CH_3^+ ion is detected after approx. 13690 ns on the front detector. The other two delayed products have not been observed in this configuration. No events where detected on the neutral detector. Since the products are detected on opposite detectors, they can now originate from the same target molecule. A coincidence analysis as described in section 6.3.3 yields approx. 2450 coincident event pairs. The corresponding coincidence line is plotted in figure 7.10. The fact that

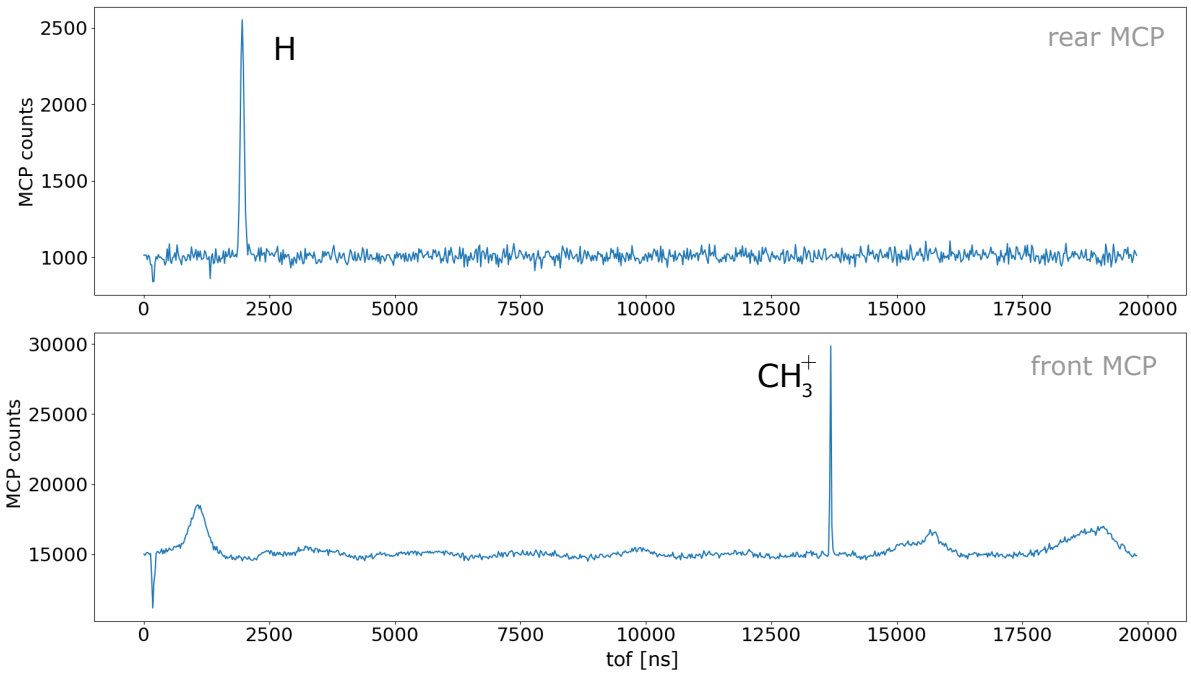

Figure 7.9: (top) REMI rear detector. The neutral product travels ≈ 1965 ns on a direct trajectory to the detector. (bottom) REMI front detector. After a half-turn in the EIBT, the CH_3^+ product impinges the detector after ≈ 13 690 ns. The additional structure in the tof-spectrum originates from residual gas ions which are accelerated towards the detector by the REMI voltage.

this clear correlation is visible shows that we observe a dissociation channel through which the molecule fragments in only two products. In conclusion, the neutral product 1, as dissociation partner of CH_3^+, is a hydrogen atom. The momentum distributions of the coincident products are shown in figure 7.11. In case of the neutral H, the longitudinal momentum can be calculated as described in section 3.4.2. This is not possible for CH_3^+ due to the more complicated trajectory illustrated in figure 7.6. To reconstruct the longitudinal momentum of this product, we simulated this trajectory in SIMION and extracted a numerical relation between product momentum and time-of-flight. By applying this relation to the measured tof, we obtained the CH_3^+ longitudinal momentum distribution. The feasibility of this approach is supported by the narrow momentum sum distribution $p_H + p_{CH_3^+}$ with a standard deviation of $\sigma \approx 0.6$ a.u.. This initial momentum uncertainty is lower then for O_2+ which is expected from the lower mass of the CH_4^+.

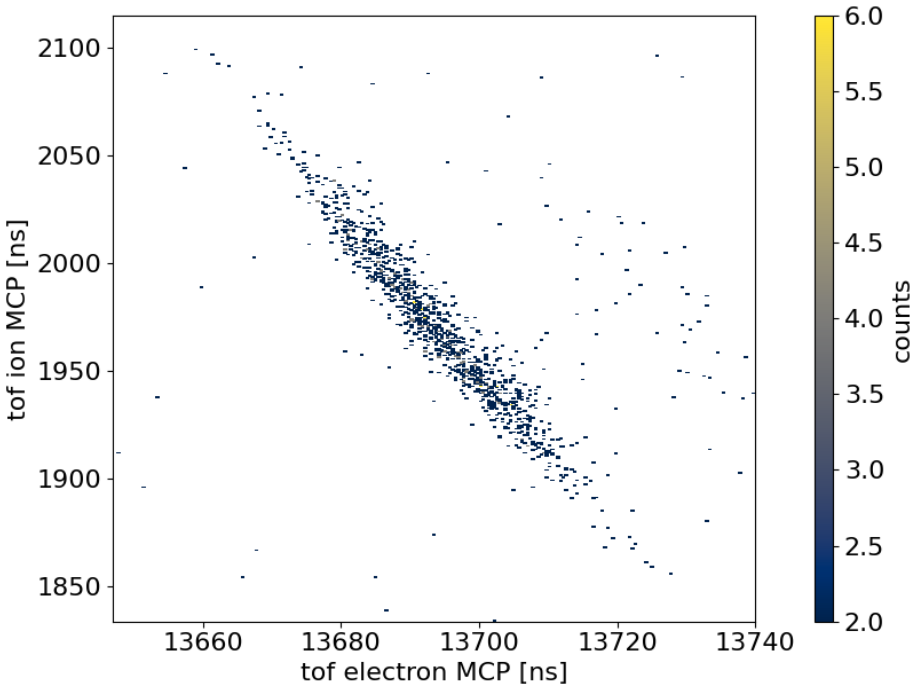

Figure 7.10: Time-of-flight coincidence histogram for the direct H and the CH_3^+ delayed product.

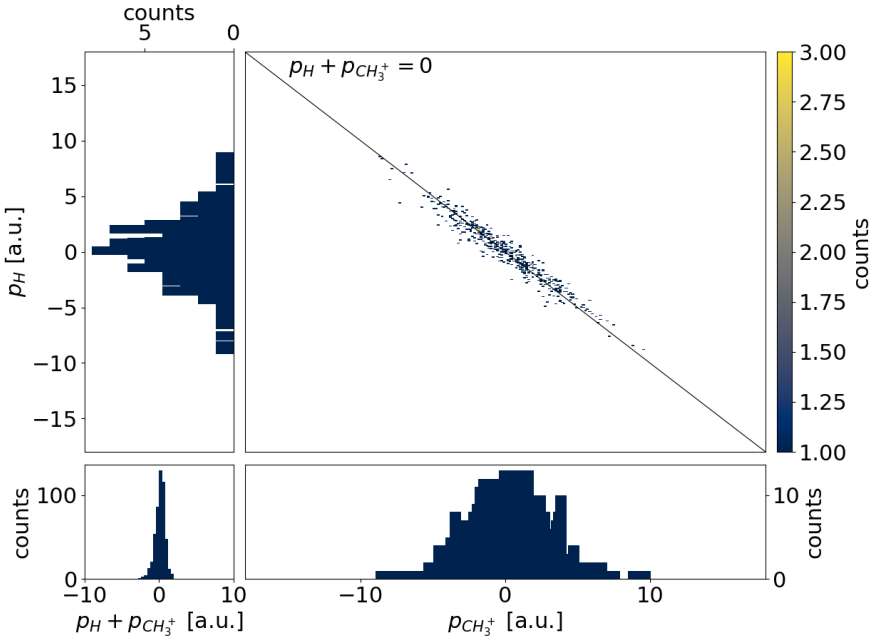

Figure 7.11: Reconstructed longitudinal momentum of coincident dissociation products.

CHAPTER 8

SUMMARY

Molecular ions are abundant in the universe from interstellar clouds to atmospheric environments of planets. They play key roles in chemical reactions which result in the emergence of complex and biologically relevant molecules. A better understanding of these reactions can be obtained by investigating the quantum dynamics of molecular ions. In the condensed phase of matter, bulk interactions significantly influence molecular dynamics and isolated molecules are no longer an appropriate model system. To incorporate the bulk influence but still maintain advantages of gas-phase experiments, molecular clusters can be investigated.

In this thesis, a novel experimental apparatus for quantum dynamics experiments on molecular ions and charged clusters has been developed from scratch to first experiments. The TrapREMI allows to store fast target beams in an electrostatic ion beam trap (EIBT). During storage, the targets are brought to reaction with a projectile beam, e.g. a laser pulse, and the resulting reaction products are detected in a Reaction Microscope (REMI). This approach combines advantages of two techniques. An EIBT offers advanced possibilities for target preparation, e.g. mass-independent ion storage, momentum spread reduction by autoresonance cooling and recycling of species which are difficult to prepare. A REMI is a versatile momentum spectrometer for electrons and ions. It allows to measure multiple reaction products in coincidence and to reconstruct their 3D momentum vectors. In usual REMI experiments, neutral products can not be detected due to low kinetic energies. In experiments involving EIBTs, no coincident ion and electron spectroscopy is performed. The unique combination of these techniques enables both, the detection of neutral, ionic and electronic products in coincidence and hence to obtain kinematically complete information on the molecular reaction process.

We chose a longitudinal configuration to integrate the REMI in the EIBT. This allows to store the ions without being deflected by the REMI extraction fields. The combination of these techniques is technically challenging because ions are stored through central gaps in the detectors which restricts the trap phase space. Additionally, the central gaps reduce the REMI acceptance. During the first phase of this thesis, the TrapREMI design was developed by employing ion optics simulations. Thereafter, the components fabricated by the MPIK precision mechanics workshop were assembled. Procedures for ion production and injection as well as data acquisition schemes have been developed. By these means, the storage capabilities and ion bunch dynamics in the TrapREMI have been characterized. Without bakeout of the vacuum chambers, we showed to store an ion number on the order of 10^3 with beam lifetimes over 1 s which is sufficient for many experiments. These values can be improved by better vacuum conditions and ion sources with lower emittance. We are able to control the ion beam profile to ensure sufficient momentum resolution and identified different modes of ion bunch dynamics which either result in fast dispersion or self-synchronization of the ion bunch. The latter can enable a reduction of the ion's momentum spread for better experimental resolutions. In contrast to usual REMI experiments, the high kinetic ion storage energy allows to detect neutral products. However, it also imposes a lower limit on reaction momenta and energies which can be detected. Therefore, the TrapREMI design is best suited to investigate reactions with high kinetic energy release (KER) in the eV regime.

In the final phase, the TrapREMI has been connected to a femtosecond IR-laser system and first photodissociation experiments on stored molecular ions have been performed. The observed photodissociation of stored O_2^+ provides a proof-of-principle for coincident product detection of ions and neutrals in the TrapREMI. From the coincidences on ion and neutral detector, the kinetic energy release (KER) could be determined to be in the 100 meV regime. As prototypical hydrocarbon ion, we performed the same photodissociation experiment on CH_4^+. We observed a fragmentation channels which results in $CH_3^+ + H$ products. A signal of CH_2^+ has been observed as well, however without a corresponding dissociation partner. Additionally, delayed products where detected which perform additional revolutions in the EIBT. This is a feature similar to ion motion in reflectron mass-spectrometers and can be of use only in particular situations. In usual REMI experiments, it decreases the momentum resolution.

In future experiments, reactions with high KER will be investigated. One possibility is to induce a coulomb explosion of the stored molecule. This can be achieved by strong-field IR laser pulses or XUV radiation, both of which can be provided by our femtosecond laser laboratory. Examples are coulomb explosions of anthracene ($C_{14}H_{10}$) which has shown to result in a KER of up to 30 eV [82] and oxide clusters [83]. Coulomb explosion imaging can also be applied to investigate isomerization dynamics of molecules. An interesting but sophisticated experiment would be to

time-resolve the isomerization of acetylene (C_2H_2) . This molecule exhibits different geometric structures depending on the charge state. In the TrapREMI, we can store $C_2H_2^-$ and perform a pump-probe experiment in which a first laser pulse detaches the excess electron and starts a structural change in the molecule. After a controlled time delay, a second laser pulse induces a coulomb explosion to probe the momentary structure.

CHAPTER 9

TECHNICAL NOTES AND MANUAL INSTRUCTIONS

9.1 FlashCam ADC Mask

For the FlashCam data acquisition, we need to specify the ADC channels on which signals should be recorded. This is done in form of an ADC mask in the hexadecimal system. Here, we present the example of ADC mask used for the photodissociation experiments in chapter 6 and 7. Table 9.1 lists the available ADC channels in the first row, numbered from 1 to 24. The seconds row shows the binary ADC mask. Each channel which should be recorded is activated by the number 1. Each channel which should be inactive is assigned a 0. The third row lists which input signal is recorded by the respective channel. In ADC channel 1 for example, we record "T0". This is the TTL trigger which starts the injection and defines time zero. From channel 5 to 23, we record the detectors with MCP and delayline signals. In channel 24, the laser timing from the photodiode is recorded. Each active ADC channel is assigned to a channel in Go4. This assignment is listed in row 4. The Go4 channel numbering is automatically generated. It starts at the first active channel with 0 and then counts upwards.

To set the ADC mask in the DAQ software, the binary mask depicted here has to be converted to hexadecimal form. In this case, the corresponding mask is FFFFF1.

ADC channel	1	2	3	4	5	6	7	8	9	10	11	12	13	14	15	16	17	18	19	20	21	22	23	24
ADC Mask	1	0	0	0	1	1	1	1	1	1	1	1	1	1	1	1	1	1	1	1	1	1	1	1
input signal	T0				x_1	x_2	y_1	y_2	MCP	x_1	x_2	y_1	y_2	z_1	z_2	MCP	x_1	x_2	y_1	y_2	z_1	z_2	MCP	t_L
Go4 channel number	0				1	2	3	4	5	6	7	8	9	10	11	12	13	14	15	16	17	18	19	20
	trigger				neutral detector						ion detector						electron detector							laser

Table 9.1: ADC Mask and channel configuration as used in the presented experiments.

9.2 Laser Gating & Correlation Spectrum

To uncover detector signals which are induced by the laser, we need to plot the relative timing between MCP events and the laser pulse which precedes them.

$$\Delta t = t_{MCP} - t_L \tag{9.1}$$

In a straighforward case, one would just record all laser and MCP events, iterate through them and calculate the time differences. A technical difficulty however is the high repetition rate of our laser system of at least approx. 47.725 kHz. The FlashCam DAQ can not record signals at this rate. Since the MCP count rate is much lower (usually on the order of $1000\,\mathrm{cts\,s^{-1}}$), we know that many laser pulses do not induce a reaction. Therefore, it is necessary to pre-select the laser pulses which are actually followed by an MCP event. However, when we detect the MCP event, the laser pulse has already passed usually some µs ago. This time difference is rather large for our high-precision DAQ and thus the laser pulse can not be retrieved from the buffer. A practicable solution is to not detect the pulse which has actually induced the reaction but the following one by gating it with the MCP event. Since the laser repetition time is stable on the order of 1 ns, the timing of the previous pulse can be calculated reliably enough. Figure 9.1 illustrates the electronic procedure as follows:

- The MCP pulses are processed by a CFD which generates a signal in NIM logic standard.
- The resulting NIM pulses are combined in a logical OR.
- A "Gate & Delay" unit generates a gate pulse with the length of the laser repetition time T_{rep}.
- This is combined with the laser photo diode signal in a "Coincidence" unit. A logical AND is applied such that the output is only true if the gate and the laser signal coincide.
- The coincidence unit output, i.e. the timing of the laser pulse which follows the MCP event $t_{laser,post}$, is recorded by the FC DAQ.

In the Go4 data analysis software, we calculate the timing of the laser pulse which precedes the reaction, and possibly did induce it, by subtracting the laser repetition time $t_{laser,pre} = t_{laser,post} - T_{rep}$. The timing of the MCP event relative to the preceding laser pulse is then

$$\begin{aligned} \Delta t &= t_{MCP} - t_{laser,pre} \\ \Delta t &= t_{MCP} - \left(t_{laser,post} - T_{rep}\right) \end{aligned} \tag{9.2}$$

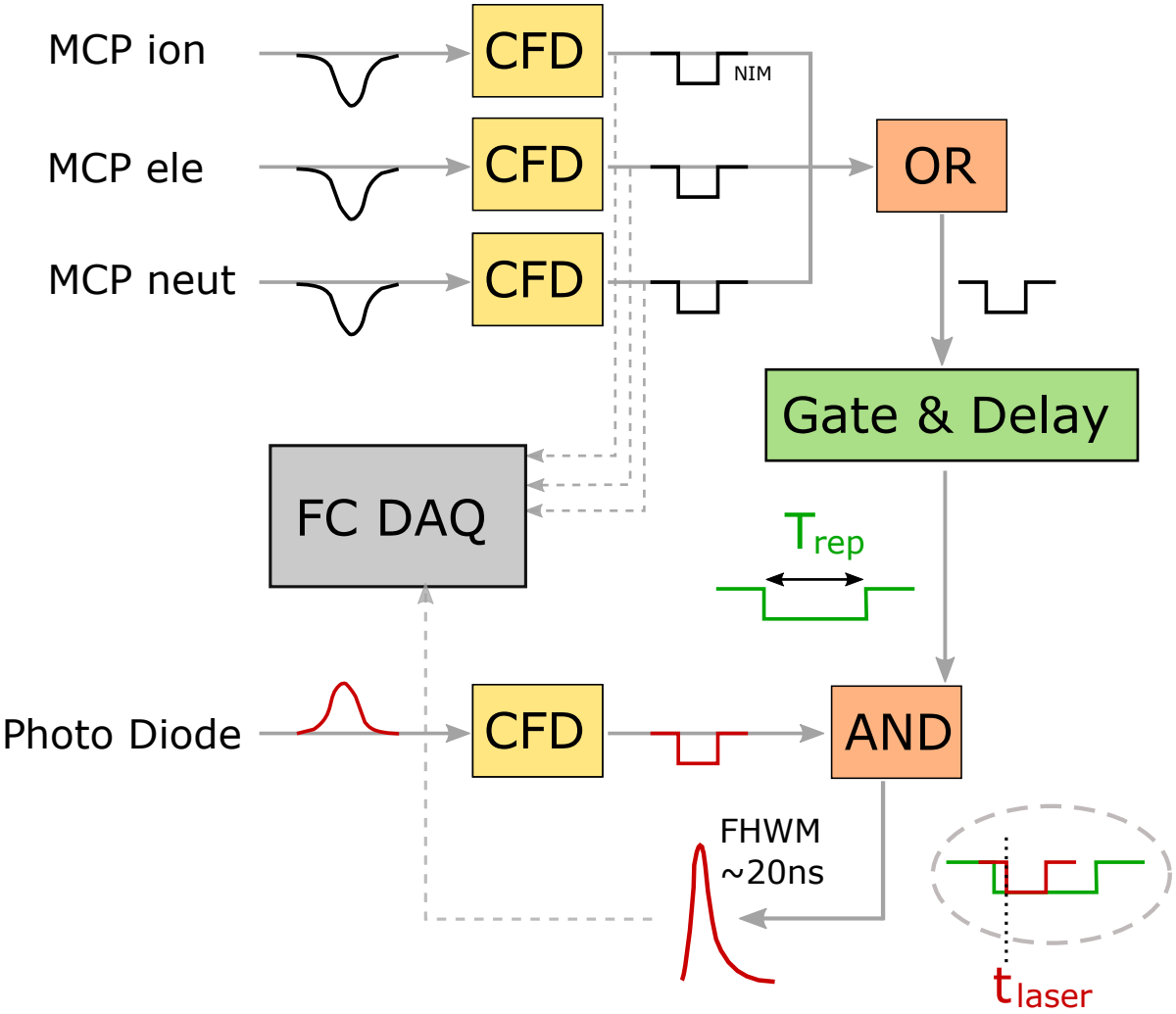

Figure 9.1: Laser gating scheme: The detector MCP signals are processed by a CFD and combined in a logical OR. The resulting NIM pulse is fed into a Gate & Delay unit which generates a gate pulse with the length of the laser repetition time T_{rep}. This gate is combined with the photo diode signal of the laser in a logical AND. The output signal timing is defined by the leading edge of the laser signal as indicated in the oval, dashed inset.

9.3 Voltage Configurations of TrapREMI

Figure 9.2 depicts the trap and REMI voltages which characterize an experimental configuration. The configurations used for the presented measurements are listed in figure 9.2.

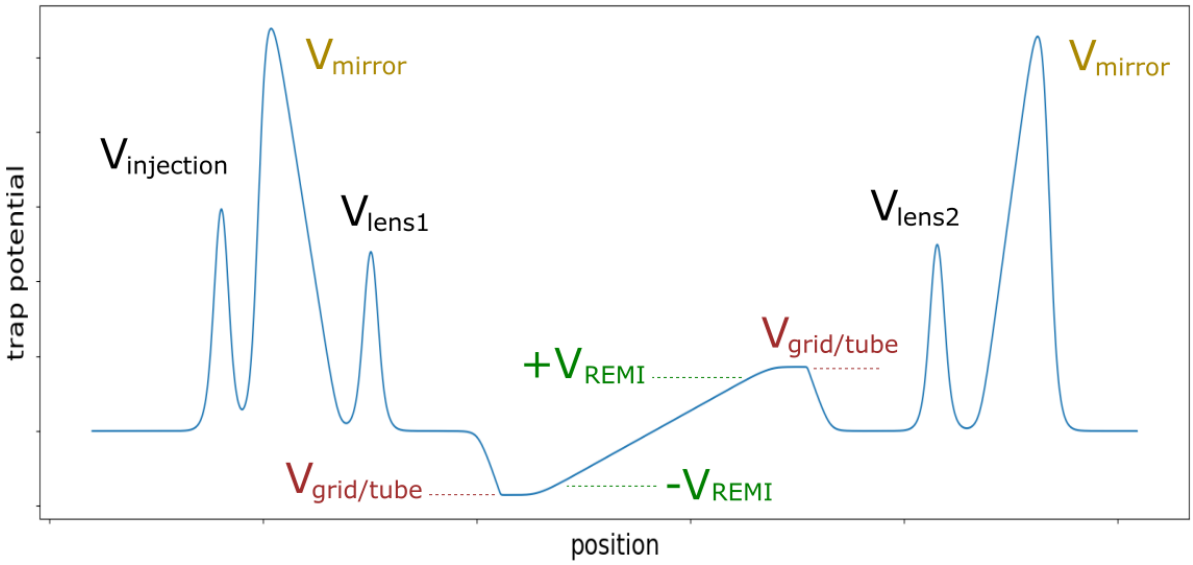

Figure 9.2: Generic potential configuration for ZIT and REMI. All elements can be modified in position and shape in order to meet specific experimental requirements. In usual configurations as depicted here, the potentials are applied symmetrically.

ion optics element	config 1	config 2	config 3	config 4
$V_{injection}[V]$	2828	2827	2670	2785
$V_{mirror}[V]$	3200	3200	3200	3200
V_{lens1} [V]	2204	2214	2181	2265
V_{lens2} [V]	2212	2220	2270	2195
V_{REMI} [V]	200	200	300	0
$V_{grid/tube}[V]$	214	214	0	0

Table 9.2: Voltage Configurations

9.4 EIBT Electrode Wiring

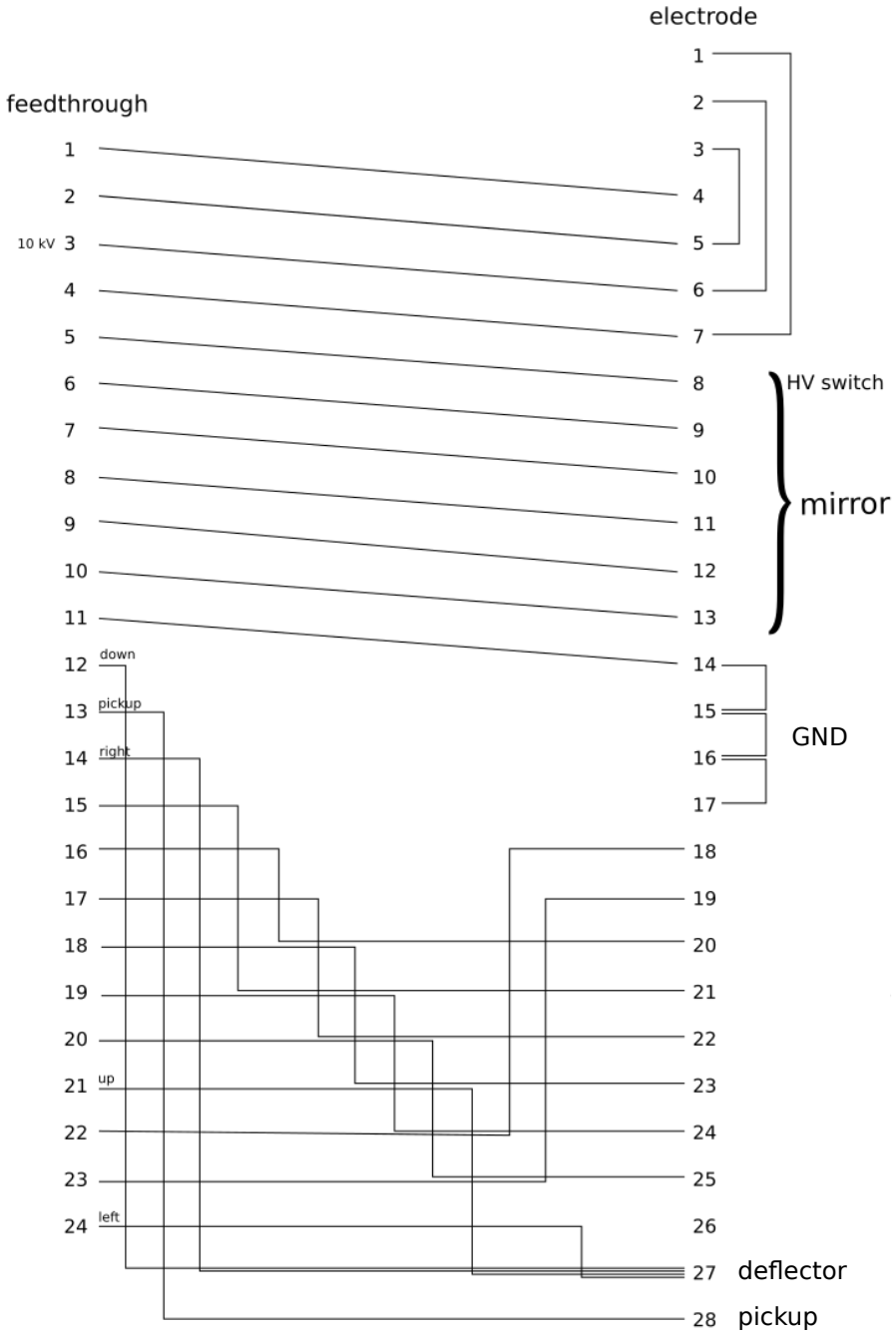

Figure 9.3: Front EIBT stack wiring of electrodes (right) to flange feedthroughs (left).

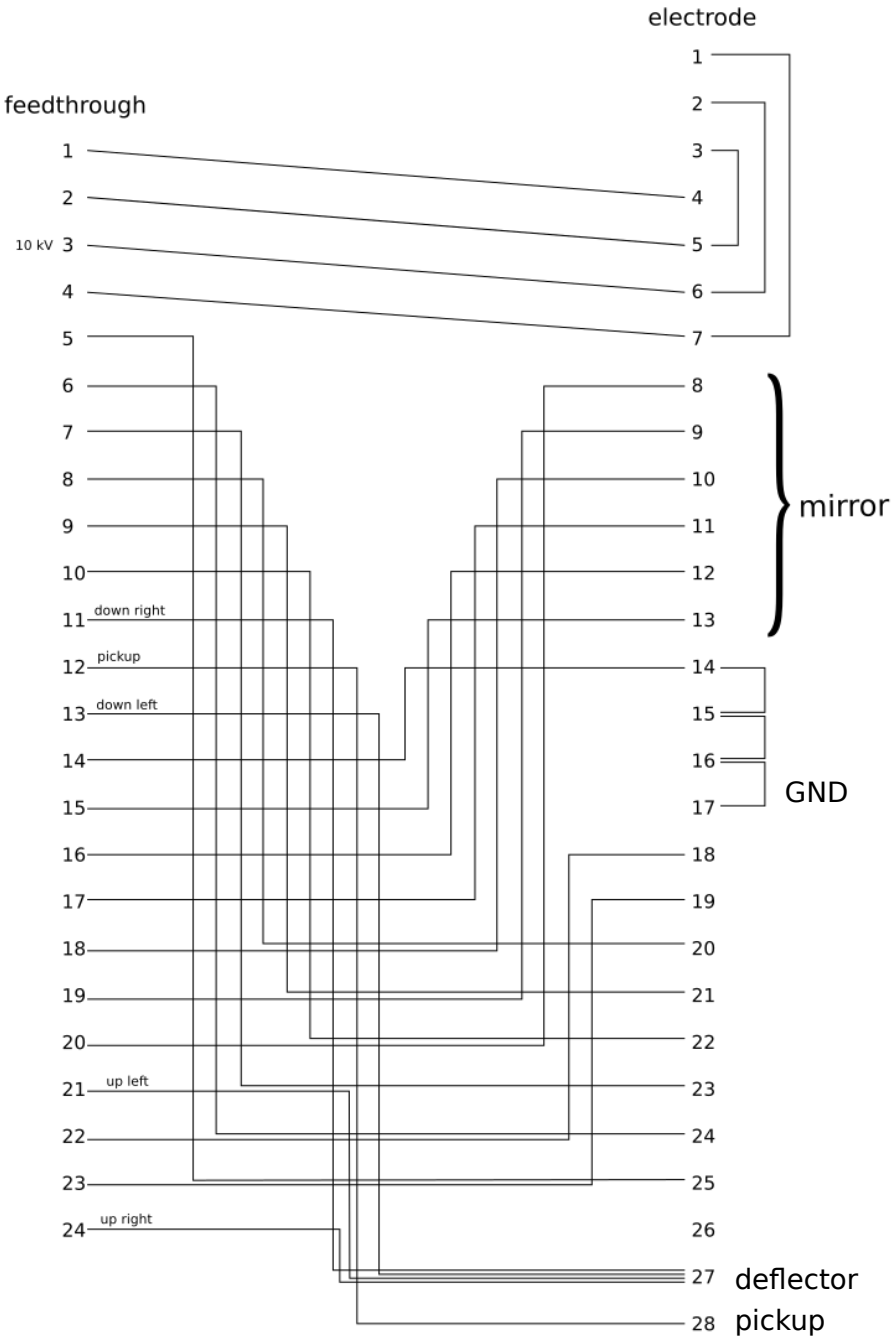

Figure 9.4: Rear EIBT stack wiring of electrodes (right) to flange feedthroughs (left).

BIBLIOGRAPHY

[1] H. J. Fraser, M. R. S. McCoustra, and D. A. Williams.
The molecular universe.
Astronomy Geophysics, 43(2):2.10–2.18, 04 2002.
doi: 10.1046/j.1468-4004.2002.43210.x.
pages 1

[2] J. W. Chamberlain.
Satellite environment handbook.
Science, 148(3671):814–814, 1965.
doi: 10.1126/science.148.3671.814.
pages 1

[3] A. V. Pavlov.
Ion chemistry of the ionosphere at e- and f-region altitudes: A review.
Surveys in Geophysics, 33:1133–1172, 2012.
doi: 10.1007/s10712-012-9189-8.
pages 1

[4] R. Ergun, L. Andersson, C. Fowler, A. Woodson, T. Weber, G. Delory, D. Andrews, A. Eriksson, T. McEnulty, M. Morooka, A. Stewart, P. Mahaffy, and B. Jakosky.
Enhanced o2+ loss at mars due to an ambipolar electric field from electron heating.
Journal of Geophysical Research: Space Physics, 121(5):4668–4678, 2016.
doi: 10.1002/2016JA022349.
pages 1

[5] Jan R. R. Verlet.
Femtosecond spectroscopy of cluster anions: insights into condensed-phase phenomena from the gas-phase.
Chem. Soc. Rev., 37:505–517, 2008.
doi: 10.1039/B700528H.
pages 2

[6] A.B. Raksit.

Reactions of o2+, o4+ and o2+·h2o ions with neutral molecules.
International Journal of Mass Spectrometry and Ion Processes, 69(1):45 – 65, 1986.
doi: https://doi.org/10.1016/0168-1176(86)87041-0.
pages 2

[7] M. Marian, R. Marian, S. D. Peyerimhoff, B.A. Hess, R. J. Buenker, and G. Seger.
Ab initio ci calculation of o2 + predissociation phenomena induced by a spin-orbit coupling mechanism.
Molecular Physics, 46(4):779–810, 1982.
doi: 10.1080/00268978200101591.
pages 2, 72, 77

[8] M. L. Vestal and G. H. Mauclaire.
Photodissociation of positive and negative ions formed in o2.
The Journal of Chemical Physics, 67(8):3767–3770, 1977.
doi: 10.1063/1.435317.
pages 2

[9] D. C. McGilvery, J. D. Morrison, and D. L. Smith.
Laser induced photodissociation of o2+.
The Journal of Chemical Physics, 70(10):4761–4768, 1979.
doi: 10.1063/1.437265.
pages 2, 71

[10] P. Coerlin.
Tracing ultra-fast molecular dynamics in O2+ and N2+ with XUV–IR pump–probe experiments.
PhD thesis, Heidelberg Graduate School of Fundamental Physics, 2015.
URL `http://hdl.handle.net/11858/00-001M-0000-0010-0BE6-7`.
pages 2, 12, 13, 14, 15, 32, 71, 72, 75, 78

[11] Idbarkach, T., Chabot, M., Béroff, K., Della Negra, S., Lesrel, J., Geslin, F., Le Padellec, A., Mahajan, T., and Díaz-Tendero, S.
Breakdown curves of ch2(+), ch3(+), and ch4(+) molecules - i. construction and application to electron collisions and uv photodissociation.
A&A, 628:A75, 2019.
doi: 10.1051/0004-6361/201935760.
pages 2

[12] A. Shahi, R. Singh, Y. Ossia, D. Zajfman, O. Heber, and D. Strasser.
Hybrid electrostatic ion beam trap (heibt): Design and simulation of ion-ion, ion-neutral, and ion-laser interactions.

Review of Scientific Instruments, 90(11):113308, 2019.
doi: 10.1063/1.5114908.
pages 3

[13] K. Hanold, A. Luong, T. Clements, and R. Continetti.
Photoelectron–multiple-photofragment coincidence spectrometer.
Review of Scientific Instruments, 70(5):2268–2276, 1999.
doi: 10.1063/1.1149751.
pages 3

[14] Robert. E. Continetti.
Continetti laboratory - machine a.
URL `http://checont6.ucsd.edu/machinea.php`.
pages 3

[15] N. G. Kling, J. McKenna, A. M. Sayler, B. Gaire, M. Zohrabi, U. Ablikim, K. D. Carnes, and I. Ben-Itzhak.
Charge asymmetric dissociation of a co^+ molecular-ion beam induced by strong laser fields.
Phys. Rev. A, 87:013418, Jan 2013.
doi: 10.1103/PhysRevA.87.013418.
pages 3

[16] R. Phaneuf, C. Havener, G. Dunn, and A. Müller.
Merged-beams experiments in atomic and molecular physics.
Reports on Progress in Physics, 62(7):1143–1180, jan 1999.
doi: 10.1088/0034-4885/62/7/202.
pages 3

[17] A. O'Connor, X. Urbain, J. Stützel, K. Miller, N. de Ruette, M. Garrido, and D. Savin.
Reaction studies of neutral atomic c with H_3^+ using a merged-beams apparatus.
The Astrophysical Journal Supplement Series, 219(1):6, jul 2015.
doi: 10.1088/0067-0049/219/1/6.
pages 3

[18] R. K. Gangwar, K. Saha, O. Heber, M. L. Rappaport, and D. Zajfman.
Autoresonance cooling of ions in an electrostatic ion beam trap.
Phys. Rev. Lett., 119:103202, Sep 2017.
doi: 10.1103/PhysRevLett.119.103202.
pages 3

[19] D. Strasser, K. G. Bhushan, H. B. Pedersen, R. Wester, O. Heber, A. Lafosse, M. L. Rappaport, N. Altstein, and D. Zajfman.

Charge-transfer dissociation of vibrationally cold heh^+ : evidence for and lifetime of the $a^3\Sigma^+$ metastable state.
Phys. Rev. A, 61:060705, May 2000.
doi: 10.1103/PhysRevA.61.060705.
pages 3

[20] D. Zajfman, O. Heber, L. Vejby-Christensen, I. Ben-Itzhak, M. Rappaport, R. Fishman, and M. Dahan.
Electrostatic bottle for long-time storage of fast ion beams.
Phys. Rev. A, 55:R1577–R1580, Mar 1997.
doi: 10.1103/PhysRevA.55.R1577.
pages 3, 10, 59

[21] Christopher J. Johnson, Rico Otto, and Robert E. Continetti.
Spectroscopy and dynamics of the hoco radical: insights into the oh + co $\rightarrow$ h + co2 reaction.
Phys. Chem. Chem. Phys., 16:19091–19105, 2014.
doi: 10.1039/C4CP02593H.
pages 3

[22] M. Lange et al.
A cryogenic electrostatic trap for long-time storage of kev ion beams.
Review of Scientific Instruments, 81(5):055105, 2010.
doi: 10.1063/1.3372557.
pages 3, 10, 57, 58, 59, 64

[23] R. von Hahn et al.
The cryogenic storage ring csr.
Review of Scientific Instruments, 87(6):063115, 2016.
doi: 10.1063/1.4953888.
pages 3

[24] Abhishek Shahi, Yishai Albeck, and Daniel Strasser.
Simultaneous 3d coincidence imaging of cationic, anionic, and neutral photo-fragments.
Review of Scientific Instruments, 89(1):013303, 2018.
doi: 10.1063/1.5004523.
pages 4

[25] S. Menk, S. Das, K. Blaum, M. W. Froese, M. Lange, M. Mukherjee, R. Repnow, D. Schwalm, R. von Hahn, and A. Wolf.
Vibrational autodetachment of sulfur hexafluoride anions at its long-lifetime limit.
Phys. Rev. A, 89:022502, Feb 2014.

doi: 10.1103/PhysRevA.89.022502.
pages 4

[26] Christopher J. Johnson, Rico Otto, and Robert E. Continetti.
Spectroscopy and dynamics of the hoco radical: insights into the oh + co $\rightarrow$ h + co2 reaction.
Phys. Chem. Chem. Phys., 16:19091–19105, 2014.
doi: 10.1039/C4CP02593H.
pages 4

[27] Wolfgang Paul.
Electromagnetic traps for charged and neutral particles.
Rev. Mod. Phys., 62:531–540, Jul 1990.
doi: 10.1103/RevModPhys.62.531.
pages 7

[28] F.M. Penning.
Die glimmentladung bei niedrigem druck zwischen koaxialen zylindern in einem axialen magnetfeld.
Physica, 3(9):873 – 894, 1936.
doi: https://doi.org/10.1016/S0031-8914(36)80313-9.
pages 7

[29] M Larsson.
Atomic and molecular physics with ion storage rings.
Reports on Progress in Physics, 58(10):1267–1319, oct 1995.
doi: 10.1088/0034-4885/58/10/003.
pages 7

[30] M. Dahan, R. Fishman, O. Heber, M. Rappaport, N. Altstein, D. Zajfman, and W. J. van der Zande.
A new type of electrostatic ion trap for storage of fast ion beams.
Review of Scientific Instruments, 69(1):76–83, 1998.
doi: 10.1063/1.1148481.
pages 7, 8, 10, 57, 58, 63, 64

[31] Frank Hinterberger.
Physik der Teilchenbeschleuniger und Ionenoptik.
Springer Heidelberg, 1 edition, 1997.
pages 8, 65

[32] Helmut Liebl.
Applied Charged Particle Optics.

Springer Heidelberg, 1 edition, 2008.
pages 8

[33] Daniel Zajfman.
Molecular physics group at weizman institut.
URL https://www.weizmann.ac.il/particle/molecule/.
pages 8

[34] Ilja Zebergs.
Charakterisierung der ionenspeicherung im projekt trapremi, 9 2019.
URL http://hdl.handle.net/21.11116/0000-0004-A9D7-B.
pages 9, 68, 69, 70

[35] H. B. Pedersen, D. Strasser, B. Amarant, O. Heber, M. L. Rappaport, and D. Zajfman.
Diffusion and synchronization in an ion-trap resonator.
Phys. Rev. A, 65:042704, Mar 2002.
doi: 10.1103/PhysRevA.65.042704.
pages 10, 51, 63, 67

[36] H. B. Pedersen et al.
Ion motion synchronization in an ion-trap resonator.
Physical review letters, 87(5):055001, jul 2001.
doi: 10.1088/1367-2630/14/7/073010.
pages 10, 51

[37] M W Froese, M Lange, S Menk, M Grieser, O Heber, F Laux, R Repnow, T Sieber, Y Toker, R von Hahn, A Wolf, and K Blaum.
The decay of ion bunches in the self-bunching mode.
New Journal of Physics, 14(7):073010, jul 2012.
doi: 10.1088/1367-2630/14/7/073010.
pages 10

[38] Alexander Dorn, R. Moshammer, C. Schröter, Theo Zouros, W Schmitt, H Kollmus, R Mann, and J. Ullrich.
Double ionization of helium by fast electron impact.
http://dx.doi.org/10.1051/jp4:1999620, 82, 03 1999.
doi: 10.1103/PhysRevLett.82.2496.
pages 11

[39] M. Sabbar, S. Heuser, R. Boge, M. Lucchini, L. Gallmann, C. Cirelli, and U. Keller.
Combining attosecond xuv pulses with coincidence spectroscopy.
Review of Scientific Instruments, 85(10):103113, 2014.

doi: 10.1063/1.4898017.
pages 11

[40] Severin Meister, Hannes Lindenblatt, Florian Trost, Kirsten Schnorr, Sven Augustin, Markus Braune, Rolf Treusch, Thomas Pfeifer, and Robert Moshammer.
Atomic, molecular and cluster science with the reaction microscope endstation at flash2.
Applied Sciences, 10:2953, 04 2020.
doi: 10.3390/app10082953.
pages 11

[41] R. Moshammer, M. Unverzagt, W. Schmitt, J. Ullrich, and H. Schmidt-Bocking.
A 4pi recoil ion electron momentum analyzer: A High resolution 'microscope' for the investigation of the dynamics of atomic, molecular and nuclear reactions.
6 1995.
pages 11

[42] R. Moshammer, D. Fischer, and H. Kollmus.
Recoil-ion momentum spectroscopy and "reaction microscopes".
Many-particle quantum dynamics in atomic and molecular fragmentation, 33-57 (2003), 35, 01 2004.
doi: 10.1007/978-3-662-08492-2_2.
pages 11

[43] J Ullrich, R Moshammer, A Dorn, R D rner, L Ph H Schmidt, and H Schmidt-B cking.
Recoil-ion and electron momentum spectroscopy: reaction-microscopes.
Reports on Progress in Physics, 66(9):1463–1545, aug 2003.
doi: 10.1088/0034-4885/66/9/203.
pages 11, 34, 87

[44] Lutz Fechner.
High resolution experiments on strong-field ionization of atoms and molecules: Test of tunneling theory, the role of doubly excited states, and channel-selective electron spectra.
PhD thesis, Heidelberg Graduate School of Fundamental Physics, 2014.
pages 11, 13, 15

[45] J Oberheide, P Wilhelms, and M Zimmer.
New results on the absolute ion detection efficiencies of a microchannel plate.
Measurement Science and Technology, 8(4):351–354, apr 1997.
doi: 10.1088/0957-0233/8/4/001.
pages 12

[46] Joseph Ladislas Wiza.

Microchannel plate detectors.
Nuclear Instruments and Methods, 162(1):587 – 601, 1979.
doi: https://doi.org/10.1016/0029-554X(79)90734-1.
pages 12

[47] Till Cremer, Bernhard W. Adams, Melvin Aviles, Camden D. Ertley, Michael R. Foley, Alexey Lyashenko, Michael J. Minot, Mark A. Popecki, Travis Rivera, Michael E. Stochaj, Anil U. Mane, Jeffrey W. Elam, Maximilian Gebhard, and Oswald H. Siegmund.
Recent developments in next-generation microchannel plates for particle identification applications.
In Oswald H. Siegmund, editor, *UV, X-Ray, and Gamma-Ray Space Instrumentation for Astronomy XXI*, volume 11118, pages 169 – 183. International Society for Optics and Photonics, SPIE, 2019.
doi: 10.1117/12.2530037.
pages 12

[48] M. Lampton, O. Siegmund, and R. Raffanti.
Delay line anodes for microchannel-plate spectrometers.
Review of Scientific Instruments, 58(12):2298–2305, 1987.
doi: 10.1063/1.1139341.
pages 12

[49] Ottmar Jagutzki, Alfred Cerezo, Achim Czasch, Reinhard Dörner, Mirko Hattaß, Min Huang, Volker Mergel, Uwe Spillmann, Klaus Ullmann-pfleger, Thorsten Weber, Horst Schmidt-böcking, and George D. W. Smith.
Multiple hit readout of a microchannel plate detector with a three-layer delayline anode.
IEEE Trans. Nucl. Sci, pages 2477–2483, 2002.
pages 13

[50] Andreas Fischer, Alexander Sperl, Philipp Cörlin, Michael Schönwald, Helga Rietz, Alicia Palacios, Alberto González-Castrillo, Fernando Martín, Thomas Pfeifer, Joachim Ullrich, Arne Senftleben, and Robert Moshammer.
Electron localization involving doubly excited states in broadband extreme ultraviolet ionization of h2.
Physical review letters, 110:213002, May 2013.
pages 13

[51] Thomas Pflueger.
Electron Impact Ionization Studies of Small Rare Gas Clusters.
PhD thesis, Heidelberg Graduate School of Fundamental Physics, 5 2012.
pages 15

[52] Scientific Instruments Services Inc.
The field and particle trajectory simulator.
URL https://simion.com/info/manual.html.
pages 21

[53] Frank Hinterberger.
Ion optics with electrostatic lenses.
2006.
pages 21, 23

[54] Sebastian Menk.
Vibrational Auto-Detachment of the Sulfur Hexafluoride Anion in a Low-background Cryogenic Ion Beam Trap.
PhD thesis, Heidelberg Graduate School of Fundamental Physics, 4 2013.
pages 24, 65

[55] RoentDek Handels GmbH.
Hexanode with central hole hex80/o, .
URL http://www.roentdek.com/detectors/.
pages 24, 27

[56] Itamar Luzon, Este Livshits, Krishnendu Gope, Roi Baer, and Daniel Strasser.
Making sense of coulomb explosion imaging.
The Journal of Physical Chemistry Letters, (6):1361–1367, Mar 2019.
doi: doi:10.1021/acs.jpclett.9b00576.
pages 26

[57] Arne Senftleben.
Kinematically complete study on electron impact ionisation of aligned hydrogen molecules.
PhD thesis, Ruperto-Carola University of Heidelberg, Germany, 2009.
pages 32

[58] GSI Helmholtzzentrum fuer Schwerionenforschung GmbH.
The go4 project page.
pages 43

[59] J. P. Blewett and Ernest J. Jones.
Filament sources of positive ions.
Phys. Rev., 50:464–468, Sep 1936.
doi: 10.1103/PhysRev.50.464.
pages 49

[60] HeatWave Labs.
Heatwave labs ion sources.
URL https://www.cathode.com.
pages 50

[61] National Institute for Standards and Technologies.
Standard reference database 101, experimental data for o2 (oxygen diatomic), .
URL https://cccbdb.nist.gov/exp2x.asp?casno=7782447&charge=0.
pages 51

[62] National Institute for Standards and Technologies.
Standard Reference Database 101, Experimental data for C2H6 (Ethane), .
URL https://cccbdb.nist.gov/exp2x.asp?casno=74840&charge=0.
pages 51

[63] National Institute for Standards and Technologies.
Standard reference database 101, list of experimental bond lengths for bond type rcn, .
URL https://cccbdb.nist.gov/expbondlengths2x.asp?descript=rCN&all=1.
pages 51

[64] National Institute of Standards and Technology.
Ethane mass spectrum (electron ionization), .
URL https://webbook.nist.gov/cgi/cbook.cgi?ID=C74840&Mask=200#Mass-Spec.
pages 52

[65] H. Kreckel, H. Bruhns, K. A. Miller, E. Wåhlin, A. Davis, S. Höckh, and D. W. Savin.
A simple double-focusing electrostatic ion beam deflector.
Review of Scientific Instruments, 81(6):063304, 2010.
doi: 10.1063/1.3433485.
pages 53

[66] Behlke Electronic GmbH.
Behlke hts 121 data sheet, .
URL https://www.behlke.com/pdf/121.pdf.
pages 54

[67] R. A. Phaneuf, F. W. Meyer, and R. H. McKnight.
Single-electron capture by multiply charged ions of carbon, nitrogen, and oxygen in atomic and molecular hydrogen.
Phys. Rev. A, 17:534–545, Feb 1978.
doi: 10.1103/PhysRevA.17.534.
pages 57

[68] D. L. Smith and L. Kevan.
Total charge-transfer cross sections in molecular systems.
Journal of the American Chemical Society, 93(9):2113–2117, 1971.
doi: 10.1021/ja00738a004.
pages 57

[69] Ludwig Hoibl.
Design und simulation der ionenstrahlführung im projekt trapremi, 2017.
URL `http://hdl.handle.net/11858/00-001M-0000-002D-4A39-6`.
pages 60, 61

[70] R. Rispoli, E. De Angelis, L. Colasanti, N. Vertolli, S. Orsini, J. A. Scheer, A. Mura, A. Milillo, P. Wurz, S. Selci, A. M. Di Lellis, R. Leoni, M. D'Alessandro, F. Mattioli, and S. Cibella.
ELENA MCP detector: absolute detection efficiency for low-energy neutral atoms.
In *Modern Technologies in Space- and Ground-based Telescopes and Instrumentation II*, volume 8450, pages 1792 – 1798. International Society for Optics and Photonics, SPIE, 2012.
doi: 10.1117/12.926185.
pages 65, 88

[71] D. Attia, D. Strasser, O. Heber, M.L. Rappaport, and D. Zajfman.
Transverse kinematics of ions stored in an electrostatic ion beam trap.
Nuclear Instruments and Methods in Physics Research Section A: Accelerators, Spectrometers, Detectors and Associated Equipment, 547(2):279 – 286, 2005.
doi: https://doi.org/10.1016/j.nima.2005.03.141.
pages 67

[72] L. Bytautas, N. Matsunaga, and K. Ruedenberg.
Accurate ab initio potential energy curve of o2. ii. core-valence correlations, relativistic contributions, and vibration-rotation spectrum.
The Journal of Chemical Physics, 132(7):074307, 2010.
doi: 10.1063/1.3298376.
pages 72, 73

[73] I. V. Hertel and C.-P. Schulz.
Atome, Moleküle und Optische Physik 2.
Springer Heidelberg, 1 edition, 2010.
pages 73, 76

[74] James A. R. Samson and R. B. Cairns.
Ionization potential of o2.

J. Opt. Soc. Am., 56(6):769–775, Jun 1966.
doi: 10.1364/JOSA.56.000769.
pages 73

[75] P.W. Atkins and R.S. Friedman.
Molecular Quantum Mechanics.
Oxford University Press, 4 edition, 2004.
pages 74

[76] Gordon H. Dunn.
Anisotropies in angular distributions of molecular dissociation products.
Phys. Rev. Lett., 8:62–64, Jan 1962.
doi: 10.1103/PhysRevLett.8.62.
pages 77

[77] National Institute of Standards and Technology.
Oxygen mass spectrum (electron ionization), .
URL `https://webbook.nist.gov/cgi/cbook.cgi?ID=C7782447&Mask=200#Mass-Spec`.
pages 79

[78] Wolfgang Demtroeder.
Laser Spectroscopy. Basic Concepts and Instrumentation, pages 359–364.
Springer Heidelberg, 3 edition, 2003.
pages 83

[79] M. Riggin and R.C. Dunbar.
Photodissociation of ch4+ via ion cyclotron resonance.
Chemical Physics Letters, 31(3):539 – 542, 1975.
doi: https://doi.org/10.1016/0009-2614(75)85080-9.
pages 101

[80] National Institute of Standards and Technology.
Methane mass spectrum (electron ionization), .
URL `https://webbook.nist.gov/cgi/cbook.cgi?ID=C74828&Mask=200#Mass-Spec`.
pages 102

[81] Wikipedia.
Reflectron.
URL `https://en.wikipedia.org/wiki/Reflectron`.
pages 105

[82] A. Markevitch, D. Romanov, S. Smith, and R. Levis.

Coulomb explosion of large polyatomic molecules assisted by nonadiabatic charge localization.
Phys. Rev. Lett., 92:063001, Feb 2004.
doi: 10.1103/PhysRevLett.92.063001.
pages 112

[83] Matt W. Ross and A.W. Castleman.
Strong-field ionization and coulomb explosion of small neodymium and europium oxide clusters.
Chemical Physics Letters, 565:22 – 27, 2013.
doi: https://doi.org/10.1016/j.cplett.2013.02.044.
pages 112